

# **Interrelationships of Microstructure, Stress and Diffusion**

von der Fakultät Chemie der Universität Stuttgart  
zur Erlangung der Würde eines Doktors der  
Naturwissenschaften (Dr. rer. nat.) genehmigte Abhandlung

vorgelegt von

**Yener Kuru**

aus Samsun/Türkei

Hauptberichter: Prof. Dr. Ir. E. J. Mittemeijer

Mitberichter: Prof. Dr. F. Aldinger

Mitprüfer: Prof. Dr. H. Bertagnolli

Tag der Einreichung: 21.12.2007

Tag der mündlichen Prüfung: 01.04.2008

MAX-PLANCK-INSTITUT FÜR METALLFORSCHUNG STUTTGART  
INSTITUT FÜR METALLKUNDE DER UNIVERSITÄT STUTTGART

Stuttgart 2008



*Dedicated to my wife, parents and sister*



# Contents

<b>1. General introduction .....</b>	<b>7</b>
<b>2. Non-ambient X-ray diffraction residual stress analysis of thin films: tracing nanosize-related effects on thermoelastic constants and identifying sources of residual stresses .....</b>	<b>13</b>
<b>2.1 Introduction.....</b>	<b>14</b>
<b>2.2 Theoretical background .....</b>	<b>16</b>
2.2.1 (X-ray) Diffraction stress analysis .....	16
2.2.2 In-situ temperature calibration and determination of thermal expansion coefficient via the strain-free lattice constant.....	17
<b>2.3 Experimental and data evaluation.....</b>	<b>19</b>
<b>2.4 Results and discussion .....</b>	<b>21</b>
2.4.1 Crystallographic textures of the specimens.....	21
2.4.2 In-situ temperature calibration and determination of coefficient of thermal expansion.....	22
2.4.3 Use of temperatures below ambient temperature for characterizing the elastic behaviour of the film/substrate assembly .....	26
2.4.4 Measurement of the thermoelastic slope of the film/substrate assembly .....	30
<b>2.5 Conclusions.....</b>	<b>32</b>
<b>3. Crystal size dependence of the coefficient of thermal expansion of metals.....</b>	<b>35</b>
<b>3.1 Introduction.....</b>	<b>36</b>
<b>3.2 Experimental .....</b>	<b>37</b>
<b>3.3 Results and discussion .....</b>	<b>38</b>
<b>3.4 Conclusions.....</b>	<b>44</b>
<b>4. Interdiffusion and stress development in Cu-Pd thin film diffusion couples.....</b>	<b>47</b>
<b>4.1 Introduction.....</b>	<b>48</b>
<b>4.2 Experimental .....</b>	<b>50</b>
4.2.1 Specimen production.....	50
4.2.2 Transmission electron microscopy.....	50

4.2.3	Concentration-depth profiling .....	50
4.2.4	X-ray diffraction .....	51
<b>4.3</b>	<b>Results .....</b>	<b>55</b>
4.3.1	Diffusional intermixing .....	55
4.3.2	Microstructure .....	56
4.3.3	Phase formation .....	57
4.3.4	Stress evolution .....	59
4.3.5	Line broadening analysis of the single layers and sublayers of the couple .....	62
<b>4.4</b>	<b>Discussion .....</b>	<b>65</b>
4.4.1	Thermoelastic behaviour .....	65
4.4.2	Overview of possible stress changes at elevated temperatures .....	65
<b>4.5</b>	<b>Summary .....</b>	<b>71</b>
<b>5.</b>	<b>Kurzfassung der Dissertation in deutscher Sprache .....</b>	<b>75</b>
<b>5.1</b>	<b>Einleitung .....</b>	<b>75</b>
<b>5.2</b>	<b>Röntgenographische Eigenspannungsanalyse dünner Schichten durch temperaturabhängige in-situ Messungen unter- und oberhalb der Raumtemperatur: Bestimmung der thermoelastischen Konstanten nanokristalliner Materialien und Identifizierung der Quellen von Eigenspannungen .....</b>	<b>76</b>
5.2.1	Kalibrierung einer Heiz-/Kühlkammer und Messung des thermischen Ausdehnungskoeffizienten .....	76
5.2.2	Differenzierung von durch thermisch aktivierte Relaxationsprozesse hervorgerufenen Spannungen von thermo-elastischen Spannungen .....	79
<b>5.3</b>	<b>Kristallitgrößenabhängigkeit des thermischen Ausdehnungskoeffizienten von Metallen .....</b>	<b>82</b>
<b>5.4</b>	<b>Interdiffusion und Spannungsaufbau in Diffusionspaaren aus Cu-Pd Dünnschichten .....</b>	<b>86</b>
5.4.1	Interdiffusion .....	86
5.4.2	Phasenzusammensetzung .....	87
5.4.3	Entwicklung der mechanischen Spannungen .....	88
	<b>Curriculum Vitae .....</b>	<b>95</b>
	<b>Acknowledgements .....</b>	<b>97</b>

# Chapter 1

## General introduction

Thin films are the focus of numerous investigations due to their peculiar properties with respect to bulk materials (fundamental science point of view) and their importance in e.g. the microelectronics industry (application point of view) [1-4]. Thin films can exhibit very high residual, internal stresses, as the yield stress can surpass the value for a corresponding bulk material considerably [5,6]. Residual stresses in thin films on substrates can be generated by volume changes of the thin film: If a process causes a contraction of the film (which is hindered by the substrate), tensile stresses develop if the lateral film dimensions are dictated by the substrate (Fig. 1.1). On the other hand, compressive stresses arise as a consequence of a volume expansion. Residual stresses can be classified as follows:

**Intrinsic stresses** are created during the film production. Several deposition parameters as material and temperature of the substrate, gas pressure and deposition rate for sputter-deposited films, film thickness etc. can affect the stress state. For films deposited by sputtering, the atomic peening effect and interatomic forces acting across porous columnar grain boundaries are the most important sources of compressive and tensile intrinsic stresses, respectively [7]. The occurrence of atomic peening involves that atoms with high kinetic energies (atoms separated from the target or Ar atoms that are neutralized and backscattered from the target) hit the newly forming film. This results in the formation of defects and entrapment of Ar atoms in the lattice. The associated volume expansion leads to a build-up of compressive residual stresses in a thin film attached to a substrate [8]. Tensile stresses can originate from the microstructure of columnar grains separated by void networks. Both simulations [9,10] and experiments [11] indicate that interatomic forces acting across the voids decorating the grain boundaries (which may be of atomic size) can bring about macroscopic tensile stress. The magnitude of the tensile stress is inversely proportional to the lateral grain size as the fraction of the atoms influenced by the intercolumnar attraction increases with decreasing column diameter [12].

**Extrinsic stresses** arise after film deposition. Some of the processes that can cause extrinsic residual stresses are: temperature changes (if the coefficients of thermal expansion of the film and the substrate material differ), phase transformations (if the molar volumes of the initial and the final phases are different), diffusion (if molar volumes and/or fluxes of the diffusing atoms are different), microstructural stabilization processes such as grain growth and defect

annihilation (i.e. excess volume in the structure is eliminated) and electrostatic and/or magnetic forces.

Apart from direct mechanical effects (e.g. plastic deformation when the stress level exceeds the yield limit or cracking when the fracture strength is exceeded), several processes such as grain growth and diffusion can be affected by these stresses and their gradients [13,14]. It is thus of cardinal importance to measure and control the residual stresses in thin films.

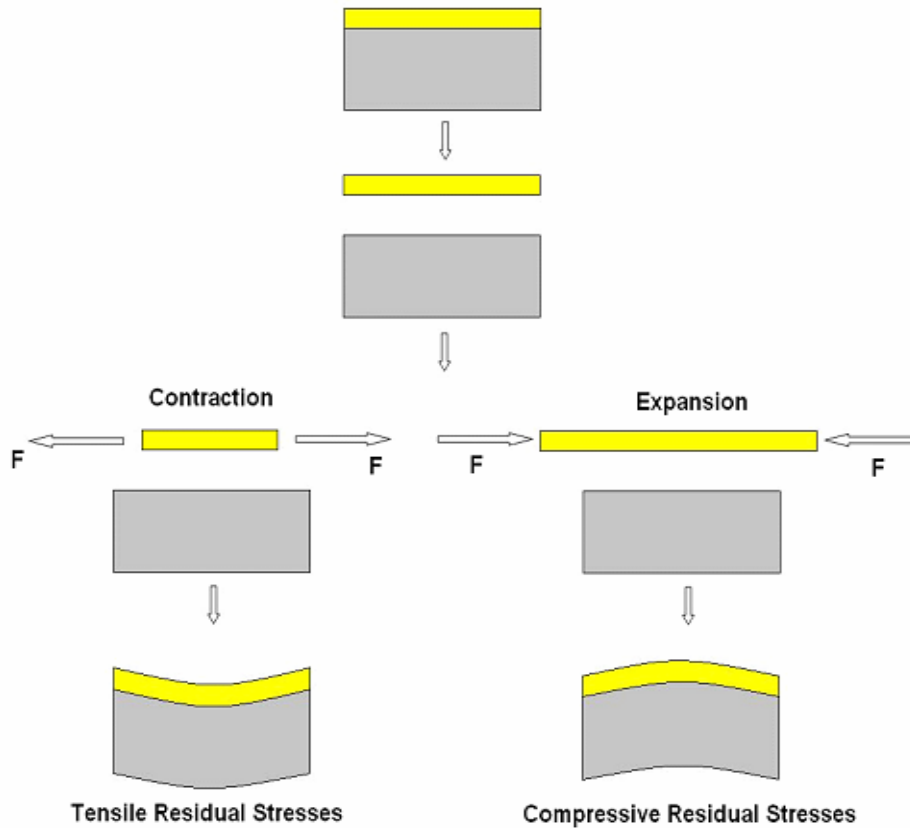


**Fig. 1.1:** Schematic presentation of volume changes of a thin film with respect to the substrate and the arising stresses.

This work is dedicated to the investigation of the interrelationships of microstructure, stress and diffusion in thin films. Non-ambient X-ray diffraction stress measurements constitute a focal point of interest and were complemented with transmission electron microscopy investigations (for microstructural analyses) and Auger-electron spectroscopy measurements in combination with sputter-depth profiling (for composition-depth profiling).

X-ray diffraction (XRD) is one of the most frequently used approaches for (residual) stress measurement. Besides being non-destructive and highly accurate (stresses of some MPa can be detected), the stress states of all crystalline phases in a layered structure can be



obtained separately [15-17]. Moreover, additional microstructural information, as the crystallographic texture, the density of crystalline defects, such as dislocations, and the crystal size can be acquired from the collected XRD data [18].

The experimental setup employed is of cardinal importance for accurate stress measurements. High brilliance (generally expressed as photons/mrad<sup>2</sup>/mm<sup>2</sup>/s) X-ray sources are necessary to investigate variation of residual stresses and formation of new phases in thin films (50 nm thick films were used in this study) in-situ. A Cu rotating anode (Bruker TXS) and a collimating single-reflection X-ray mirror (Xenocs FOX2D CU 12\_INF) were employed to meet this requirement [19,20] (Fig. 1.2). Such a system increases the diffracted intensity by about a factor of 300 compared to a sealed tube and a conventional cross-coupled mirror and a small instrumental broadening, important for an accurate line broadening analysis to probe the crystallite size and microstrain of the sample, is obtained. For in-situ, temperature-dependent, experiments a heating/cooling chamber DCS350 (Anton Paar) was mounted on the Eulerian cradle (see also Ref. [21]). It is possible with this equipment to make in-situ experiments within a temperature range between -100 °C and 350 °C and at pressures of the order of 10<sup>-3</sup> mbar.

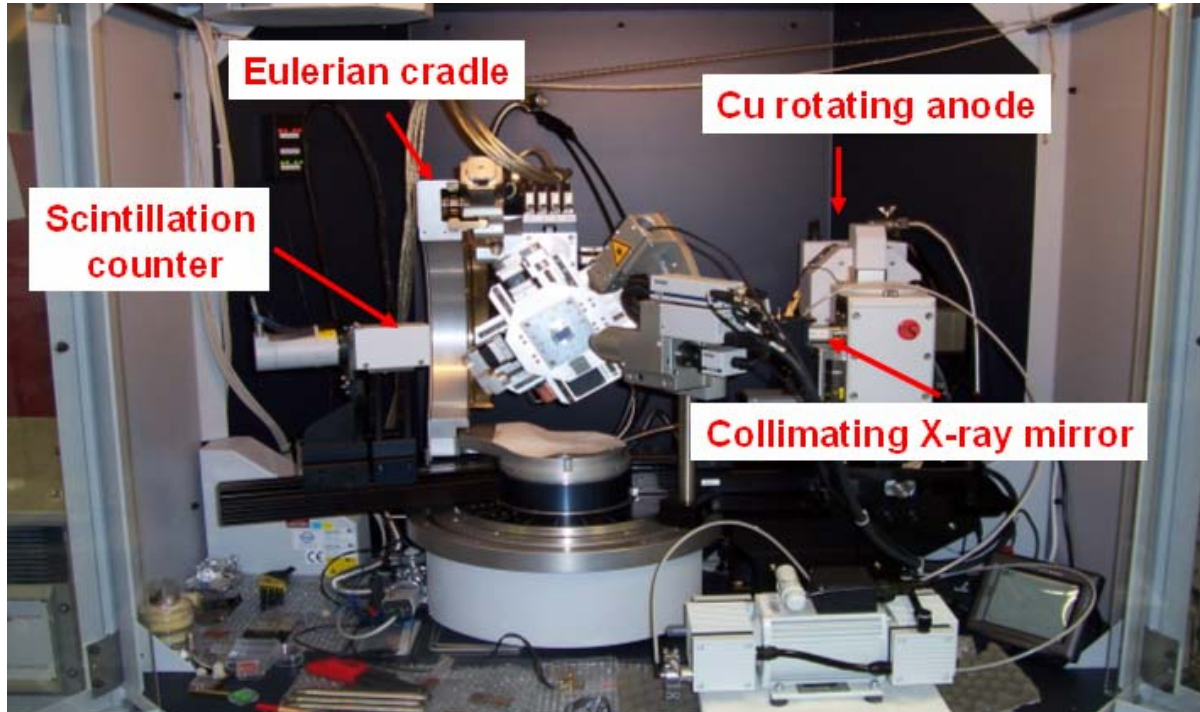


**Fig. 1.2:** Bruker D8 Discover diffractometer employed in residual stress analysis.

As compared to room temperature measurements, the interpretation of XRD data recorded at non-ambient temperatures is much more demanding. In Chapter 2 of the thesis,

methodological aspects and problems associated with in-situ, temperature-dependent XRD stress analyses have been addressed and possible solutions have been discussed in detail.

Chapter 3 is devoted to the coefficient of thermal expansion (CTE) of nanocrystalline materials. The CTE of nanocrystalline materials has been investigated both theoretically and experimentally in numerous studies. Several contradictory observations for the crystal-size dependence of the CTE can be found in literature [22,23]. On the basis of the above indicated methodological developments, it has been demonstrated unambiguously for the first time by in-situ, temperature dependent XRD stress measurements that the crystallite size affects the CTE of metal thin films. The CTE increases from its bulk value with decreasing crystallite size.

In spite of the scientific and technological importance, systematic investigations of the effect of interdiffusion on residual (internal) stresses in thin films are rare. In the Chapter 4 of the thesis, interdiffusion, phase formation and the stress evolution in thin bi-layer (individual layer thickness: 50 nm) diffusion couples of Cu and Pd have been investigated employing in-situ X-ray diffraction measurements. It has been found that upon annealing at relatively low temperatures (185 °C) for durations up to 17 hours considerable diffusional intermixing, accompanied by the formation of new phases and considerable stress changes, occurs. The stress evolution in the Cu-Pd bilayer during diffusion annealing deduced from in-situ XRD measurements has been discussed in the light of the stress evolution obtained for single Cu and Pd layers, deposited in identical conditions and subjected to the same heat treatment as the bilayers. This has made possible, for the first time, a separation of stresses caused by microstructural relaxation (decrease of crystalline imperfection) from stresses caused by interdiffusion.

## References

- [1] W. D. Nix, Metall. Trans. A **20A**, 2217 (1989).
- [2] M. F. Doerner and W. D. Nix, Crit. Rev. Solid State **14**, 225 (1988).
- [3] G. C. A. M. Janssen, Thin Solid Films **515**, 6654 (2007).
- [4] L. B. Freund and S. Suresh, *Thin Film Materials Stress, Defect Formation and Surface Evolution*, (Cambridge Univ. Press, Cambridge, 2003).
- [5] T. J. Balk, G. Dehm and E. Arzt, Acta Mater. **51**, 4471 (2003).
- [6] E. Arzt, Acta Mater. **46**, 5611 (1998).
- [7] M. Ohring, *Materials Science of Thin Films*, (Academic Press, San Diego, 2002).
- [8] H. Windischmann, Crit. Rev. Solid State **17**, 547 (1992).
- [9] K. H. Müller, J. Appl. Phys. **62**, 1796 (1987).
- [10] C. C. Fang, F. Jones and V. Prasad, J. Appl. Phys. **74**, 4472 (1993).
- [11] M. Itoh, M. Hori and S. Nadahara, J. Vac. Sci. Technol. **B 9**, 149 (1991).
- [12] J. A. Floro, E. Chason, R. C. Cammarata and D. J. Srolovitz, MRS Bull. **27**, 19 (2002).
- [13] F. C. Larche and J. W. Cahn, Acta Metall. **30**, 1835 (1982).
- [14] F. C. Larche and J. W. Cahn, Acta Metall. **33**, 331 (1985).
- [15] U. Welzel, J. Ligot, P. Lamparter, A. C. Vermeulen and E. J. Mittemeijer, J. Appl. Cryst. **38**, 1 (2005).
- [16] V. Hauk, *Structural and Residual Stress Analysis by Nondestructive Methods Evaluation, Application, Assessment*, (Elsevier, Amsterdam, 1997).
- [17] I. C. Noyan and J. B. Cohen, *Residual Stress*, (Springer-Verlag, Berlin, 1987).
- [18] E. J. Mittemeijer and P. Scardi (Eds.), *Diffraction Analysis of the Microstructure of Materials*, (Springer, Berlin;Heidelberg, 2004).
- [19] M. Wohlschlögel, T. U. Schüllli, B. Lantz and U. Welzel, J. Appl. Cryst. **41**, 124 (2008).
- [20] M. Wohlschlögel, T. U. Schüllli, G. Maier, U. Welzel and E. J. Mittemeijer, Z. Kristallogr. Suppl. **26**, 147 (2007).

[21] M. Wohlschlägel, U. Welzel, G. Maier and E. J. Mittemeijer, *J. Appl. Cryst.* **39**, 194 (2006).

[22] W. Fang, and C. Y. Lo, *Sensor Actuat. A-Phys* **84**, 310 (2000).

[23] Y. Zoo, D. Adams, J. W. Mayer, and T. L. Alford, *Thin Solid Films* **513**, 170 (2006).

## Chapter 2

# Non-ambient X-ray diffraction residual stress analysis of thin films: tracing nanosize-related effects on thermoelastic constants and identifying sources of residual stresses

*Y. Kuru, M. Wohlschlägel, U. Welzel and E.J. Mittemeijer*

### Abstract

The stress evolutions at non-ambient temperatures in Ni and Pd layers (thickness of each metal layer was 50 nm) were investigated employing *in-situ* X-ray diffraction measurements in a temperature range between -100 °C and 250 °C. Stress determinations were performed by analyzing the X-ray diffraction data according to the  $\sin^2\psi$ -method on the basis of the crystallite group variant. The stress evolution in the Ni layer was correlated with the change of its coherently diffracting domain size and its microstrain with temperature. The advantage of measurements at temperatures below ambient to distinguish the thermal stresses from effects of stress relaxation and emerging secondary stresses, arising from thermally activated processes (such as grain growth), was highlighted in this work for the first time. The possibility to use the *in-situ* X-ray diffraction stress measurement to obtain coefficients of thermal expansion and thermoelastic slopes of thin films (with nanosized grains) was discussed in detail.

## 2.1 Introduction

Thin films can exhibit very high residual, internal stresses arising from the film growth, from thermal mismatch induced by cooling or heating due to difference of thermal shrinkage/expansion of the film and the substrate and, possibly, from interdiffusion and phase transformations occurring during or after film deposition if the specimen is subjected to aging and/or some time-temperature programme [1-5]. Various investigations have been devoted to the investigation of such residual stresses and their impact on the (mechanical) properties of layered structures (see, e.g. [6-14]). For such studies, the availability of accurate methods for ambient and non-ambient (in-situ) stress analyses is a prerequisite.

X-ray diffraction (XRD) is one of the most frequently used approaches for (residual) stress measurement. Besides being non-destructive and highly accurate (stress (variation) of some MPa can be detected), the stress states of all crystalline phases in a layered structure can be obtained separately [15-17]. Moreover, additional microstructural information, as the crystallographic texture, the density of crystalline defects, such as dislocations, and the crystal size can be acquired from the collected XRD data.

Usually XRD stress analysis is performed at room temperature, but, in principle, in-situ, e.g. during thermal treatments, XRD stress analysis is possible as well [18,19]. As compared to room temperature measurements, the interpretation of XRD data recorded at non-ambient temperatures is more demanding for the following reasons:

- (i) The temperature dependence of physical properties of films and the substrate has to be known for data analysis and interpretation: for example, the temperature dependence of the coefficients of linear thermal expansion (CTE) of film and substrate and the temperature dependence of the elastic constants. Such data may be unavailable or ambiguous. Note, for example, that the data for the coefficient of thermal expansion of silicon reported in the literature exhibit a spread of more than 20 % at a temperature of 25 °C (although silicon is an extensively studied material in the semiconductor industry; cf. Wohlschlögel *et al.* [18]). Moreover, it was found that the CTE of thin films and nanocrystalline materials can differ considerably from the (bulk) literature values [20].
- (ii) Precise knowledge of the specimen temperature may lack. It has been shown that the reading of the temperature gauge of the temperature controller of the non-ambient chamber is usually unacceptable as correct indication of the actual specimen temperature [18,21]. Dedicated calibration procedures should be followed. In addition, lateral and/or through-thickness temperature gradients can pose further problems [21].

(iii) Thermally activated processes can influence the stress state of thin films, as stress relaxation [22,23] or oxidation [2] may occur already at only slightly elevated temperatures (if not already at room temperature). A separation of the various contributions to the state of stress can then be difficult.

Recipes for avoiding the above problems during in-situ stress measurements will be given in this paper. To this end a detailed in-situ X-ray diffraction analysis of stress in Pd and Ni thin films has been performed in the temperature interval between -100 °C and 250 °C.

Apart from focusing on an accurate determination of the CTEs of film and/or substrate, attention is paid in particular to the necessity of measurements below ambient temperature to exclude thermally activated processes (i.e. grain growth and defect annihilation). This last possibility has rarely been exploited until now.

## 2.2 Theoretical background

### 2.2.1 (X-ray) Diffraction stress analysis

In diffraction stress analysis, diffraction lines of one or more  $hkl$  reflections are recorded at various tilt,  $\psi$  (and possibly, dependent on the complexity of the stress state, rotation,  $\varphi$ ) angles (for details and a rigorous definition of the angles  $\psi$  and  $\varphi$ , see [15-17]). From the measured peak positions, lattice spacings  $d_{\varphi,\psi}^{hkl}$  and thus lattice strains  $\varepsilon_{\varphi,\psi}^{hkl}$  can be calculated:

$$\varepsilon_{\varphi,\psi}^{hkl} = \frac{d_{\varphi,\psi}^{hkl} - d_0^{hkl}}{d_0^{hkl}}. \quad (1)$$

where  $d_0^{hkl}$  is the strain-free lattice spacing of the  $\{hkl\}$  planes.

In the following, the discussion will be restricted to the case of a planar, rotationally symmetric state of stress,  $\sigma_{11}^S = \sigma_{22}^S \equiv \sigma$ , where  $\sigma_{11}^S$  and  $\sigma_{22}^S$  denote the principal stresses, in the specimen frame of reference, parallel to the surface. This restriction can be adopted without limiting the generality of the proposed methods, except for the case of a triaxial state of stress (which always requires the a priori knowledge of the strain-free lattice constants for the determination of the full stress tensor). For the case of a planar, rotationally symmetric state of stress,  $\varepsilon_{\varphi,\psi}^{hkl}$  is independent of  $\varphi$  and, dropping the subscript  $\varphi$ , it holds (using Eq. (1)) [15,16,24]:

$$d_{\psi}^{hkl} = 2d_0^{hkl} \sigma S_1^{hkl} + d_0^{hkl} + \frac{1}{2} d_0^{hkl} \sigma S_2^{hkl} \sin^2 \psi \quad (2)$$

where  $S_1^{hkl}$  and  $\frac{1}{2} S_2^{hkl}$  are the diffraction elastic constants. The formulation in Eq. (2) in terms of  $d_{\psi}^{hkl}$ , instead of  $\varepsilon_{\psi}^{hkl}$ , is preferred, as, due to the small difference between  $d_{\psi}^{hkl}$  and  $d_0^{hkl}$ , a small error in  $d_0^{hkl}$  introduces a large error in  $\varepsilon_{\psi}^{hkl}$ . Then, for stress determination, a very accurate value of  $d_0^{hkl}$  is not required, as its error enters only into a product, not into a difference (see Eq. (78) in Ref. [15]).

The strain-free lattice spacing  $d_0^{hkl}$  can be determined directly from the measurement of the stressed sample. It is given by the measured lattice spacing in the direction prescribed by that angle  $\psi$ , for which, according to the elastic theory, the strain is zero. In case of a quasi-isotropic specimen (a specimen which is not intrinsically isotropic but as a macroscopic whole can be treated as isotropic due to its polycrystalline nature, random texture and the



absence of direction-dependent grain interaction) [15] and a rotationally symmetric (i.e. no dependence on  $\varphi$ ) biaxial state of stress, the direction,  $\psi^*$ , of zero strain is given by

$$\sin^2 \psi^* = -2S_1^{hkl} / \left( \frac{1}{2} S_2^{hkl} \right). \quad (3)$$

(cf. Eq. (2)). A detailed discussion of the stress-free direction for more complicated stress states and the relation with the stress component  $\sigma_{33}^S$  can be found in Ref. [16].

A dedicated approach can be used for specimens with very sharp and strong texture components. The texture may then be described by single-crystal like ideal orientations. The corresponding diffraction stress analysis method is called crystallite group method [25-30]. In this limit, single-crystal elastic compliances can be used instead of the diffraction elastic constants/diffraction stress factors (for details, see [15]; for in particular, limitations of the CGM in the case of fibre texture, see Ref. [31]). For the case of the CGM,  $\sin^2 \psi^*$  is calculated employing the following equation, instead of Eq. (3):

$$\sin^2 \psi^* = \left( -2s_{12} - \frac{2}{3}(s_{11} - s_{12} - \frac{s_{44}}{2}) \right) / \left( \frac{1}{2} s_{44} \right). \quad (4)$$

where  $s_{11}$ ,  $s_{12}$  and  $s_{44}$  are the single-crystal compliances.

### **2.2.2 In-situ temperature calibration and determination of thermal expansion coefficient via the strain-free lattice constant**

For simplicity, cubic materials, which have isotropic CTEs, will be considered for the description of the methodological possibilities. An in-situ temperature calibration is possible via determination of the strain-free lattice constants provided that accurate temperature-dependent coefficient of (linear) thermal expansion of the film,  $\alpha_F(T)$  (and/or the substrate,  $\alpha_S(T)$ ), is known. In the following, the treatment will be formulated for the case that the film is employed for the temperature calibration. It holds:

$$\frac{a_0(T_f) - a_0(T_a)}{a_0(T_a)} = \int_{T_a}^{T_f} \alpha_F(T') dT'. \quad (5)$$

where  $a_0(T_a)$  and  $a_0(T_f)$  denote the strain-free lattice constant of the film at ambient temperature and at a final temperature, respectively. Generally, Eq. (5) has to be solved for  $T_f$  numerically. Only if  $\alpha_F(T)$  is constant or if it can be approximated by a simple analytical expression, Eq. (5) can be solved analytically for  $T_f$ .

The practical applicability of Eq. (5) for temperature calibration may be affected by in particular:

(i) Scatter of the literature CTE data which can occur for even widely studied materials (as Si; cf. Section I and Ref. [18]). This scatter may partly be the result of inaccurate measurements of CTEs, but differences in specimen composition and microstructure may also contribute to it. It has, for example, been found that the CTEs of nanocrystalline materials may differ considerably from the CTEs of corresponding coarse-grained materials [20] (see also Section IV). It should be recognized that CTEs measured by dilatometric and diffraction methods are intrinsically different. Whereas dilatometric measurements sense length changes resulting from the lattice expansion and the increase of the vacancy concentration upon increasing the temperature (i.e., dilatometry records the macroscopic, mechanical length change), diffraction methods record the lattice expansion only (see, for example Ref. [32]). Thus, upon approaching the melting temperature (where a considerable vacancy concentration occurs), CTEs determined by diffraction are always smaller than CTEs determined employing dilatometry.

(ii) Erroneous values for the elastic constants used for deriving the (unstrained) lattice constant from the diffraction measurement (cf. Eq. (4)).  $\sin^2 \psi^*$  is given by a ratio of elastic constants and therefore the sensitivity to errors in the elastic constants may be relatively moderate, e.g. if errors in the different elastic constants, relative to their real values, are about equal.

If the specimen temperature has been accurately calibrated, a determination of the temperature-dependent coefficient of thermal expansion of film (and/or substrate) is possible according to:

$$\alpha_F(T) \equiv \frac{1}{a_0(T)} \frac{\partial a_0(T)}{\partial T}. \quad (6)$$

## 2.3 Experimental and data evaluation

Pd and Ni thin films were deposited at room temperature onto Si (100) wafers, covered with thin amorphous SiO<sub>2</sub> and Si<sub>3</sub>N<sub>4</sub> diffusion barrier layers (each 50 nm thick), by DC magnetron sputtering under ultra high vacuum conditions (base pressure about  $1 \times 10^{-10}$  mbar). Each of the thin films had a thickness of 50 nm. Prior to the deposition, the substrates were sputter-cleaned for about 1 minute with Ar ions of kinetic energy 100 eV. During the film deposition, the substrate holder was rotating and the chamber pressure was maintained at  $2 \times 10^{-4}$  mbar employing Ar as a sputter gas. The Pd sputter source was operated at 100 W; the Ni sputter source was operated at 200 W.

X-ray diffraction measurements were performed employing a Bruker D8 Discover diffractometer equipped with an Eulerian cradle. Cu-K $\alpha$  radiation emerging from the focus of a rotating-anode X-ray source (Bruker TXS) operating at 50 kV and 20 mA has been converted into a monochromated and quasi-parallel beam by a collimating X-ray mirror (Xenocs) [33,34]. The diffracted beam passed a parallel plate collimator (acceptance angle 0.23°) before being detected by a scintillation counter. For in-situ, temperature dependent, experiments a heating/cooling chamber DCS350 (Anton Paar) was mounted on the Eulerian cradle (see also [18]). It is possible with this equipment to make in-situ experiments within a temperature range between -100 °C and 350 °C and at pressures of the order of  $10^{-3}$  mbar.

The specimens were first cooled from room temperature (25 °C) to -100 °C, then heated back to room temperature, afterwards heated from room temperature to 250 °C and finally cooled back to room temperature. The increments in temperature were taken as 25 °C throughout the entire heat treatment. The temperature cycle from room temperature to 250 °C and vice versa was repeated four times for each specimen. The  $2\theta$  ranges employed to record the {111} reflections of the layers were 37.5°-42.5° for Pd and 41.5°-46.5° for Ni. For every temperature step,  $2\theta$  scans were performed at two tilt angles,  $\psi=0^\circ$  and  $\psi=70.54^\circ$ , employing the side-inclination method [15]. This resulted in a duration of 22 minutes for one stress measurement. A delay time of 5 minutes was scheduled for each temperature step in order to guarantee temperature homogenization.

Pole figure sections of the as-deposited Pd layer and as-deposited and heat treated Ni layer were obtained by plotting the integrated intensities of the {111} reflections as function of tilt angle  $\psi$ . At each  $\psi$ ,  $2\theta$  was continuously varied from 37° to 43° and from 41.5° to 47.5° with a rate of 0.01 °/s for the Pd and Ni layers, respectively.

Calibration of the heating/cooling chamber was performed by a resistance thermometry method (the details of this method have been explained in Ref. [18]) independently of the calibration procedure proposed in this paper (i.e. employing the thin film as a reference sample). In order to determine the instrumental broadening of the diffractometer as function of diffraction angle  $2\theta$ , 13  $hkl$  reflections of a  $\text{LaB}_6$  (NIST SRM660a) standard powder sample were measured.

Pearson VII functions were fitted to each reflection by using the software Profit 1.0 from Philips in order to determine peak parameters such as peak maximum position, shape parameter, integral breadth, Voigt parameter and peak asymmetry parameter [35].

Changes of crystallite size and microstrain during the thermal cycles were monitored by single-line broadening analysis with the diffraction vector oriented perpendicular to the specimen surface [36-38]. More sophisticated methods for the analysis of the diffraction line broadening exist. However, the single-line method can be employed relatively easily and rapidly (as only one particular diffraction line has to be recorded) to obtain estimates for the size of the coherently diffracting domains  $D$  and the microstrain  $\varepsilon$  [36-38] and, in particular, to observe the evolution of these parameters in-situ as function of temperature.

## 2.4 Results and discussion

### 2.4.1 Crystallographic textures of the specimens

The pole figure sections shown in Fig. 2.1 indicate that both specimens have a strong and sharp  $\{111\}$  fibre texture in the as-deposited state. This justifies employing the CGM for the residual stress analysis (cf. Section 2.2.1). The strength of the  $\{111\}$  texture gets even more pronounced after the heating cycles. Thus, the CGM can also be applied to the heat treated specimens (cf. Fig. 2.1 (b)).

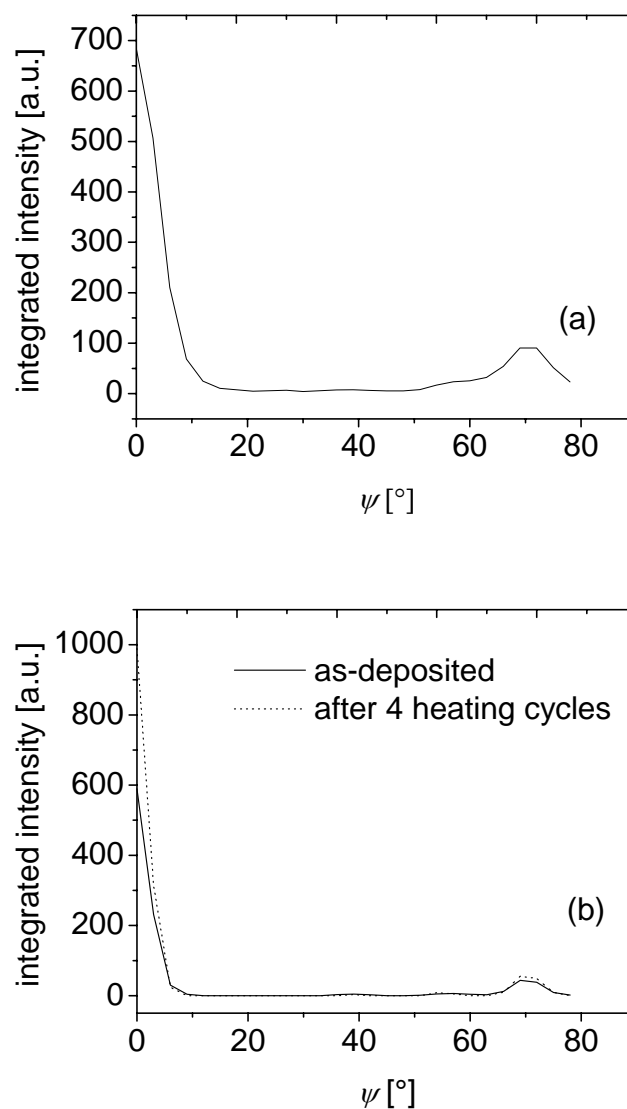


**Fig. 2.1:**  $\{111\}$  pole figure section for (a) the as-deposited Pd layer (b) the as-deposited and the heat treated Ni layers.

### **2.4.2 In-situ temperature calibration and determination of coefficient of thermal expansion**

The state of stress at room temperature has been found to be planar and rotationally symmetric. Hence, all following diffraction measurements were conducted at an arbitrary rotation angle  $\varphi$  (cf. Section 2.2.1).

In the following sections, two different temperatures are used. The first one is the specimen temperature,  $T$ , as obtained by direct measurement (resistance thermometry; see Section 2.3 and Ref. [18]). The other one is the calculated temperature,  $T_{\text{calc}}$ , derived from the strain-free lattice constants employing Eq. (5) using the recommended thermal expansion function for Pd [39] and thermal expansion data of Altman *et al.* [40] for Ni layer (the recommended thermal expansion function for Ni in Ref. [39] is not valid for temperatures below room temperature). The temperature mentioned throughout the article is the specimen temperature,  $T$ , unless otherwise stated.

Pd and Ni specimens have been thermally cycled between room temperature (25 °C) and -100 °C. The {111} reflection has been measured and the strain-free lattice constants have been obtained by interpolation in the  $d_{\psi} \sin^2 \psi$  plots at  $\sin^2 \psi^*$  (cf. Section 2.2.1) employing the crystallite group method. The results are shown in Fig. 2.2.

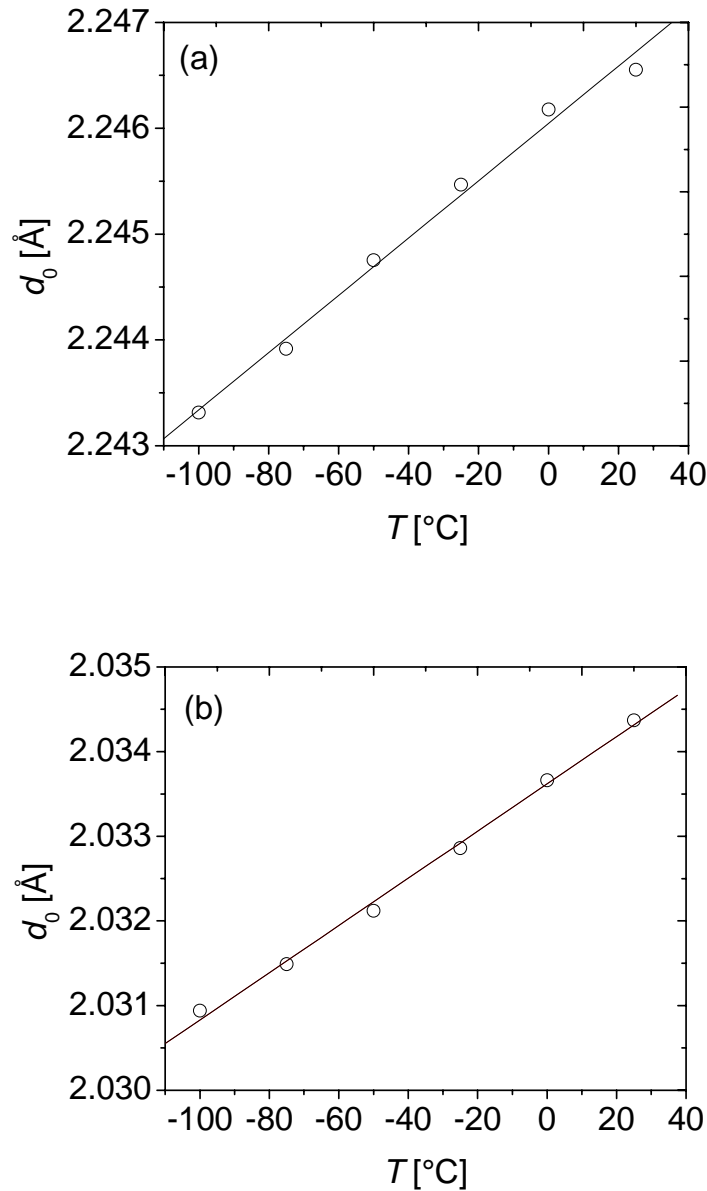


**Fig. 2.2:** Plot of  $d_0$  versus specimen temperature for (a) Pd and (b) Ni layers. Error bars have not been shown as their size is about the size of the symbols used.

The Pd specimen temperature,  $T$ , and calculated temperature,  $T_{\text{calc}}$ , have been plotted along the abscissa and ordinate in Fig. 2.3 (a), respectively. The line drawn in Fig. 2.3 (a) pertains to (possible) equality of  $T$  and  $T_{\text{calc}}$ . It follows that the temperature obtained by the in-situ temperature calibration,  $T_{\text{calc}}$ , agrees reasonably well with the specimen temperature as measured directly,  $T$ .

Similar results for the Ni specimen are presented in Fig. 2.3 (b). Contrary to the case of Pd (Fig. 2.3 (a)),  $T$  and  $T_{\text{calc}}$  differ significantly.

From linear fits to the data presented in Fig. 2.2 the average CTEs in the investigated temperature interval have been calculated. The results have been gathered in Table 2.1. Consistent with the above discussion, a relatively good agreement of the measured CTE and the CTE taken from literature is observed for the Pd layer, whereas the agreement is considerably less good for the Ni layer.

**Table 2.1:** The coefficients of thermal expansion for Pd and Ni layers. Experimental averages and literature averages for the temperature range between room temperature and -100 °C. The recommended function [39] and the data of Altman *et al.* [40] were used for the Pd layer and the Ni layer, respectively (see text).

<b>Coefficients of thermal expansion calculated for Pd and Ni layers</b>			
<b>Pd</b>		<b>Ni</b>	
Experimental average [1/°C]	Literature average [1/°C]	Experimental average [1/°C]	Literature average [1/°C]
$(12.0 \pm 0.6) \times 10^{-6}$	$11.2 \times 10^{-6}$	$(13.7 \pm 0.4) \times 10^{-6}$	$12.4 \times 10^{-6}$

It is suggested here that the apparent deviations obtained for the Ni *layer* are a consequence of the inappropriateness of the CTE of *bulk* Ni employed for calculation of the ordinate values in Fig. 2.3(b). This has been discussed in detail elsewhere [20]. This finding demonstrates that thin films (and nanocrystalline materials in general) can have CTE values significantly different from the literature data for bulk materials.



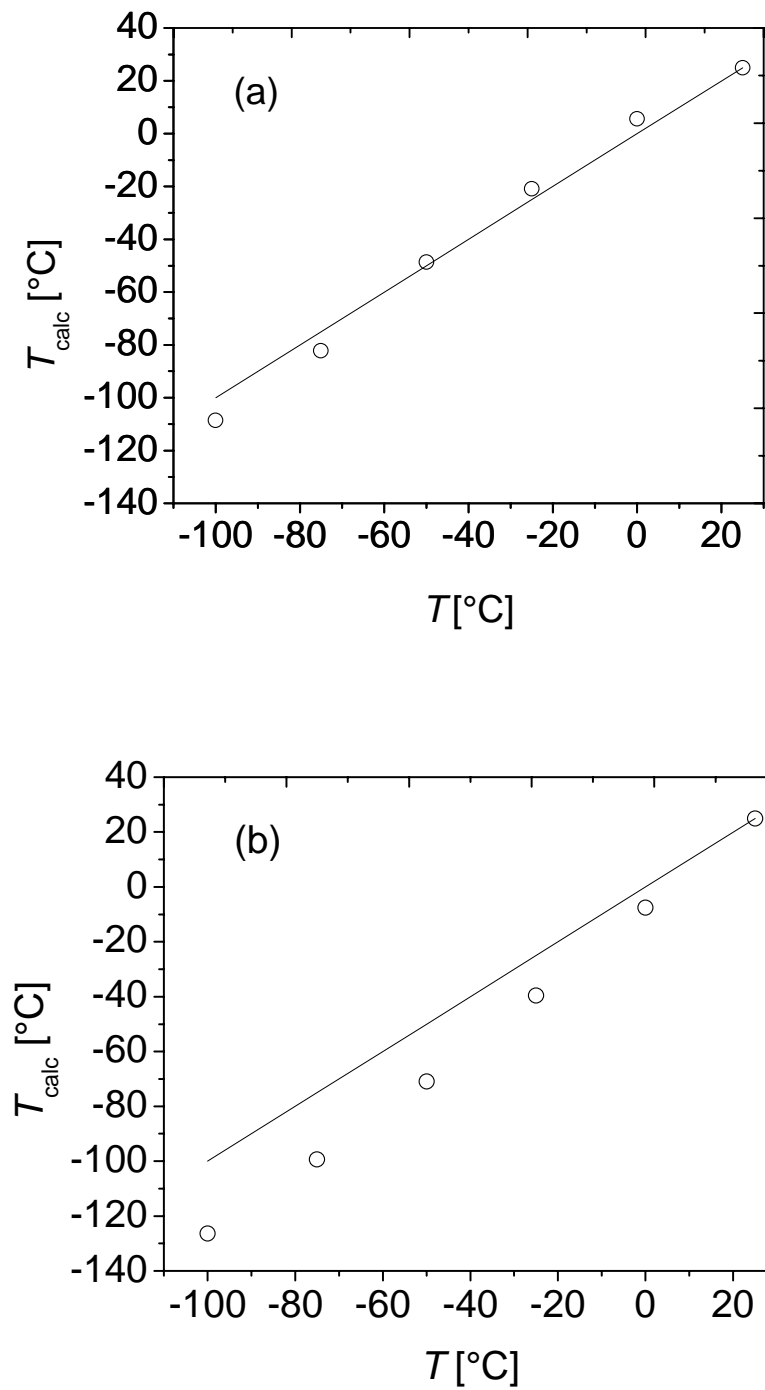


**Fig. 2.3:** Temperature,  $T_{\text{calc}}$ , calculated from measured  $d_0$  values of (a) the Pd layer (b) the Ni layer versus the specimen temperature,  $T$ . Error bars have not been shown as their size is about the size of the symbols used.

### **2.4.3 Use of temperatures below ambient temperature for characterizing the elastic behaviour of the film/substrate assembly**

A Ni thin film has been thermally cycled between room temperature and -100 °C. Afterwards, it was cycled between room temperature and 250 °C four times. At each temperature diffraction stress measurements were performed on the basis of the CGM (cf. Section 2.3). The results are shown in Figs. 2.4 and 2.5.

The linear extrapolation of the thermoelastic behaviour observed during cooling, below room temperature, to temperatures above ambient temperature demonstrates unambiguously that already upon heating to temperatures as low as 25 °C-50 °C, the induced stress change cannot be attributed entirely to the thermal misfit of the film and the substrate (see Fig. 2.4). Evidently, thermally activated relaxation of the compressive thermal stress in the film, originating from the increasing temperature and the higher CTE of the film than the CTE of the substrate, occurs immediately above ambient temperature or a thermally activated process becomes active that results in the generation of a tensile stress contribution. The magnitude of the amount of stress relaxation above room temperature or the amount of tensile stress generated can be estimated from the difference between the observed stress,  $\sigma^{\text{obs}}$ , and the expected stress according to the linear extrapolation of the stress evolution below room temperature,  $\sigma^{\text{extp}}$ ; results are shown in Fig. 2.6. The difference  $\sigma^{\text{obs}} - \sigma^{\text{extp}}$  is substantial upon heating above ambient temperature and reaches a plateau at about 225 °C (Fig. 2.6).

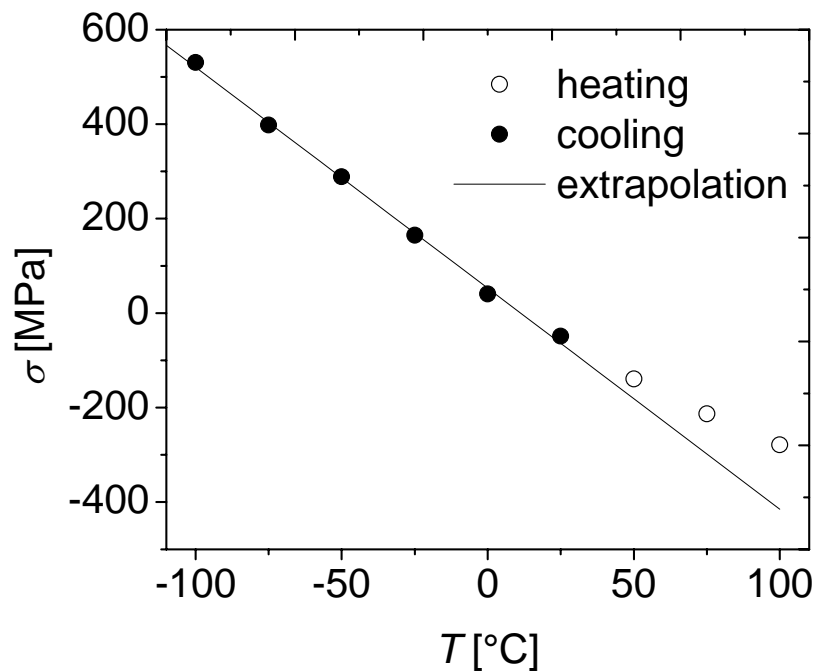


**Fig. 2.4:** Stress versus temperature plots for the Ni layer in the temperature range between  $-100\text{ }^{\circ}\text{C}$  and  $100\text{ }^{\circ}\text{C}$ . The solid line is the linear extrapolation of the cooling data to elevated temperatures. Error bars have not been shown as their size is about the size of the symbols used.

The corresponding changes of crystallite size  $D$  and microstrain  $\varepsilon$  (cf. Section 2.3) in the first heating cycle have been presented in Fig. 2.7, recognizing that  $\sigma^{\text{obs}} - \sigma^{\text{exp}}$  is a consequence of relaxation associated with grain growth and/or a consequence of the annihilation of crystalline defects (see further).

As is evident from Fig. 2.7, the heating cycle can be subdivided into two segments. Whereas the annihilation of crystal defects, exhibited by a decrease of the microstrain, proceeds essentially from the beginning of the heating (Fig. 2.7 (b)), growth of the coherently diffracting domains in the direction perpendicular to the film surface starts at a temperature of about  $100\text{ }^{\circ}\text{C}$  (Fig. 2.7 (a)). It appears that in particular upon onset of grain growth a drastic increase of  $\sigma^{\text{obs}} - \sigma^{\text{exp}}$  occurs (cf. Figs. 2.6 and 2.7).

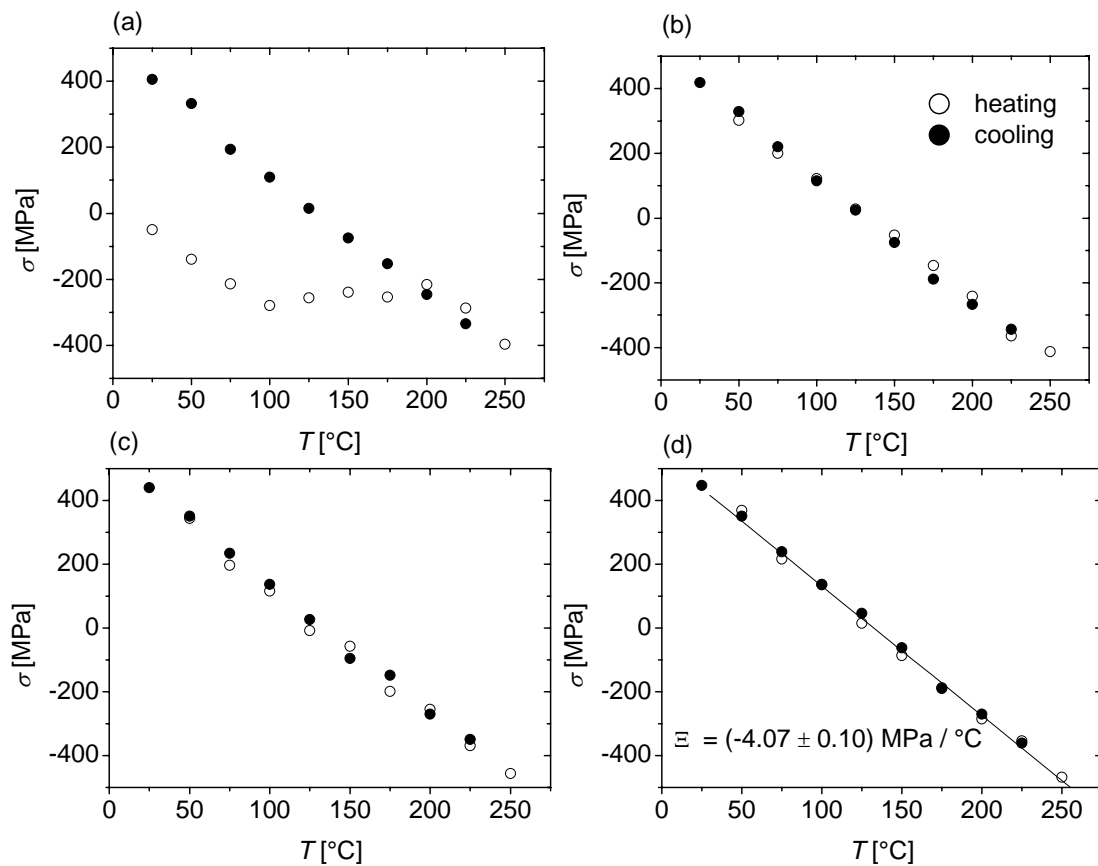


**Fig. 2.5:** Stress versus temperature plots for the Ni layer for four heating cycles between room temperature and 250 °C. (a) First cycle (b) Second cycle (c) Third cycle (d) Fourth cycle (The value of the thermoelastic slope,  $\Xi$ , for the fourth cycle has also been indicated in the figure). Error bars have not been shown as their size is about the size of the symbols used.

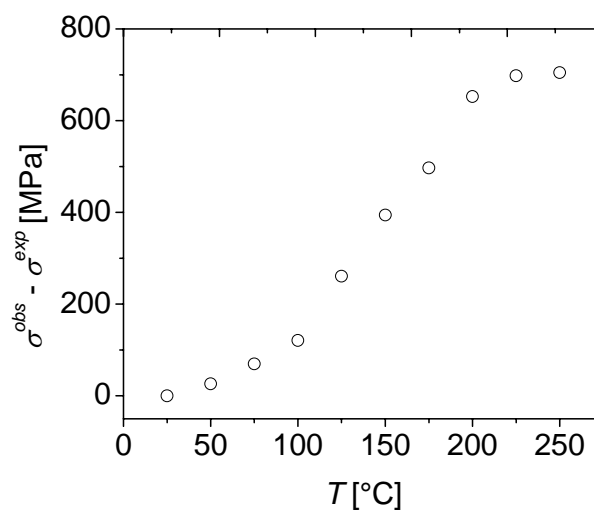


**Fig. 2.6:** The difference between the observed stress and the expected stress (according to the linear extrapolation of the cooling data to elevated temperatures) in the heating part of the first cycle of the Ni layer. Error bars have not been shown as their size is about the size of the symbols used.

Adopting a simple treatment proposed by Doerner and Nix [3] (extending the treatment by Chaudhari [41]), that correlates the generation of tensile stress to the elimination of excess volume in the grain boundaries during grain growth, it has been shown here that the amount of tensile stress,  $\sigma^{\text{obs}} - \sigma^{\text{exp}}$  (700 MPa) arising during the first heating cycle in the Ni layer is well compatible with a tensile stress contribution due to the increase of crystallite size as determined from the diffraction-line broadening analysis, if the excess volume per unit area of a grain boundary is assumed to be half of an atomic diameter.

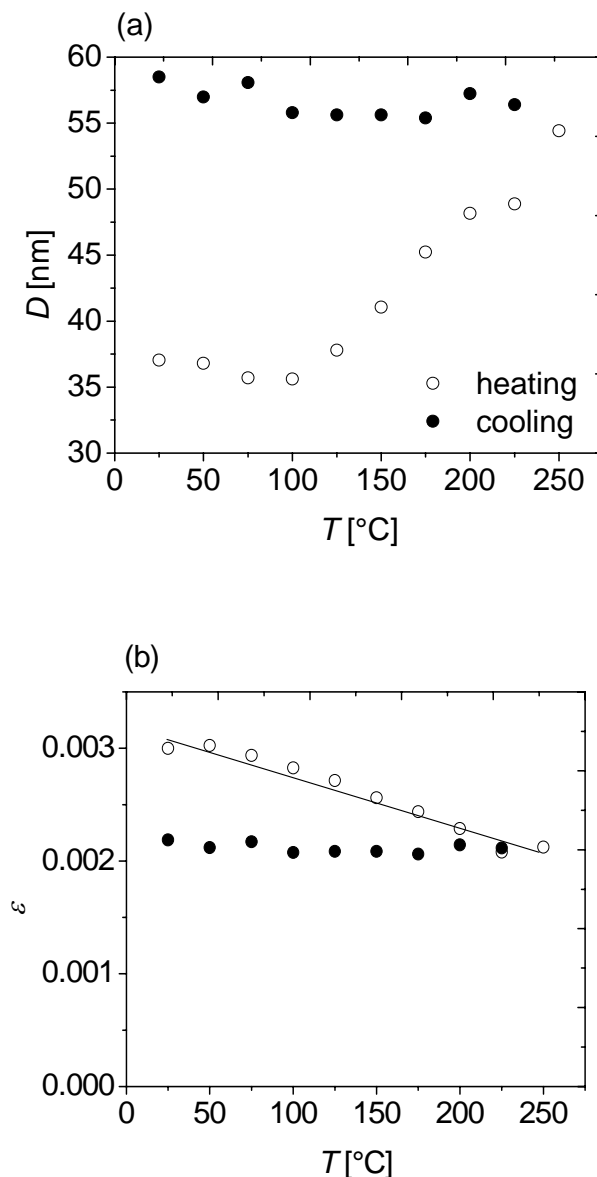


**Fig. 2.7:** Plots of domain size (a) and microstrain (b) versus temperature obtained by the single-line method for the first heating cycle of the Ni layer.

After heating to 250 °C, a stable microstructure has developed (as evidenced by achieved constancy of diffraction-line position and shape) and the first heating segment is

followed by a cooling segment and heating and cooling cycles exhibiting fully linear behaviour consistent with the (bulk values of the) CTEs of the Ni layer and the substrate (cf. Figs. 2.5 (b)-(d)). The measured thermoelastic slope for the fourth heating cycle is  $-4.07 \text{ MPa}/^\circ\text{C}$  (cf. Fig. 2.5(d)), which matches the theoretically predicted thermoelastic slope for perfectly  $\{111\}$  fibre-textured bulk Ni ( $-4.08 \text{ MPa}/^\circ\text{C}$ ; cf. Table 2.2) taken as a model for the Ni layer with its sharp and strong  $\{111\}$  fibre texture (see Fig. 2.1 (b)).

#### **2.4.4 Measurement of the thermoelastic slope of the film/substrate assembly**

The average thermoelastic slope (TES),  $\Xi$ , ( $=\frac{\partial\sigma(T)}{\partial T}$ ) for Pd and Ni layers thermally cycled between room temperature ( $25^\circ\text{C}$ ) and  $-100^\circ\text{C}$  has been determined in this temperature interval from the linear fit to the stress vs. temperature data (Fig. 2.8). The results have been gathered in Table 2.2, together with the corresponding results calculated on the basis of literature data for CTEs [39,40,42] (The recommended linear expansion functions were used for Pd and Si [39], while the data of Altman *et al.* [40] were employed for Ni). Temperature dependence of the elastic constants in the temperature range ( $-100^\circ\text{C}$ - $25^\circ\text{C}$ ) was neglected for this calculation since the error introduced by this assumption is less than 5 % [43].

Whereas a relatively good agreement between measured and expected data for the TES occurs for the Pd film (for the case of  $\{111\}$  fibre texture), the agreement is considerably less good for the Ni film (Table 2.2). The considerable deviation obtained for the Ni layer is a consequence of the inappropriateness of the CTE of Ni taken from the literature, due to the small crystallite size of the as-deposited Ni layer (see discussion in Section 2.4.2). The crystallite size of Pd is relatively large (about 50 nm, as obtained from single-line broadening analysis) leading to a CTE close to its literature value. On the other hand, the crystallite size of Ni is about 35 nm: The experimentally determined CTE of as-deposited Ni ( $13.7\times 10^{-6} \text{ 1}/^\circ\text{C}$ ) is distinctly larger than the corresponding literature value ( $12.4\times 10^{-6} \text{ 1}/^\circ\text{C}$ ) and a too small TES is calculated adopting the literature value for the CTE. As a general conclusion it follows that employing the literature CTE obtained for coarse-grained specimens of a certain material, as the CTE for a thin film (nanosized grains) of the same material, leads to pronouncedly erroneous results for thermoelastic properties (e.g. TES) of thin films.

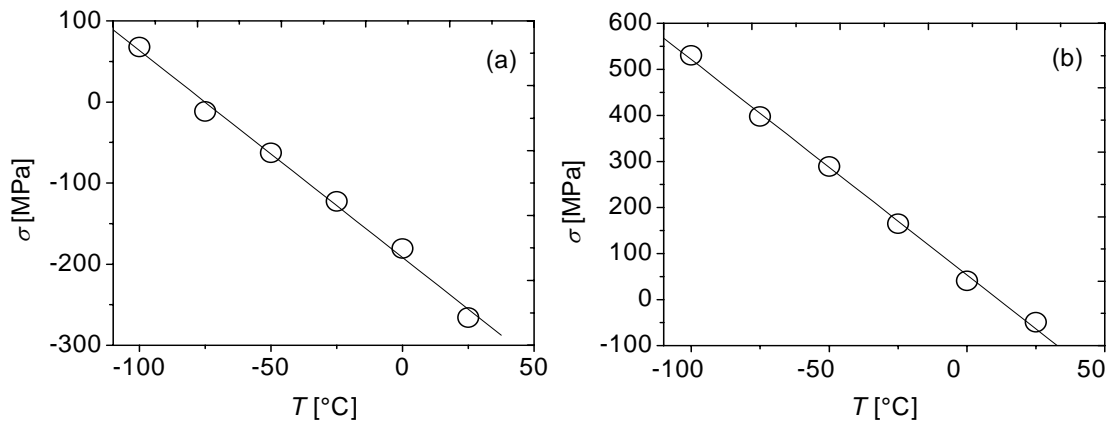


**Fig. 2.8** Stress versus temperature plots for the (a) Pd and (b) Ni layers during cooling to  $-100\text{ }^{\circ}\text{C}$ . Error bars have not been shown as their size is about the size of the symbols used.

**Table 2.2:** Measured thermoelastic slopes of Pd and Ni single layers during cooling to  $-100\text{ }^{\circ}\text{C}$ . The residual stresses in both layers were obtained by employing CGM (see Section 2.3). The calculated thermoelastic slopes of the layers for the cases of polycrystalline (no preferred orientation) layers and layers with perfect  $\{111\}$  fiber texture have also been given [3,39,40,42].

measured thermoelastic slopes			
Pd		Ni	
CGM [MPa/ $^{\circ}\text{C}$ ]		CGM [MPa/ $^{\circ}\text{C}$ ]	
$-2.55 \pm 0.10$		$-4.68 \pm 0.11$	
calculated thermoelastic slopes			
Pd		Ni	
Polycrystalline [MPa/ $^{\circ}\text{C}$ ]	Perfect $\{111\}$ Fiber Textured [MPa/ $^{\circ}\text{C}$ ]	Polycrystalline [MPa/ $^{\circ}\text{C}$ ]	Perfect $\{111\}$ Fiber Textured [MPa/ $^{\circ}\text{C}$ ]
-1.85	-2.69	-3.04	-4.08

## 2.5 Conclusions

- Strain-free lattice constants deduced from residual stress measurements can be successfully used to measure average CTEs (if temperature calibration of the specimen was performed) of thin films (nanosized grains).
- Experimental distinction of the thermal stresses, due to a difference between the CTEs of film and substrate, and relaxation of stress due to thermally activated processes, as annihilation of crystal defects, and build up of (tensile) stress due to grain growth, both *above* ambient temperature, can be realized by investigating the stress-temperature relationship at temperatures *below* ambient temperature, where these thermally activated processes are not operative normally.
- Thermoelastic slopes of metal thin films can be measured reliably by cooling the specimen below room temperature without any additional heat treatments after the deposition (as usually applied to stabilize the as-deposited structure), since thermally activated processes are inhibited at these temperatures. However, the CTEs of thin films (nanosized grains) differ significantly from literature values pertaining to coarse-grained bulk material.

## Acknowledgement

We thank Mr F. Thiele and Dr G. Richter (Max Planck Institute for Metals Research, Stuttgart, Germany) for the specimen production.



## References

- [1] B. Okolo, P. Lamparter, U. Welzel, T. Wagner and E. J. Mittemeijer, *Thin Solid Films* **474**, 50 (2005).
- [2] B. Okolo, P. Lamparter, U. Welzel and E. J. Mittemeijer, *J. Appl. Phys.* **95**, 466 (2004).
- [3] M. F. Doerner and W. D. Nix, *Crit. Rev. Solid State* **14**, 225 (1988).
- [4] L. B. Freund and S. Suresh, *Thin Film Materials Stress, Defect Formation and Surface Evolution*, (Cambridge Univ. Press, Cambridge, 2003).
- [5] G. C. A. M. Janssen, *Thin Solid Films* **515**, 6654 (2007).
- [6] R. Messier and J. E. Yehoda, *J. Appl. Phys.* **58**, 3739 (1985).
- [7] R. Messier, A. P. Giri and R. A. Roy, *J. Vac. Sci. Technol. A* **2**, 500 (1984).
- [8] H. T. G. Hentzell, C. R. M. Grovenor and D. A. Smith, *J. Vac. Sci. Technol. A* **2**, 218 (1984).
- [9] P. B. Barna and M. Adamik, *Thin Solid Films* **317**, 27 (1998).
- [10] K. M. Chow, W. Y. Ng and L. K. Yeung, *Surf. Coat. Technol.* **105**, 56 (1998).
- [11] G. Lucadamo, K. Barmak, D. T. Carpenter and J. M. Rickman, *Acta Mater.* **49**, 2813 (2001).
- [12] V. Ramaswamy, W. D. Nix and B. M. Clemens, *Scripta Mater.* **50**, 711 (2004).
- [13] U. Welzel, P. Lamparter, M. Leoni and E. J. Mittemeijer, *Mater. Sci. Forum* **347**, 405 (2000).
- [14] U. Welzel, P. Lamparter and E. J. Mittemeijer, *Mater. Res. Soc. Symp. Proc.* **562**, 147 (1999).
- [15] U. Welzel, J. Ligot, P. Lamparter, A. C. Vermeulen and E. J. Mittemeijer, *J. Appl. Cryst.* **38**, 1 (2005).
- [16] V. Hauk, *Structural and Residual Stress Analysis by Nondestructive Methods Evaluation, Application, Assessment*, (Elsevier, Amsterdam, 1997).
- [17] I. C. Noyan and J. B. Cohen, *Residual Stress*, (Springer-Verlag, Berlin, 1987).
- [18] M. Wohlschlägel, U. Welzel, G. Maier and E. J. Mittemeijer, *J. Appl. Cryst.* **39**, 194 (2006).
- [19] R. Resel, E. Tamas, B. Sonderegger, P. Hofbauer and J. Keckes, *J. Appl. Cryst.* **36**, 80 (2003).
- [20] Y. Kuru, M. Wohlschlägel, U. Welzel and E. J. Mittemeijer, *Appl. Phys. Lett.* **90**, 243113 (2007).

- [21] M. Beck and E. J. Mittemeijer, *J. Appl. Cryst.* **35**, 103 (2002).
- [22] W. D. Nix, *Metall. Trans. A* **20A**, 2217 (1989).
- [23] A. C. Vermeulen, R. Delhez, Th. H. de Keijser and E. J. Mittemeijer, *J. Appl. Phys.* **77**, 5026 (1995).
- [24] U. Welzel and E. J. Mittemeijer, *J. Appl. Phys.* **93**, 9001 (2003).
- [25] P. F. Willemse and B. P. Naughton, *Mater. Sci. Technol.* **1**, 41 (1985).
- [26] P. F. Willemse, B. P. Naughton and C. A. Verbraak, *Mater. Sci. Eng.* **56**, 25 (1982).
- [27] V. Hauk and G. Vaessen, *Z. Metallkd.* **72**, 102 (1985).
- [28] V. Hauk, *Adv. X-ray Anal.* **29**, 1 (1986).
- [29] V. Hauk and R. Oudelhoven, *Z. Metallkd.* **79**, 41 (1988).
- [30] H. U. Baron and V. Hauk, *Z. Metallkd.* **79**, 127 (1988).
- [31] U. Welzel and E. J. Mittemeijer, *Mater. Sci. Forum* **443**, 131 (2004).
- [32] R. O. Simmons and R. W. Balluffi, *Phys. Rev.* **119**, 600 (1960).
- [33] M. Wohlschlägel, T. U. Schüllli, B. Lantz and U. Welzel, *J. Appl. Cryst.* **41**, 124 (2008).
- [34] M. Wohlschlägel, T. U. Schüllli, G. Maier, U. Welzel and E. J. Mittemeijer, *Z. Kristallogr. Suppl.* **26**, 147 (2007).
- [35] *Profit User's Guide*, (Philips Analytical X-ray, Delft, 1996).
- [36] R. Delhez, Th. H. de Keijser and E. J. Mittemeijer, *Fresen. Z. Anal. Chem.* **312**, 1 (1982).
- [37] Th. H. de Keijser, J. I. Langford, E. J. Mittemeijer and A. B. P. Vogels, *J. Appl. Cryst.* **15**, 308 (1982).
- [38] E. J. Mittemeijer and P. Scardi, *Diffraction Analysis of the Microstructure of Materials*, (Springer, Berlin, 2004).
- [39] Y. S. Touloukian, *Thermal Expansion: Metallic Elements and Alloys*, (IFI/Plenum, New York, 1975).
- [40] H. W. Altman, T. Rubin and H. L. Johnston, *Cryogenic Laboratory Rept. OSU-TR-264-27*, (Ohio State University, Columbus, 1954).
- [41] P. Chaudhari, *Vac. Sci. Technol.* **9**, 520 (1972).
- [42] W. F. Gale and T. C. Totemeier, *Smithells Metals Reference Book*, (Elsevier, Amsterdam, 2004).
- [43] R. Bechmann and R. F. S. Hearmon, *Landolt-Börnstein: Elastic, piezoelectric, piezooptic and electrooptic constants of crystals*, (Springer-Verlag, Berlin, 1966).

## Chapter 3

# Crystal size dependence of the coefficient of thermal expansion of metals

*Y. Kuru, M. Wohlschlägel, U. Welzel and E.J. Mittemeijer*

### Abstract

The coefficients of thermal expansion (CTE) of polycrystalline Ni and Cu thin films have been investigated employing temperature-dependent X-ray diffraction measurements of lattice parameters. Great care has been taken to exclude effects of in particular microstructural relaxation and mechanical stresses on the dependences of the lattice parameters on temperature. The CTEs determined in the as-deposited condition, characterised by grain sizes in the range of 25-35 nm, are considerably (about 10%) larger than the corresponding literature values of bulk materials. Heat treating the specimens at moderate temperatures induced grain growth and a decrease of the crystalline imperfection. After the heat treatment, the CTEs determined for the thin films had reduced considerably and had become equal to (Ni) or approached (Cu) the corresponding literature data for bulk materials.

### 3.1 Introduction

Nanocrystalline materials are of fundamental scientific interest as their physical properties can differ considerably from those of corresponding bulk materials [1-7]. The coefficient of thermal expansion (CTE) of nanocrystalline materials has been investigated both theoretically and experimentally in a number of studies. The findings can be reviewed as follows: Whereas theoretical studies generally conclude that the CTE should increase, from the value for coarse-grained materials, with decreasing crystallite size [8,9], inconsistent experimental results have been obtained: (i) the CTE would be independent of the crystallite size [10-14]; (ii) the CTE would increase with decreasing crystallite size [15-17]; (iii) the CTE would depend on the crystallite size (and, possibly, additional microstructural parameters) and could be both smaller and larger than the CTE of coarse-grained materials [18].

This inconclusive nature of the previous results about the crystallite-size dependence of the CTE may be related to the following experimental, not always recognized, pitfalls: (i) The presence of residual stresses and their variation with temperature in a thin film specimen or in a specimen prepared by techniques like severe plastic deformation and consolidation under an ultrahigh pressure, can affect significantly the lattice parameter as measured in (X-ray) diffraction investigations (e.g. in Refs. [19] and [20]). (ii) For (non-cubic) materials with anisotropic CTEs the occurrence of crystallographic texture affects the macroscopic, mechanical CTE as measured by a technique as dilatometry (e.g. in the case of Se) [21]. (iii) Compositional changes (e.g. in multi-phase systems) and microstructural changes (as grain growth) can occur for a specimen investigated at elevated temperatures (e.g. in Ref. [15]). (iv) (Change of) porosity can be a source of error for CTE values measured by techniques involving the detection of macroscopic, mechanical length changes as dilatometry.

In this work, the following strategy has been adopted to avoid the above mentioned sources of error: X-ray diffraction measurements, insensitive to porosity, have been employed for measuring CTEs. Residual stresses have been considered and their effect on the measured diffraction line position has been separated from the effect of the thermal lattice expansion. High purity specimens consisting of cubic materials (for which the CTE is isotropic) have been used in order to avoid composition changes and complications arising from the presence of crystallographic texture. The measurements have been carried out below room temperature, to exclude the occurrence of thermally activated processes as grain growth, which has been shown here to be of cardinal importance.

## 3.2 Experimental

Ni and Cu thin films were deposited at room temperature on Si(100) wafers covered with thin amorphous SiO<sub>2</sub> and Si<sub>3</sub>N<sub>4</sub> barrier layers (each 50 nm thick) by DC magnetron sputtering (base pressure about  $1 \times 10^{-10}$  mbar) employing Ar (at  $2 \times 10^{-4}$  mbar) as a sputter gas. Each of the thin films had a thickness of 50 nm.

The as-deposited layers were mounted on a heating/cooling chamber for X-ray diffraction investigations (Anton Paar DCS350; for temperature calibration and further details, see Ref. [22]) attached to the Eulerian cradle of a Bruker D8 Discover parallel-beam diffractometer equipped with a rotating-anode Cu K $\alpha$  X-ray source (Bruker TXS), a collimating X-ray mirror (Xenocs) and a scintillation counter [23,24]. The specimens were cooled from room temperature (25 °C) to -100 °C with temperature steps of 25 °C. Residual stresses (i.e. the stress, planar and rotationally symmetric, parallel to the specimen surface  $\sigma$ ) were measured at every temperature step employing the crystallite group method (CGM) making use of the {111} reflection. The CGM, allowing direct use of the intrinsic single crystal elastic constants (SEC), was preferred over the traditional  $\sin^2\psi$ -analysis ( $\psi$  is the angle between the diffraction vector and the specimen surface normal) involving X-ray elastic constants, as both layers had strong and sharp {111} fibre textures [25]. The strain free lattice parameter ( $a_0$ ) at a given temperature was calculated from the interplanar spacing of the {111} lattice planes by interpolating at the strain-free direction  $\sin^2\psi^*$  calculated from the SEC [25]. This approach presupposes that the value of  $\sin^2\psi^*$  is neither affected by the temperature-dependence nor by a possibly occurring grain-size dependence of the SEC. This can be made likely considering that: (i)  $\sin^2\psi^*$  depends upon the ratio of sums and differences of the individual SEC (temperature/size-dependent changes then cancel at least partially); (ii) no significant grain-size dependence of the SEC is expected for grain sizes exceeding 20 nm [26,27].

For every temperature step, the {111} reflections were recorded at two tilt angles,  $\psi=0^\circ$  and  $\psi=70.54^\circ$ . The time required for one stress measurement was 22 minutes. A waiting time of 5 minutes was adopted upon arriving at the temperature of each temperature step in order to guarantee temperature homogenization.

### 3.3 Results and discussion

The average CTE values of the layers for the temperature range between 25 °C and -100 °C were obtained from the slope of plots of the (thermal) lattice strain ( $\varepsilon_{th} = \Delta a_0 / a_0^{25^\circ\text{C}}$ ) versus temperature. The results obtained in the as-deposited conditions have been gathered in Fig. 3.1. For the strain calculation, the strain at ambient temperature (25°C) was taken as zero. It follows that the CTEs for the Ni and Cu layers in as-deposited condition are considerably larger than the CTE value according to the literature for the same temperature range (cf. Table 3.1).

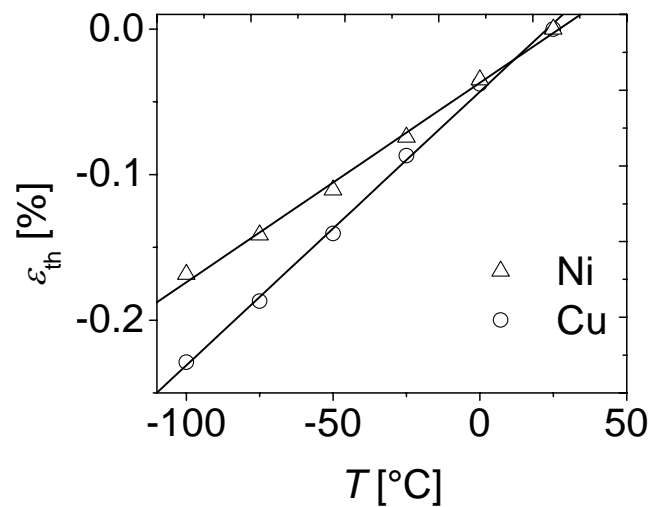


**Fig. 3.1:** The thermal strain,  $\varepsilon_{th}$  ( $=\Delta d/d_0$ , where  $d_0$  is the spacing of certain lattice planes at room temperature and  $\Delta d$  is the change in lattice-plane spacing when the temperature is changed by  $\Delta T$ ) for nickel (Ni) and copper (Cu) layers in the as-deposited nanocrystalline state as a function of temperature,  $T$ . The CTEs are the slopes of the fitted straight lines.

**Table 3.1:** The measured CTE values of the Ni and Cu thin films and the corresponding literature values [28]. TF: Thin film specimen, CG: Coarse-grained specimen.

	CTE of Ni [ $10^{-6} / ^\circ\text{C}$ ]	CTE of Cu [ $10^{-6} / ^\circ\text{C}$ ]
As-deposited (TF)	$13.7 \pm 0.4$	$18.8 \pm 0.4$
After heat treatment (TF)	$12.6 \pm 0.2$	$17.4 \pm 0.4$
Literature value (CG)	12.4	15.7
	$D$ of Ni [nm]	$D$ of Cu [nm]
As-deposited (TF)	37	26
After heat treatment (TF)	59	41

After the cooling cycles, the layers were heat treated according to a temperature cycle between room temperature and 250 °C (heating and cooling with temperature steps of 25 °C). This temperature cycle was repeated four times for both layers to establish a stabilized microstructure (as evidenced by achieved constancy of diffraction-line position and shape). It was verified that the heating cycles did not lead to a significant change of the strain-free lattice constant at room temperature. The evolution of the stress state during the thermal cycles was measured employing the CGM (for details see above; results not shown). Annealing the specimens at elevated temperatures during the heating cycles resulted even in a slight increase of the texture strength. Changes of crystallite size and microstrain during the thermal cycles were monitored by single line broadening analysis with the diffraction vector oriented perpendicular to the specimen surface (i.e.  $\psi=0^\circ$ ) [29-31]. Results are shown in Fig. 3.2. Whereas an increase of the crystallite size and a decrease of the microstrain were detected during the first temperature cycle, the crystallite size and microstrain did not show any further changes in the subsequent cycles. The increase of the crystallite size during the first heating cycle was paralleled by the emergence of a considerable tensile stress contribution in both layers superimposed upon the stress evolution resulting from the mismatch of the coefficients of thermal expansion of substrate and layer. Adopting a simple treatment proposed by Doerner and Nix [32] (extending the treatment by Chaudhari) [33], that ascribes the generation of tensile stress to the elimination of excess volume in the grain boundaries during grain growth, it was shown here that the amounts of tensile stress arising during the first heating cycle in both layers (700 MPa and 300 MPa for Ni and Cu layers, respectively) are well compatible with the increases of grain size as determined from the diffraction-line broadening analyses, if the excess volume per unit area of the grain boundary is taken about half of an atomic diameter.

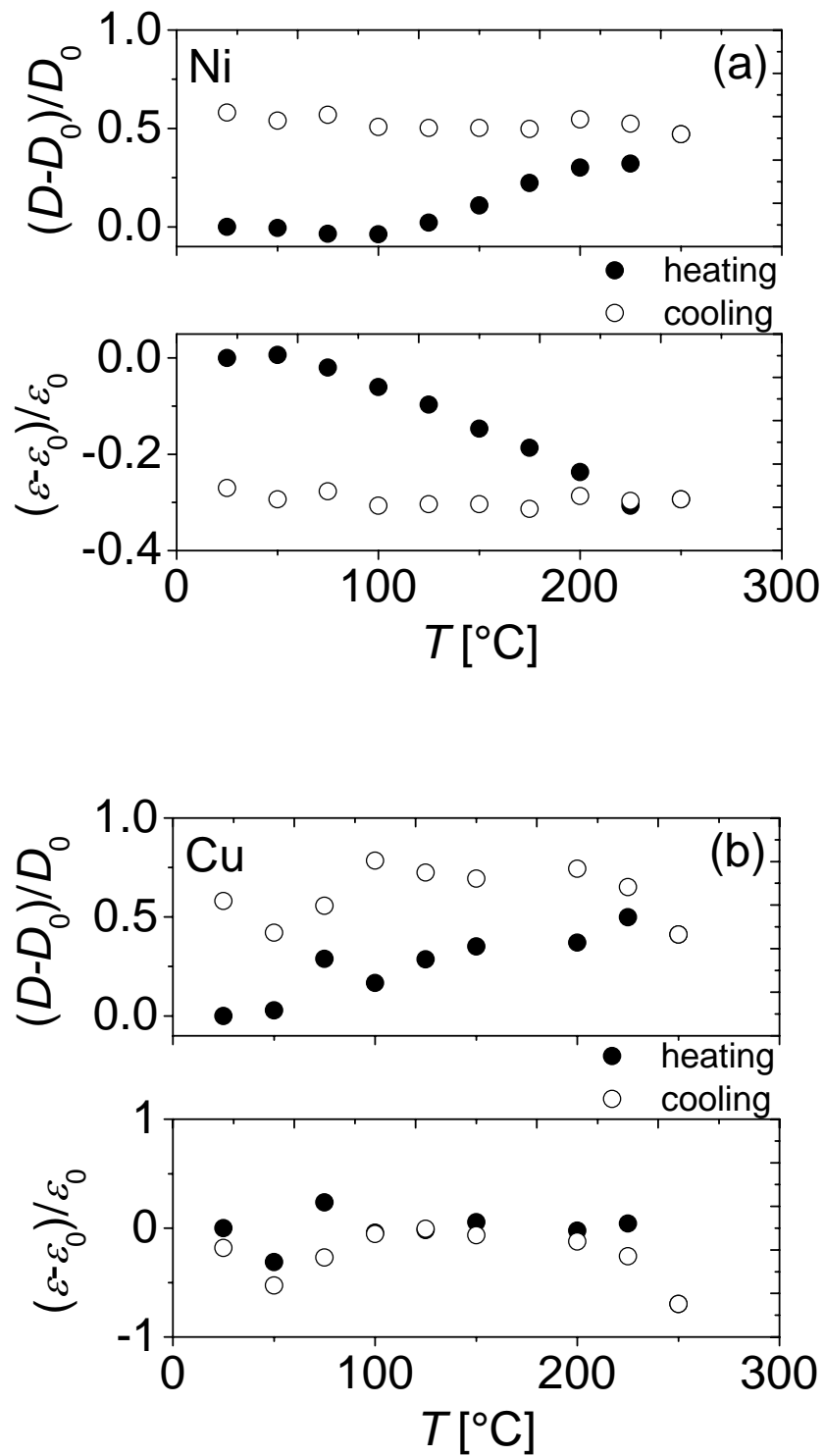


**Fig. 3.2:** Variation in crystallite size,  $(D-D_0)/D_0$ , and variation in microstrain,  $(\varepsilon-\varepsilon_0)/\varepsilon_0$ , versus temperature,  $T$ , for (a) Ni ( $D_0=37$  nm,  $\varepsilon_0=0.3$  %) and (b) Cu ( $D_0=26$  nm,  $\varepsilon_0=0.17$  %) layers during the first heating cycle between 25  $^{\circ}\text{C}$  and 250  $^{\circ}\text{C}$ .

After completing the heating cycles, the CTE values of the layers were again obtained for the temperature range between 25  $^{\circ}\text{C}$  and -100  $^{\circ}\text{C}$  from the slope of plots of the strain  $\varepsilon_{\text{th}}$



versus temperature. The results are shown in Fig. 3.3 (see also Table 3.1). It follows that upon heat treatment the CTEs for the Ni and Cu layers had reduced significantly: In accordance with an increase of the crystallite size of the Ni layer from about 35 nm to about 50 nm, a decrease of the CTE occurred from  $13.7 \times 10^{-6} \text{ 1/}^\circ\text{C}$  to  $12.6 \times 10^{-6} \text{ 1/}^\circ\text{C}$ . This last value is equal to the corresponding literature value within experimental accuracy (see Table 3.1) for the temperature range considered. In accordance with an increase of the crystallite size of the Cu layer from 25 nm to about 40 nm, a decrease of the CTE occurred from  $18.8 \times 10^{-6} \text{ 1/}^\circ\text{C}$  to  $17.4 \times 10^{-6} \text{ 1/}^\circ\text{C}$ . This last value is closer to but still larger than the corresponding literature value. Evidently, the crystallite size of the Cu layer at the end of the heat treatment is smaller than that of the Ni layer, which may explain that the CTE of the Cu film after the heat treatment is still larger than the literature value.

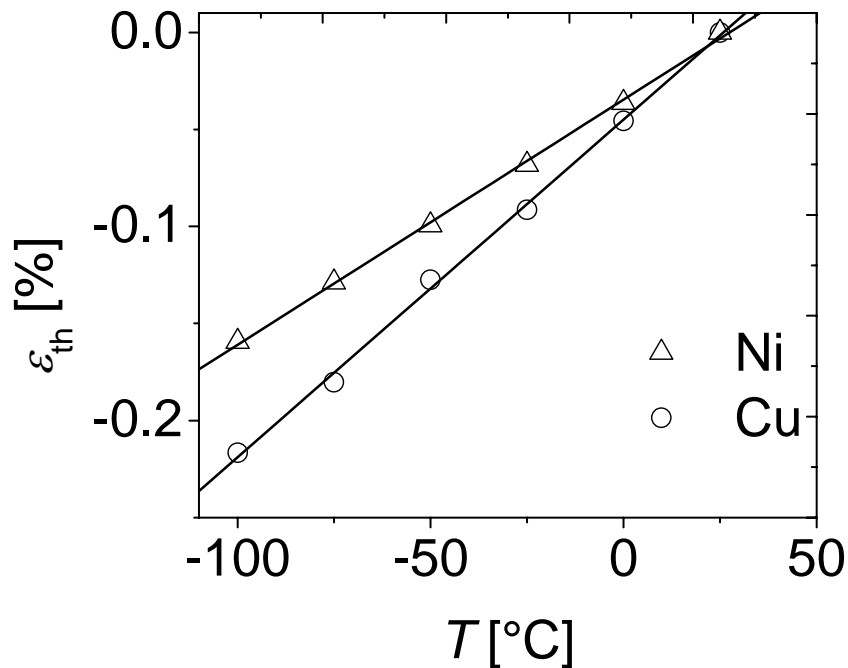


**Fig. 3.3:** The thermal strain,  $\epsilon_{th}$ , for nickel (Ni) and copper (Cu) layers as a function of temperature,  $T$ , after four heating cycles between 25 °C and 250 °C. The CTEs are the slopes of the fitted straight lines.

The findings obtained for the CTEs can be understood as follows: Atoms at the surface of a crystal or at an (incoherent) interface (grain boundary) are not saturated with respect to their state of bonding: their coordination number (i.e. the number of nearest neighbours) is less than for bulk atoms. As a consequence the curve of potential energy per atom versus interatomic distance for a surface/interface atom shows a less deep potential energy minimum well than for a bulk atom (cf. Fig. 3.4). The effect of a similar vibrational kinetic energy for

surface/interface and bulk atoms now has consequences of different extent. Evidently, the less deep potential energy minimum for the surface/interface atom, as compared to the bulk atom, leads to a larger atomic position variation due to thermal vibration for the surface/interface atom than for the bulk atom. Consequently, in view of the asymmetry of the potential energy minimum wells, the thermal expansion for the surface/interface atoms of the crystal is larger than for the bulk atoms. (Experimental proof that the above discussed potential energy well is less deep and moreover more asymmetric for surface atoms than for bulk atoms has been provided in Ref. [34].) The smaller a crystal, the larger the ratio of the number of surface/interface atoms and the number of bulk atoms. Hence, the smaller a crystal, the larger its *average* CTE.

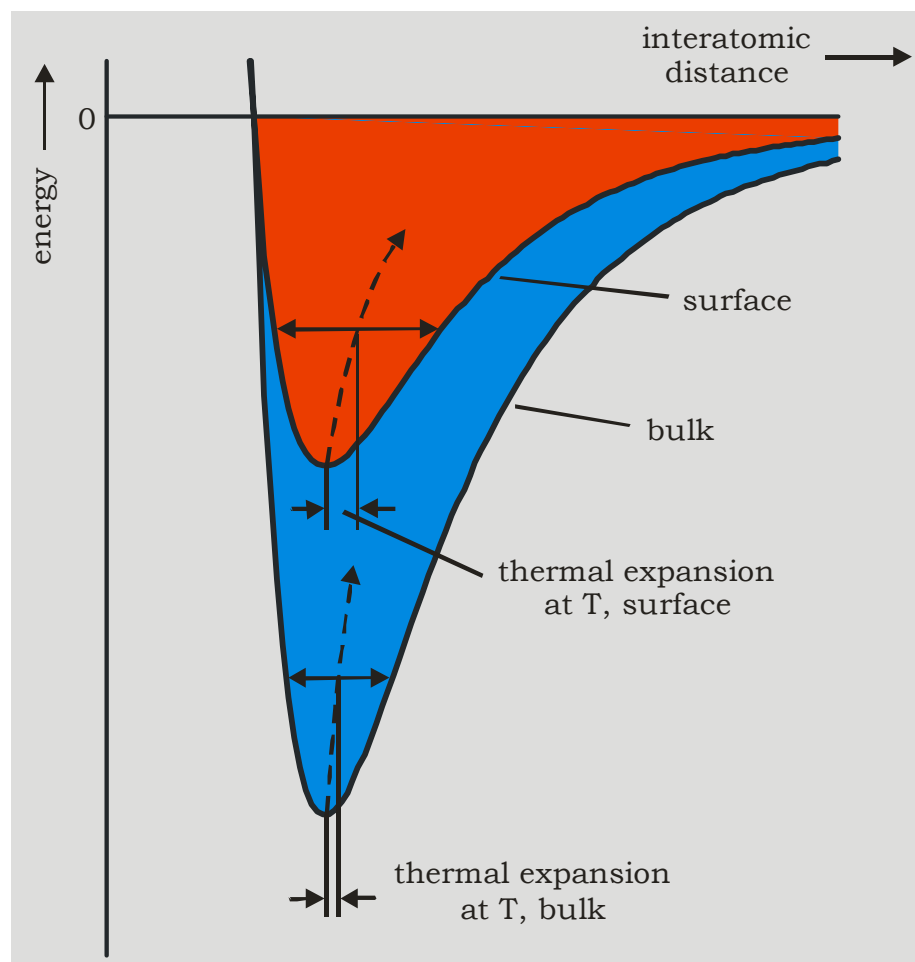


**Fig. 3.4:** Potential energy as a function of interatomic distance for bulk and surface atoms.

In conclusion, the dependence of the CTE on crystallite size has been proven conclusively, by avoiding interference of effects of porosity, preferred orientation and, in particular, residual stress and microstructural changes (occurring at and above room temperature in nanocrystalline thin films of metals). By an increase of crystallite size from 35

nm to 50 nm in a Ni thin film the CTE decreased by 8.0 %, thereby attaining its value for coarse-grained bulk material. For a Cu thin film, an increase of crystallite size from 25 nm to 40 nm led to a 7.4 % reduction in its CTE which then is closer to but still larger than the value for coarse-grained material. The initially larger difference with the CTE for coarse-grained, bulk material for the Cu layer, as compared with the Ni layer, and, after heat treatment, the remaining, although pronouncedly reduced, difference with the CTE for coarse-grained bulk material in case of only the Cu layer, may be related to smaller initial and final crystallite sizes for the Cu layer.

### **3.4 Conclusions**

It is concluded that the CTE of a material with a grain size in the nanometer range will generally be distinctly larger than the CTE of its conventional coarse-grained counterpart. This can have grave consequences for the interpretation of thermoelastic properties (e.g. biaxial modulus) of thin films; at the same time the possibility is now given to tune the CTE of a thin film by modifying its microstructure.

### **Acknowledgement**

We thank Mr F. Thiele and Dr G. Richter (Max Planck Institute for Metals Research, Stuttgart, Germany) for the specimen production.

## References

- [1] H. Gleiter, *Phase Transit.* **24-26**, 15 (1990).
- [2] R. Birringer, and H. Gleiter, *Advances in Materials Science, Encyclopedia of Materials Science and Engineering* (Pergamon Press, Oxford, 1988).
- [3] V. Yakamov, D. Wolf, S. R. Phillpot, A. K. Mukherjee, and H. Gleiter, *Nature Mater.* **1**, 45 (2002).
- [4] H. Van Swygenhoven, P. M. Derlet, and A. G. Froseth, *Nature Mater.* **3**, 399 (2004).
- [5] Z. Shan, E. A. Stach, J. M. K. Wiezorek, J. A. Knapp, D. M. Follstaedt, and S. X. Mao, *Science* **305**, 654 (2004).
- [6] Z. Budrovic, H. Van Swygenhoven, P. M. Derlet, S. Van Petegem, and B. Schmitt, *Science* **304**, 273 (2004).
- [7] W. D. Nix, *Metall. Trans. A* **20A**, 2217 (1989).
- [8] H. J. Fecht, *Phys. Rev. Lett.* **65**, 610 (1990).
- [9] M. Wagner, *Phys. Rev. B* **45**, 635 (1992).
- [10] J. Harada, and K. Ohshima, *Surf. Sci.* **106**, 51 (1981).
- [11] J. A. Eastman, M. R. Fitzsimmons, and L. J. Thompson, *Phil. Mag. B* **66**, 667 (1992).
- [12] J. A. Eastman, M. R. Fitzsimmons, L. J. Thompson, A. C. Lawson, and R. A. Robinson, *Nanostruct. Mater.* **1**, 465 (1992).
- [13] T. Turi, and U. Erb, *Mater. Sci. Eng. A* **204**, 34 (1995).
- [14] B. B. Panigrahi, V. V. Dabhade, and M. M. Godkhindi, *Mater. Lett.* **59**, 2539 (2005).
- [15] K. Lu, and M. L. Sui, *Acta Metall. Mater.* **43**, 3325 (1995).
- [16] Y. H. Zhao, and K. Lu, *Phys. Rev. B* **56**, 14330 (1997).
- [17] J. G. Lee, and H. Mori, *Eur. Phys. J. D* **34**, 227 (2005).
- [18] W. Fang, and C. Y. Lo, *Sensor Actuat. A-Phys* **84**, 310 (2000).
- [19] K. Zhang, I. V. Alexandrov, R. Z. Valiev, and K. Lu, *J. Appl. Phys.* **84**, 1924 (1998).
- [20] Y. Zoo, D. Adams, J. W. Mayer, and T. L. Alford, *Thin Solid Films* **513**, 170 (2006).
- [21] H. Zhang, and B. S. Mitchell, *Mater. Sci. Eng. A* **270**, 237 (1999).
- [22] M. Wohlschlägel, U. Welzel, G. Maier, and E. J. Mittemeijer, *J. Appl. Cryst.* **39**, 194 (2006).
- [23] M. Wohlschlägel, T. U. Schüllli, B. Lantz and U. Welzel, *J. Appl. Cryst.* **41**, 124 (2008).

- 
- [24] M. Wohlschlägel, T. U. Schüllli, G. Maier, U. Welzel and E. J. Mittemeijer, *Z. Kristallogr. Suppl.* **26**, 147 (2007).
- [25] U. Welzel, J. Ligot, P. Lamparter, A. C. Vermeulen, and E. J. Mittemeijer, *J. Appl. Cryst.* **38**, 1 (2005).
- [26] A. Latapie and D. Farkas, *Scripta Mater.* **48**, 611 (2003).
- [27] T. D. Shen, C. C. Koch, T. Y. Tsui and G. M. Pharr, *J. Mater. Res.* **10**, 2893 (1995).
- [28] Y. S. Touloukian, *Thermal Expansion: Metallic Elements and Alloys* (IFI/Plenum, New York, 1975).
- [29] R. Delhez, Th. H. de Keijser, and E. J. Mittemeijer, *Fresen. Z. Anal. Chem.* **312**, 1 (1982).
- [30] Th. H. de Keijser, J. I. Langford, E. J. Mittemeijer, and A. B. P. Vogels, *J. Appl. Cryst.* **15**, 308 (1982).
- [31] E. J. Mittemeijer and P. Scardi (Eds.), *Diffraction Analysis of the Microstructure of Materials* (Springer, Berlin; Heidelberg, 2004).
- [32] M. F. Doerner, and W. D. Nix, *Crit. Rev. Solid State* **14**, 225 (1988).
- [33] P. Chaudhari, *Vac. Sci. Technol.* **9**, 520 (1972).
- [34] M. Kiguchi, T. Yokoyama, D. Matsumura, H. Kondoh, O. Endo, and T. Ohta, *Phys. Rev. B* **61**, 14020 (2000).

## Chapter 4

# Interdiffusion and stress development in Cu-Pd thin film diffusion couples

*Y. Kuru, M. Wohlschlägel, U. Welzel and E.J. Mittemeijer*

### Abstract

Thin film Cu-Pd diffusion couples (individual sublayer thicknesses: 50 nm) were prepared by DC-magnetron sputtering on silicon substrates coated with amorphous diffusion/reaction barriers ( $\text{Si}_3\text{N}_4$  on top of  $\text{SiO}_2$ ). The microstructural variations, phase formation and stress evolution during diffusion annealing were investigated employing Auger-electron spectroscopy (AES) in combination with sputter depth profiling, transmission electron microscopy (TEM) and *in-situ* X-ray diffraction (XRD). Upon annealing at relatively low temperatures (185 °C) for durations up to 17 hours, considerable diffusional intermixing occurs. Interdiffusion is accompanied by the formation of a compound phase (ordered  $\text{Cu}_3\text{Pd}$  ( $\alpha'$ )). The stress changes in the bilayer system during heating and isothermal annealing were investigated employing *in-situ* X-ray diffraction stress measurements and were compared to corresponding results obtained for single layers of the components in the Cu-Pd bilayers system, produced under conditions identical to those employed for the sublayers of the diffusion couple. The specific residual stresses that emerge due to diffusion (and reactions) between the (sub)layers in the bilayer could then be identified by comparing the stress evolutions upon annealing of the single layers with those recorded for the sublayers of the bilayer.

## 4.1 Introduction

Thin films can exhibit very high levels of residual stress. One usually distinguishes: (i) intrinsic, growth stresses [1,2] (ii) extrinsic, thermal stresses (arising from a difference between the coefficients of thermal expansion (CTE) of film and substrate; see, for example, [3,4]) and (iii) stress development due to thermally activated processes as annihilation of defects, grain growth, interdiffusion and phase transformations [5,6].

Interdiffusion can be a source of stress generation in a bilayer diffusion couple if the partial molar volumes of the components of the specimen are different and/or if a net vacancy flux occurs due to a difference of the intrinsic diffusion coefficients of the diffusing species which is not counterbalanced by vacancy generation and annihilation processes (cf. the Kirkendall effect [7]) (see, for example, [8,9]). It has been speculated that, in turn, the (diffusion-induced and thereby changing) stress state influences the diffusion process [10]. The effect of an imposed state of stress on diffusion is well known for the case of hydrostatic stress, which modifies the diffusivity via the so-called activation volume [7]. The case of a non-hydrostatic nature of the stress state (e.g. a biaxial state of stress in thin films) has received much less attention: The pioneering theoretical work in this field is due to Larche and Cahn [11]; systematic experimental investigations for thin film systems are rare, in spite of the scientific and technological importance. As an example, Welzel *et al.* investigated the stress evolution accompanying interdiffusion for sputtered Nb/W layers in the temperature range 400 °C-700 °C employing ex-situ X-ray diffraction (XRD) stress measurements [12,13]. Balandina and Ostrovsky studied grain boundary diffusion in thin metallic films and attempted correlating the measured grain boundary diffusion coefficient with stresses in the layers [14,15]. However, questionable assumptions were adopted: (i) The flux was assumed to be proportional to the chemical potential gradient although thin films are in a biaxial state of nonhydrostatic stress and the diffusion potential gradient should have been employed as driving force for the diffusion [11]. (ii) The stresses in the thin films were assumed to be due to only the thermal stresses produced during cooling from deposition temperature to room temperature as consequence of differences between CTEs of the films and the substrates, neglecting intrinsic stresses as well as plastic strain accommodation. Moreover, stress change by the diffusion (process) itself (see results of the present work in Section 4.3.4) was ignored as well.

*In-situ* X-ray diffraction (XRD) is a versatile tool to probe stress changes in a diffusion couple since the stresses in each phase can be determined [16], in contrast with the in-situ



wafer curvature method which can only measure the average stresses of the (bi)layer system [1,2,6]. In addition, microstructural information comprising the crystallographic texture, the density of crystal defects, such as dislocations, and the crystal size, can be acquired from the collected XRD data. It should be recognized that the interpretation of XRD data recorded at non-ambient temperatures is much more demanding than at ambient temperature, since (i) the temperature dependences of physical properties of films and substrate, as the coefficient of thermal expansion, should be known and a dedicated calibration of the specimen temperature has to be performed [17], and (ii) in particular, besides diffusional intermixing, processes as grain growth, strain relaxation by plastic accommodation and the formation of new phases can occur at non-ambient temperatures. Thereby a quantitative interpretation of the stress evolution, as determined by in-situ XRD, in terms of (only) diffusion is not straightforward [18].

One possible way to sort out stress changes due to processes other than interdiffusion is to perform also experiments with single layers of the components (sublayers) in the bilayer system investigated and produced under conditions identical to those employed for the sublayers of the diffusion couple. Residual stresses that emerge due to diffusion (and reactions) between the sublayers in the bilayer can then be identified by comparing the stress evolutions upon annealing of the single layers with those recorded for the bilayer.

In the present work, interdiffusion, phase formation and stress evolution in thin Cu-Pd bilayer (individual sublayer thicknesses: 50 nm) diffusion couples have been investigated employing Auger-electron spectroscopy in combination with sputter-depth profiling, transmission electron microscopy and in-situ X-ray diffraction measurements. It has been found that upon annealing at relatively low temperatures (185 °C) for durations up to 17 hours considerable diffusional intermixing, accompanied by the formation of a compound phase and considerable stress changes, occurs. The possible sources of the observed stress (changes) in the Cu-Pd bilayer during diffusion annealing have been discussed, with reference to the stresses observed for the single layers subjected to the same heat treatment as the bilayer.

## 4.2 Experimental

### 4.2.1 Specimen production

Cu and Pd thin films were deposited at room temperature (25 °C) onto Si (100) wafers covered with thin amorphous SiO<sub>2</sub> and Si<sub>3</sub>N<sub>4</sub> (on top) diffusion-barrier layers (each 50 nm thick), by DC magnetron sputtering under ultra high vacuum conditions (base pressure about  $1 \times 10^{-10}$  mbar). Each of the thin films had a thickness of 50 nm. Prior to the deposition, the substrates were sputter-cleaned for about 1 minute with argon ions of kinetic energy 100 eV. During the film deposition, the substrate holder was rotating and the chamber pressure was maintained at  $2 \times 10^{-4}$  mbar employing Ar as sputter gas. The Cu sputter source was operated at 200 W; the Pd sputter source was operated at 100 W. For preparation of the diffusion couple, Cu was deposited as the bottom layer of the couple onto a similar substrate as the single layers; the Pd layer was then deposited as the top layer since Pd is a more noble metal and less prone to oxidation than Cu.

### 4.2.2 Transmission electron microscopy

The microstructure of the as-deposited Cu-Pd bilayer was investigated in a Philips CM 200 transmission electron microscope (TEM) with a 200 kV electron beam. For cross-sectional sample preparation of as-deposited and annealed specimens, two pieces were cut from the bilayer/substrate specimen and sandwiched (bilayers of both pieces facing each other) with epoxy glue. After mechanical thinning by grinding, the thin slice of material was embedded into a specially designed cylindrical polycrystalline Al<sub>2</sub>O<sub>3</sub> tube of 3 mm diameter as a holder for the cross-sectional sample. Then the tube was cut into slices. The slices underwent mechanical grinding, dimpling from both sides and finally ion thinning (Ar<sup>+</sup> ions with 3.5 keV energy and 1 mA ion current in a BAL-TEC RES 010 apparatus with liquid nitrogen cooling) for several hours to achieve electron transparency. Details of the cross-sectional specimen preparation can be found in Ref. [19].

### 4.2.3 Concentration-depth profiling

Concentration-depth profiles were obtained by using ion sputtering in combination with Auger Electron Spectroscopy (AES) in a JEOL JAMP 7830F field emission Auger microprobe. The energies of the argon ions and the primary electron beam were 1 keV and 10 keV, respectively. Auger lines of Cu (LMM, 920 eV) and Pd (MNN, 330 eV) were measured for the determination of the Cu and Pd concentrations. The sputter rates for the pure elements (Cu and Pd) were evaluated by total removal by sputtering of the pure Cu and pure

Pd layers in the unannealed (as-deposited) specimens. The ratio of their sputter rates was determined as 0.96. Sputter time can be converted into sputter depth if the sputter rate is known. However, the sputter rate can change with changing composition in a binary system when interdiffusion takes place. In order to evaluate the sputter rate of the Cu-Pd binary system after diffusion annealing a simple kinetic sputter model was applied [20]: The atomic concentrations of Cu and Pd,  $c_{\text{Cu}}$  and  $c_{\text{Pd}}$ , respectively, were calculated using the following relationships:

$$c_{\text{Cu}} = \frac{\frac{I_{\text{Cu}}}{S_{\text{Cu}}}}{\frac{I_{\text{Cu}}}{S_{\text{Cu}}} + \frac{I_{\text{Pd}}}{S_{\text{Pd}}}} \quad (1)$$

$$c_{\text{Pd}} = \frac{\frac{I_{\text{Pd}}}{S_{\text{Pd}}}}{\frac{I_{\text{Cu}}}{S_{\text{Cu}}} + \frac{I_{\text{Pd}}}{S_{\text{Pd}}}} \quad (2)$$

where  $S_{\text{Cu}}$  and  $S_{\text{Pd}}$  are the relative Auger yields of Cu and Pd respectively with respect to pure Ag (here: 0.574 and 0.923, respectively).  $I_{\text{Cu}}$  and  $I_{\text{Pd}}$  are the Auger peak-to-peak heights (APPH) of the Auger peaks corresponding to Cu and Pd, respectively, in the differentiated spectrum.

#### 4.2.4 X-ray diffraction

X-ray diffraction measurements were performed employing a Bruker D8 Discover diffractometer equipped with an Eulerian cradle. Cu-K $\alpha$  radiation, emerging from the point focus of a rotating-anode X-ray source (Bruker TXS) operating at 50 kV and 20 mA, was converted into a quasi-parallel beam by a collimating X-ray mirror (Xenocs) [21,22]. The diffracted beam passed a parallel plate collimator (acceptance angle 0.23°) before being detected by a scintillation counter. For in-situ, temperature dependent, experiments a heating/cooling chamber DCS350 (Anton Paar) was mounted on the Eulerian cradle (see also [17]). With this equipment, it is possible to perform in-situ experiments within a temperature range between -100 °C and 350 °C and at pressures of the order of 10<sup>-3</sup> mbar. Calibration of the heating/cooling chamber was performed by a resistance thermometry method (for details see Ref. [17]).

The specimens (both the single Cu and Pd layers and the Cu-Pd couples) were first cooled from room temperature to -100 °C, then heated back to room temperature, next heated

from room temperature to 185 °C, subsequently isothermally annealed at this temperature for 16 hours and 40 minutes, and finally cooled back to room temperature. The increments in temperature during heating and cooling were taken as 25 °C, except for the last step (150 °C → 185 °C). The annealing temperature was chosen relatively low (185 °C) to facilitate diffraction measurements in time periods of 20-40 minutes during which the specimen did not undergo significant microstructural change. The  $2\theta$  ranges employed to record the {111} reflections were 42°-45° for the single Cu layer, 37.5°-42.5° for the single Pd layer and 38.5°-44.5° for the Cu-Pd bilayer. For stress analysis at every temperature step, measurements of these diffraction-angle ranges were performed at two specimen tilt angles,  $\psi=0^\circ$  and  $\psi=70.54^\circ$ , employing the side-inclination method [16]. This resulted in durations of about 22 minutes and 40 minutes for one stress measurement for a single layer and a bilayer, respectively. A waiting time of 5 minutes was adopted upon arriving at the temperature of each temperature step in order to guarantee temperature homogenization.

The software ‘ProFit’ (Panalytical) was used to determine peak maximum positions, full widths at half maximum (FWHM), integral breadths and integrated intensities by fitting Pearson VII functions to measured diffraction lines [23].

For the analysis of mechanical stress the interplanar spacing  $d_\psi^{hkl}$  at each tilt angle,  $\psi$  was calculated from the corresponding position of the  $hkl$  diffraction-line maximum, determined by peak fitting (see above) using Bragg’s law. In the present work, the 111 reflections were used for stress analysis for both the Cu(-rich) phase and the Pd(-rich) phase. Due to the in-plane rotational symmetry of the biaxial state of stress in the Cu and Pd sublayers (measurements at rotation angles  $\varphi = 0^\circ$  and  $\varphi = 90^\circ$  with respect to the specimen normal yielded the same stress values) and the occurrence of a pronounced {111}-fibre texture (cf. Section 4.3.2), the fibre-texture crystallite group method (CGM) was employed. In this limit, single crystal elastic compliances (values were taken from Ref. [24]) can be used in the diffraction stress evaluation instead of the diffraction stress factors (for details, see [16,25]; for limitations in the application of the CGM in the case of fibre texture, see Ref. [26]). For the case of CGM, the stress parallel to the surface,  $\sigma$ , and the strain-free direction,  $\sin^2 \psi^*$ , can be obtained employing Eqs. (3) and (4), respectively, where  $s_{11}$ ,  $s_{12}$  and  $s_{44}$  are the single-crystal compliances and  $d_0^{hkl}$  is the strain-free lattice spacing of the { $hkl$ } planes:

$$d_\psi^{hkl} = 2d_0^{hkl} \sigma \left( s_{12} + \frac{s_{11} - s_{12} - s_{44}/2}{3} \right) + d_0^{hkl} + \frac{1}{2} d_0^{hkl} \sigma s_{44} \sin^2 \psi \quad (3)$$

$$\sin^2 \psi^* = \left( -2s_{12} - \frac{2}{3}(s_{11} - s_{12} - s_{44}/2) \right) / \left( \frac{1}{2}s_{44} \right) \quad (4)$$

The measured diffraction profile  $h(x)$  can be conceived as the convolution of an only structurally broadened profile  $f(x)$  with the instrumentally broadened profile  $g(x)$ :  $h(x) = f(x) \otimes g(x)$ . The structural line broadening can originate from crystalline imperfections, as small crystallite size and the microstrain due to dislocations, misfitting precipitates etc. The instrumental broadening incorporates all instrumental aberrations as slit widths, etc. Both theory and experiment support that in many cases, the structurally broadened and the instrumentally broadened profiles can all well be approximated by Voigt functions (a Voigt function is the convolution of a Cauchy (Lorentz) function and a Gauss function). In this case, the integral breadths of the Gauss- and Cauchy components of the structurally broadened profiles,  $\beta_{f,g}$  and  $\beta_{f,c}$ , respectively, can be obtained from the integral breadths ( $\beta_h$ ) and the Voigt parameters (i.e., the ratio of the FWHM to the integral breadth) of the measured profiles ( $h$ ) employing the so-called Voigt-method [27-30]. To this end, the integral breadths ( $\beta_g$ ) and the Voigt parameters of the instrumentally broadened profiles ( $g$ ) have to be known as well. In order to determine the instrumentally broadened profile of the diffractometer as function of diffraction angle  $2\theta$ , 13  $hkl$  reflections of a LaB<sub>6</sub> (NIST SRM660a) standard powder sample were measured. The integral breadths and the Voigt parameters at the diffraction angles of the Cu and Pd 111 reflections were then obtained by interpolation.

Assuming that the Cauchy component of the structurally broadened profile is due to the small crystallite size and that the Gauss component of the structurally broadened profile is due to microstrains, the crystallite size  $D$  and the microstrain  $e$  can be obtained from [27,28]:

$$\beta_{f,c} = \frac{K\lambda}{D \cos \theta_0} \quad (5)$$

$$\beta_{f,g} = 4e \tan \theta_0 \quad (6)$$

where  $K$  is the Scherrer constant (taken equal to 1, which is compatible with columnar grains oriented perpendicular to the surface of constant height),  $\lambda$  is the wavelength and  $\theta_0$  is the position of the diffraction-line maximum. The value of  $e$  in Eq.(6) is a measure for the microstrain (variation) in the specimen. For the case of a Gaussian strain distribution is it possible to calculate the local r.m.s. strain  $\langle \varepsilon_0^2 \rangle^{1/2}$  from  $e$ :  $\langle \varepsilon_0^2 \rangle^{1/2} = (2/\pi)^{1/2} e$  [27].

This single-line method of diffraction-line broadening analysis is very useful to acquire a general understanding of origins of line broadening and to obtain estimates for crystallite size and microstrain and, in particular, to observe the evolution of their values in-situ as functions of temperature and/or time. More sophisticated and more detailed methods for the analysis of diffraction-line broadening exist (see, for example, Ref. [31]), but such analyses require much more measurement time (e.g. a second, weak order of the reflection has to be measured) which damages unacceptably the time resolution in the in-situ investigation performed here.

## 4.3 Results

### 4.3.1 Diffusional intermixing

Concentration-depth profiles for the bilayer in the as-deposited state and after annealing at 185 °C for 7 h and 17 h are shown in Fig. 4.1. The sputter-depth profiles of the as-deposited specimens do not show a truly sharp interface at the location of the Cu/Pd interface due to the roughness of the interface and the smearing of the 'true' concentration-depth profile due to instrumental effects associated with sputter-depth profiling (see, for example, [32,33]). The occurrence of appreciable diffusional intermixing in the unannealed diffusion couple is unlikely as all depositions have been performed at temperatures where diffusion can be neglected ( $T < 40^\circ\text{C}$ , cf. Section 4.2.1). As follows from Fig. 4.1, annealing at 185 °C leads to considerable diffusional intermixing: In addition to a change of the slope at the position of the initial interface, the sputter-depth profiles for the annealed samples show the emergence of a plateau region of considerable Pd concentration in the initially pure Cu sublayer, the height of which increases with annealing time. This is a result of Pd diffusion through Cu grain boundaries accompanied with sideways Pd diffusion from the Cu grain boundaries into the Cu grains. Further, a significant Cu concentration occurs at the surface of the bilayer specimen, whereas the Cu concentration in the plateau region of the Pd layer remains small. Thus, sideways Cu diffusion from the Pd grain boundaries into the Pd grains is very limited. Values determined for volume interdiffusion coefficients and grain-boundary diffusion coefficients have been determined from both the near interface and the plateau regions [6].

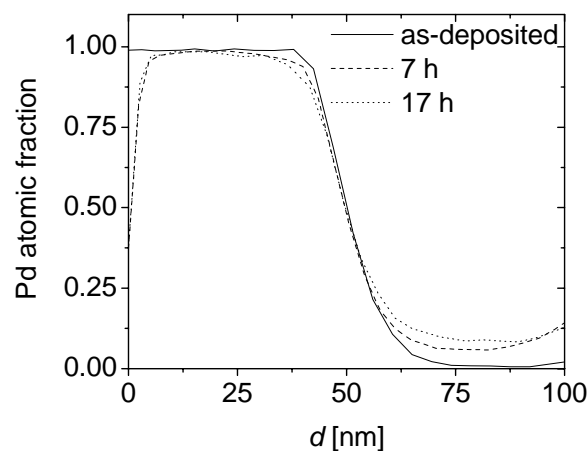


**Fig. 4.1:** Sputter-depth profiles (AES) of the specimen before annealing and after annealing at 185 °C for 7 h and 17 h.

### 4.3.2 Microstructure

A cross-sectional bright field TEM image of the as-deposited Cu-Pd bilayer is shown in Fig. 4.2. The interface between the Cu and Pd layers can be discerned. Although some equiaxed grains exist, most of the grains in both layers have a columnar morphology; the in-plane, lateral grain sizes of the layers are in the range between 30 to 40 nm.

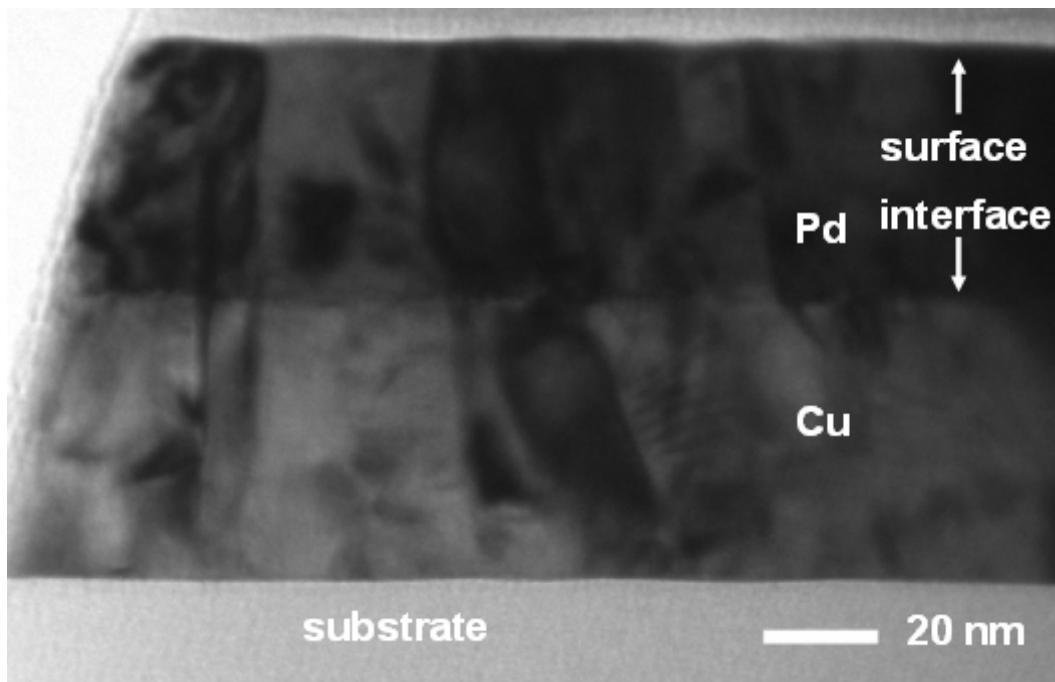


**Fig. 4.2:** Cross-sectional TEM micrograph (bright field) of the as-deposited Cu-Pd bilayer.

The  $\{111\}$  pole figure sections (normalized (with respect to the maximum at  $\psi=0^\circ$ ) integrated intensity of the 111 reflections plotted versus  $\psi$ ) of both sublayers of the bilayer before and after annealing are shown in Fig. 4.3. The Cu and Pd sublayers have relatively strong  $\{111\}$  fibre textures in the as-deposited state and after annealing. The rotational symmetry of the texture with respect to the specimen normal was confirmed by measurements at different angles of rotation with respect to the specimen normal,  $\varphi$ . The intensity maxima at  $\psi=0^\circ$  and  $\psi=70.54^\circ$  correspond to the ideal orientations of the  $\{111\}$  fibre texture crystallite group. These results justify employing the CGM for the residual stress analysis of as-deposited and heat treated samples (see Section 4.2.4). The small hump at about  $\psi=22^\circ$  in the pole figure section of the annealed Cu sublayer originates from multiple twinning (annealing twins); cf. Ref. [3].



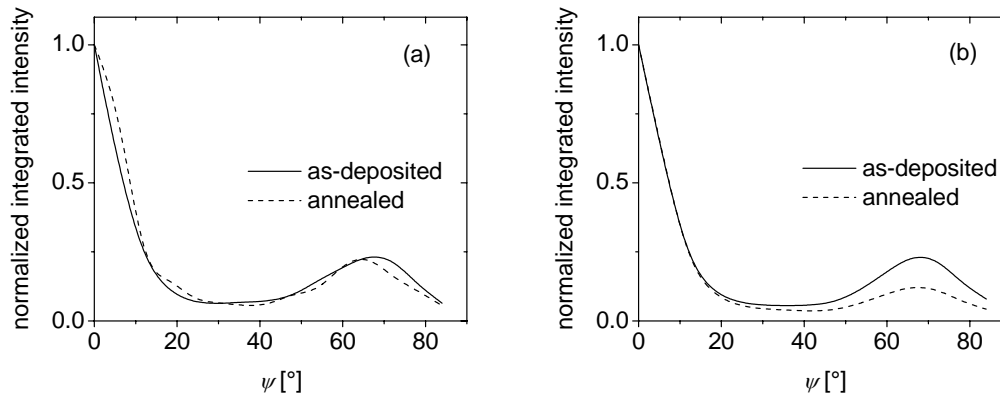


**Fig. 4.3:** Pole figure sections of the (a) Cu layer and (b) Pd layer of the bilayer before and after annealing, using the 111 Cu and 111 Pd reflections, respectively.

### 4.3.3 Phase formation

The diffraction patterns corresponding to the diffraction-angle ranges of the Cu and Pd 111 reflections of diffusion couples in the as-deposited state and after annealing at 185 °C for different times are shown in Fig. 4.4. The separate 111 reflections of pure Cu and pure Pd are clearly observed in the XRD pattern for the as-deposited state. If complete solid solubility prevails in the Cu-Pd system, it is expected that the corresponding 111 reflections of Cu and Pd broaden upon diffusion annealing because of a developing continuous composition variation perpendicular to the original interface of the couple, and finally merge into the single reflection corresponding to the homogenized state. However, the experiment reveals that upon annealing a shoulder develops at the low-angle side of the original Cu 111 reflection. Such additional reflections also appear at the low-angle side of the Cu 200, 311 and 222 reflections. This suggests that phase formation has occurred upon diffusion annealing.

The phase formed has been identified as follows: The strain-free lattice constant of the new phase has been determined from the position of the diffraction line developing at the low-angle side of the original Cu 111 reflection measured as a function of  $\sin^2 \psi$  under the following hypotheses: (i) the new phase has cubic symmetry and the reflection considered is the 111 reflection of the new phase; (ii) the strain-free direction  $\psi_0$  of the new phase is identical to the strain-free direction of Cu; (iii) the stress state for the new phase is also planar, rotationally symmetric. The observed strain-free lattice constant for the new phase at room temperature (25 °C) has been determined as  $a=0.3676$  nm. Then, adopting a linear dependence on composition for the lattice parameter of the disordered Cu-Pd solid solution ('Vegard's law'; this assumption is justified for the system Cu-Pd; cf. Ref. [34,35]) between the strain-free lattice constants obtained for the Cu and Pd layers in the as-deposited

condition, this observed value for the lattice parameter of the new phase was found to fall within the range of values of lattice parameters reported for the ordered phase  $\alpha'$ -Cu<sub>3</sub>Pd, existing between about 8 and 22 at. % Pd, exhibiting ordering according to the prototype structure Cu<sub>3</sub>Au (Strukturbericht designation L1<sub>2</sub>; space group  $Pm\bar{3}m$ ; cf. Ref. [34]). Hence, the newly formed phase likely is  $\alpha'$ -Cu<sub>3</sub>Pd. Moreover, the occurrence and the observed positions of further reflections are compatible with the formation of the phase  $\alpha'$ -Cu<sub>3</sub>Pd. The superstructure reflections (100, 110,...) were not observed, which is plausible recognizing that the values of the atomic scattering factors of Pd and Cu do not differ much: The superstructure reflections have an intensity less than about 5 % of the intensity of the 111 reflection.

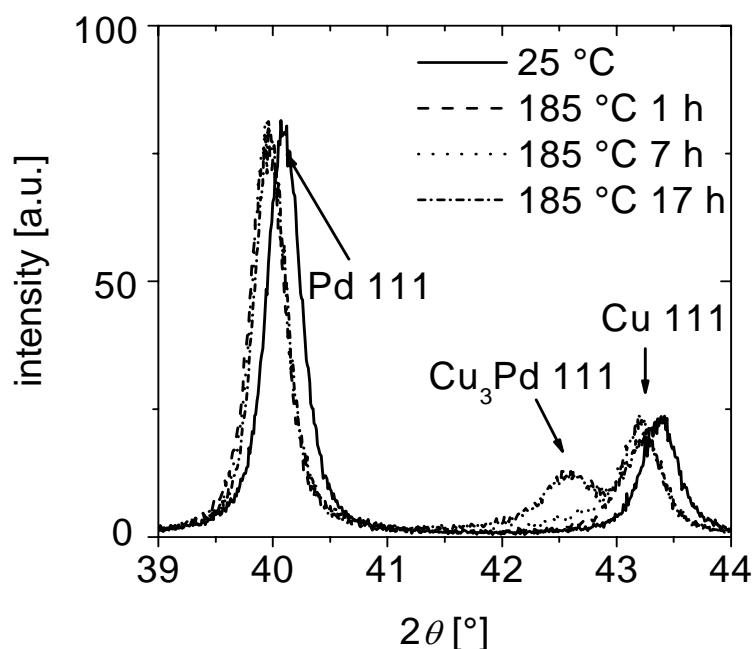


**Fig. 4.4:** Diffraction pattern of the Cu-Pd bilayer at 25 °C and during annealing at 185 °C in the diffraction-angle range pertaining to the 111 reflections of Cu and Pd. For all measurements,  $\psi=0^\circ$ , i.e. the diffraction vector is oriented perpendicular to the film surface.

It has to be noted that the presence of a tetragonal  $\alpha''$ -Cu<sub>3</sub>Pd phase (space group  $P4mm$ ; cf. Ref. [34]) phase cannot be definitively excluded as a tetragonal splitting for the 200 and 311 reflections may not be observable due to the intrinsic broadening of the reflections and the low tetragonality ( $c/a$  ratio  $> 0.95$ ) of the tetragonal  $\alpha''$ -Cu<sub>3</sub>Pd phase.

The square of the integrated intensity of the  $\alpha'$ -Cu<sub>3</sub>Pd 111 peak (measured at  $\psi=0^\circ$ ) has been plotted versus annealing time at  $T=185^\circ\text{C}$  in Fig. 4.5. Taking the integrated intensity of the Cu<sub>3</sub>Pd 111 reflection as a measure for the volume fraction of Cu<sub>3</sub>Pd (it was found that the texture of Cu<sub>3</sub>Pd is also of  $\{111\}$  fibre-texture type and did not change significantly

during annealing), it follows that the amount of  $\text{Cu}_3\text{Pd}$  formed is proportional to  $t^{1/2}$ , implying a parabolic growth law. Thus, the results suggest that the growth of the  $\text{Cu}_3\text{Pd}$  phase is diffusion-controlled and that a significant incubation time occurs.

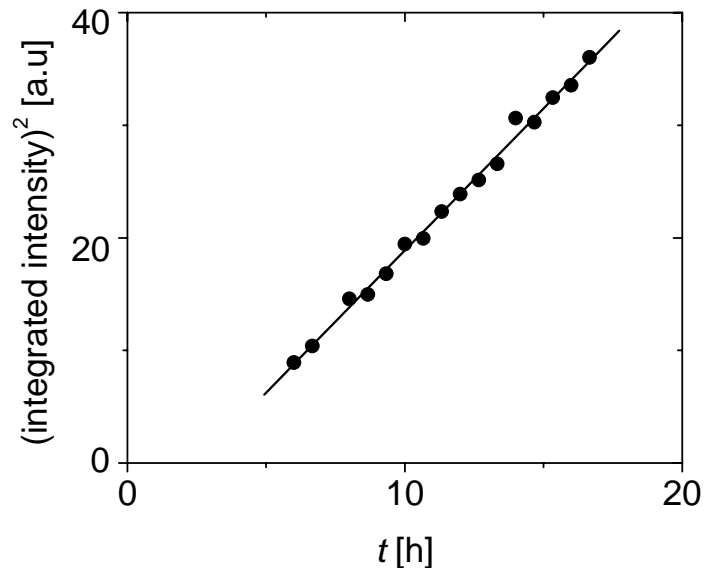


**Fig. 4.5:** Square of the integrated intensity of the  $\text{Cu}_3\text{Pd}$  111 peak versus time,  $t$  ( $T=185\text{ }^\circ\text{C}$ ).

#### 4.3.4 Stress evolution

Single Cu and Pd layers and Cu-Pd bilayers were cooled from room temperature to  $-100\text{ }^\circ\text{C}$  in order to trace the thermoelastic behaviour in the absence of thermally activated processes which would change the microstructure. The observed residual stresses vary linearly and reversibly with temperature (below room temperature) for all layers. The thermoelastic slopes,  $\Xi$  ( $\Xi = \Delta\sigma/\Delta T$ ), of the Cu and Pd layers in the bilayer are found to be equal to the thermoelastic slopes of their single layer counterparts within experimental accuracy (cf. Table 4.1). The room temperature stress levels of the as-deposited single layers and their counterparts in the as-deposited bilayer specimens are different (see, at  $25\text{ }^\circ\text{C}$ , Figs. 4.6(a) and 4.6(c), and Figs. 4.6(b) and 4.6(d)). These differences can be due to slight variations in the deposition conditions for the single and bilayer specimens. The larger stress difference observed for the Pd layers may be understood recognizing that the Pd layer in the couple grows on a Cu layer, whereas the Pd single layer grows on the bare substrate: The growth stress is very sensitive to even slight changes in the substrate surface condition (cf. Ref. [3]).

After cooling to  $-100\text{ }^\circ\text{C}$ , all layers were heated up (in steps, cf. Section 4.2.4) to  $185\text{ }^\circ\text{C}$ . The thus induced variations in residual stress of the Cu and Pd layers (both as single

layers and as sublayers of the bilayer) are shown in Fig. 4.6, at temperatures at and above room temperature, together with the straight-line extrapolations of the stress evolution at temperatures well below room temperature to temperatures above room temperature, which extrapolations represent the thermoelastic behaviour in the absence of thermally activated processes [18].

**Table 4.1.** Calculated thermoelastic slopes of both layers for the cases of polycrystalline and perfect {111} fiber textured films using the corresponding single-crystal elastic constants, Young's modulus and Poisson's ratio in Ref. [24].

<b>Thermoelastic slopes <math>\Xi</math> calculated for the Cu and Pd layers</b>			
<b>Cu</b>		<b>Pd</b>	
Polycrystalline [MPa/°C]	Perfect {111} Fiber Textured [MPa/°C]	Polycrystalline [MPa/°C]	Perfect {111} Fiber Textured [MPa/°C]
-2.39	-3.20	-1.70	-2.45
<b>Thermoelastic slopes measured for Cu and Pd layers</b>			
Single Cu layer [MPa/°C]	Cu layer of the bilayer [MPa/°C]	Single Pd layer [MPa/°C]	Pd layer of the bilayer [MPa/°C]
-3.32±0.06	-3.45±0.23	-2.55±0.1	-2.53±0.09

For both the single Cu layer and the Cu sublayer of the diffusion couple the variation of the stress with temperature is nonlinear with respect to the purely thermoelastic behaviour: tensile stress contributions develop in both Cu layers. The amount of tensile stress created, with respect to the purely thermoelastic behaviour, in the Cu layer of the bilayer is larger (about 130 MPa at 185 °C) than the tensile stress contribution generated in the single Cu layer.

Whereas at 185 °C a tensile stress contribution of about 220 MPa has been generated, with respect to the purely thermoelastic behaviour, in the single Pd layer, the stress in the Pd sublayer of the diffusion couple follows more or less the thermoelastic extrapolation.

During the anneal at 185 °C, the stresses in the single Cu and the single Pd layers do not show a considerable variation with time (cf. Fig. 4.7). The modest stress change of compressive nature in the Cu single layer is likely caused by oxidation (see Fig. 4.7). In contrast, both sublayers of the diffusion couple reveal a considerable tensile stress contribution developing during the anneal at 185 °C according to a parabolic time law (cf. Fig. 4.8).

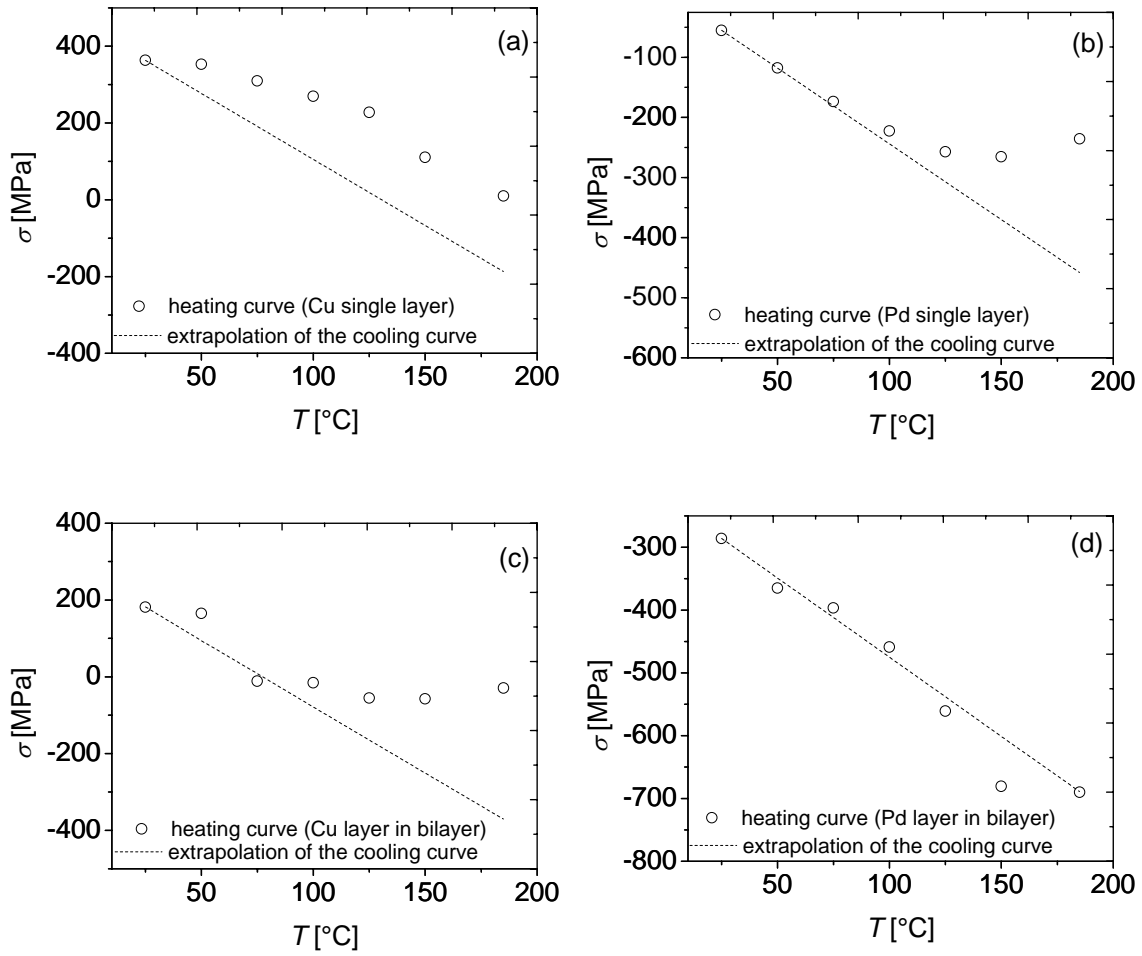


**Fig. 4.6:** Stress,  $\sigma$ , versus temperature,  $T$ , plots for (a) Cu and (b) Pd single layers and (c) Cu and (d) Pd sublayers of the bilayer. Straight line extrapolations to the elevated temperatures are also shown.

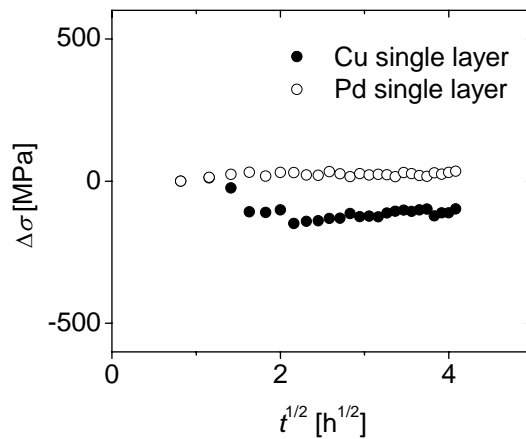


**Fig. 4.7:** Variation in stress,  $\Delta\sigma$ , versus square root of time,  $t^{1/2}$ , graphs for Cu and Pd single layers ( $T=185$  °C).

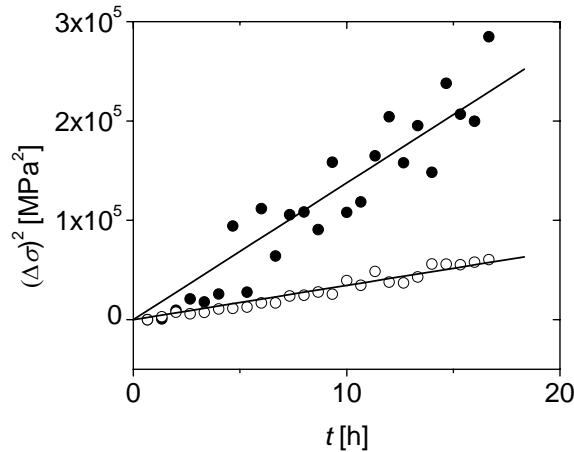


**Fig. 4.8:** Square of the variation in stress,  $((\Delta\sigma)^2)$ , versus time,  $t$ , graphs for Cu and Pd sublayers of the bilayer.

### **4.3.5 Line broadening analysis of the single layers and sublayers of the couple**

#### **Heating to 185 °C**

The crystallite size,  $D$ , and microstrain,  $e$ , values obtained from the line broadening analysis applied to the 111 reflections (cf. Section 4.2.4) during heating for both the single layers and the sublayers of the diffusion couple from room temperature to 185 °C have been gathered in Fig. 4.9. For both the Cu layers and the Pd layers, the crystallites sizes, microstrains and their temperature dependences are similar for the single layers and the corresponding sublayers in the diffusion couple, except for the microstrain in the Pd layers: The single Pd layer exhibits a larger microstrain that decreases upon increasing the temperature, whereas a constant (and lower) microstrain is found for the Pd sublayer of the diffusion couple. The microstrain attained at 185 °C in the single Pd layer is about equal to the (constant, temperature-independent) microstrain of the Pd sublayer in the diffusion couple. Upon heating the specimens to 185 °C, a slight increase of the crystallite size is observed which indicates the occurrence of moderate grain growth.

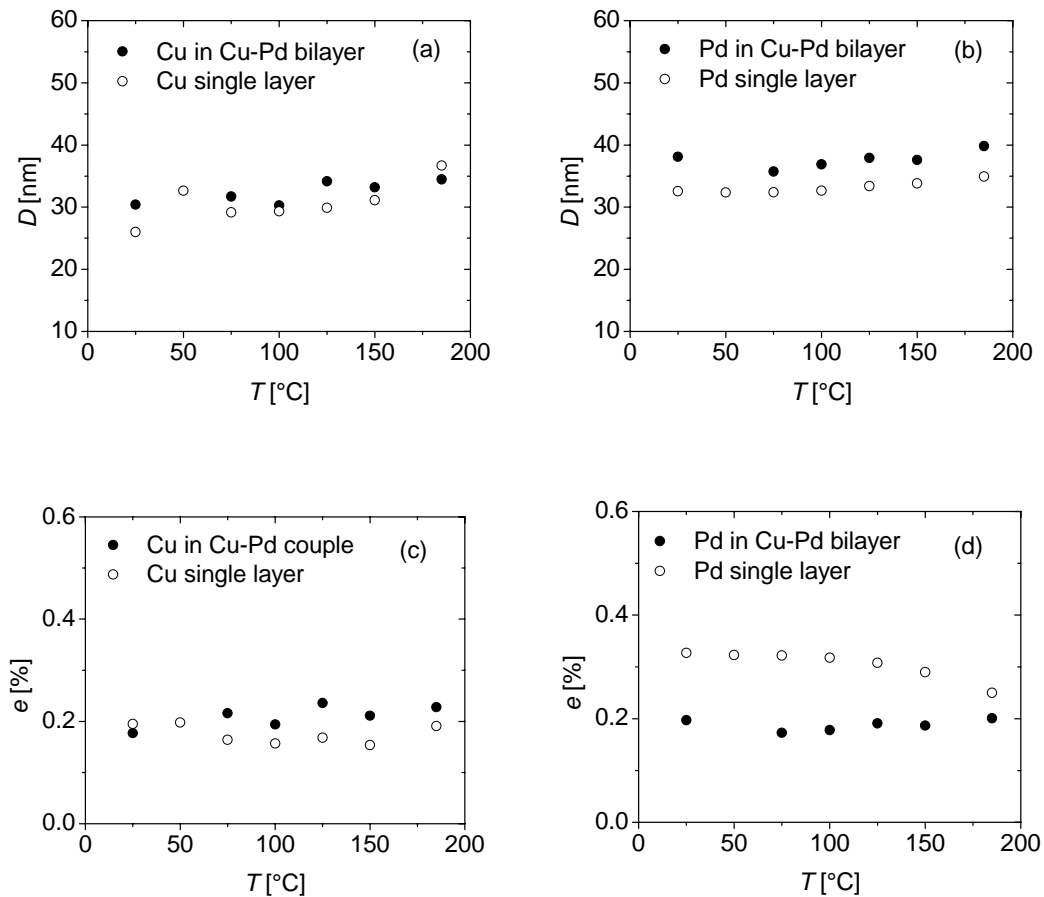


**Fig. 4.9:** Evolution of crystallite size,  $D$ , for (a) Cu layer of the bilayer and single Cu layer and (b) Pd layer of the bilayer and single Pd layer and microstrain,  $e$ , for (c) Cu layer of the bilayer and single Cu layer and (d) Pd layer of the bilayer and single Pd layer with temperature,  $T$ . For all measurements,  $\psi=0^\circ$ , i.e. the diffraction vector is oriented perpendicular to the film surface.

### Annealing at 185 °C

The crystallite size,  $D$ , and microstrain,  $e$ , values obtained from the line broadening analysis applied to the 111 reflection during isothermal annealing for both the single layers and the Pd sublayer of the diffusion couple have been gathered in Fig. 4.10. A reliable analysis of the diffraction-line broadening for the Cu sublayer of the diffusion couple was obstructed by the emergence of the  $\text{Cu}_3\text{Pd}$  reflection (see Fig. 4.4). For both the Cu and Pd single layers, the crystallites sizes and microstrains remain constant during isothermal annealing. For the Pd sublayer of the diffusion couple, a moderate increase of the crystallite size,  $D$ , from about 40 nm to about 50 nm occurs, whereas the microstrain of the Pd sublayer does not change significantly with annealing time.

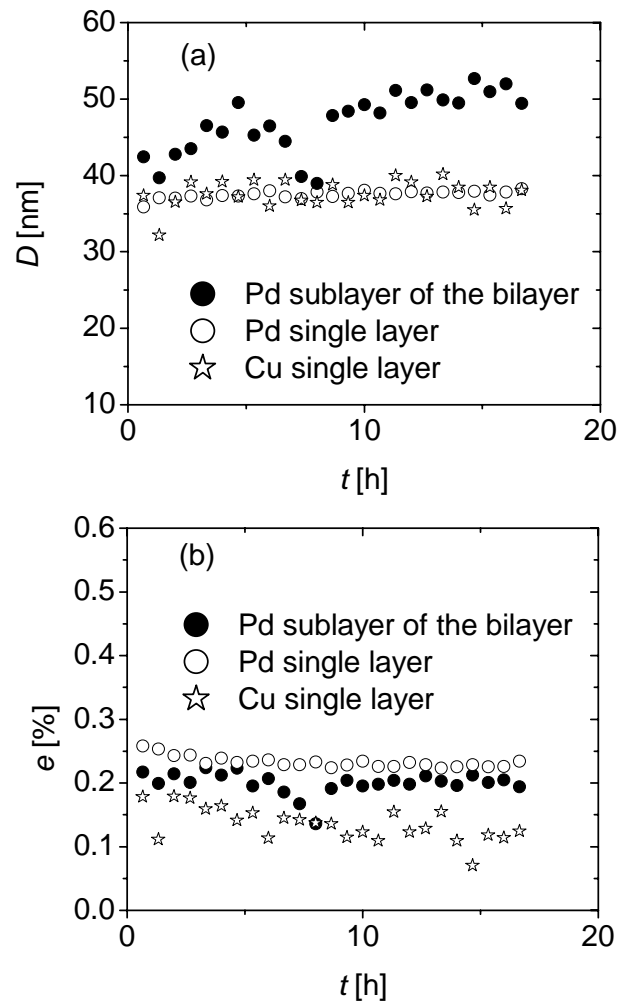


**Fig. 4.10:** Evolution of (a) crystallite size,  $D$ , and (b) microstrain,  $e$ , with time,  $t$ , for single Cu layer, single Pd layer and Pd sublayer of the bilayer during isothermal annealing at 185 °C. For all measurements,  $\psi=0^\circ$ , i.e. the diffraction vector is oriented perpendicular to the film surface.



## 4.4 Discussion

### 4.4.1 Thermoelastic behaviour

The thermoelastic slopes  $\Xi_{\text{layer}}$  of the (sub)layers can be calculated from the difference of the CTEs of the (sub)layers and the substrate ( $\alpha_{\text{layer}} - \alpha_{\text{substrate}}$ ) and the biaxial moduli of the (sub)layers  $M_{\text{layer}}$ :

$$\Xi_{\text{layer}} = M_{\text{layer}} (\alpha_{\text{layer}} - \alpha_{\text{substrate}}) \quad (7)$$

The biaxial moduli of the (sub)layers depend upon their texture state. Theoretical extremes have been calculated here for the cases of randomly oriented and perfectly  $\{111\}$ -fibre textured polycrystals [36]; the results have been gathered in Table 4.1, together with the experimentally obtained results for the single layer and bilayer specimens (cf. Section 4.3.4). It should be noted here that the CTEs of the Cu and Pd layers used in these calculations were experimentally measured from the variations of the strain-free lattice parameters of the single layers (cf. Eq.(4)) with temperature (below room temperature), since the CTE of a thin layer is generally and principally different from the literature value obtained for coarse-grained specimens [37]. From the results given in Table 4.1 it follows that the thermoelastic slopes calculated for the perfectly  $\{111\}$ -fibre textured polycrystals are appropriate estimates for thermoelastic slopes of the Cu and Pd single layers and the Cu and Pd sublayers of the diffusion couple (cf. Table 4.1), which is compatible with the pronounced strength of the  $\{111\}$  fibre texture observed experimentally (see also Fig. 4.3). Thereby also the application of the CGM method in the residual stress analysis is validated (see Section 4.2.4).

### 4.4.2 Overview of possible stress changes at elevated temperatures

#### 4.4.2.1 Mechanisms of stress development at elevated temperatures

In addition to purely thermoelastic behaviour, various mechanisms can lead to changes of the stress state during a heat treatment: (i) grain growth, (ii) defect annihilation and shrinkage of grain-boundary voids, (iii) plastic deformation, (iv) phase transformations and (v) interdiffusion (if the partial molar volumes of the components of the specimen are different and/or if a net vacancy flux occurs due to a difference of the intrinsic diffusion coefficients of the diffusing species which is not counterbalanced by vacancy generation and annihilation processes) [1,5].

For layers sputter-deposited at (about) room temperature mechanisms (i) and (ii) (both these relaxation processes are thermally activated) generally occur upon increasing the temperature (if not already at room temperature). These relaxation processes cause a film compaction by the annihilation of excess volume associated with defects and grain boundaries and, thus, tensile stress contributions are generated in the film system. Mechanism (iii) always leads to stress relaxation, i.e. a decrease of the absolute stress level. Mechanisms (iv) and (v), which will be discussed below in more detail for the Cu-Pd system, can induce both tensile and compressive stress contributions according to the sign of the net volume change in the layer. Hence, the net (observed) stress change is the outcome of a combination of a number of, possibly competing, sources of stress generation and relaxation.

### **Phase transformation**

From the results described in Section 4.3.3 it follows that ordered Cu<sub>3</sub>Pd ( $\alpha'$ ) is formed during isothermal annealing at 185 °C. The residual stress parallel to the surface invoked by ordering of a hypothetical, homogeneous, disordered Cu<sub>3</sub>Pd thin film can be calculated from the difference between the molar volumes of the ordered and the disordered phases ( $\Delta\Omega$ ) according to Eq. (8) [5]

$$\sigma = \frac{-E}{1-\nu} \frac{\Delta\Omega}{3\Omega_{\text{Cu}_3\text{Pd}}} \quad (8)$$

where  $\Omega_{\text{Cu}_3\text{Pd}}$  is the molar volume of the disordered Cu<sub>3</sub>Pd alloy and  $E$  and  $\nu$  are Young's modulus and Poisson's ratio of the film, respectively; for calculation it is assumed that  $E$  and  $\nu$  are unaffected by the ordering and that their values can be estimated by the composition-weighted arithmetic averages of the corresponding values for pure Cu and pure Pd [24,34]. The specific volume change upon ordering can be calculated on the basis of the lattice parameters of the ordered and disordered Cu<sub>3</sub>Pd [34,38]:  $\Delta\Omega/3\Omega_{\text{Cu}_3\text{Pd}} \approx -0.00135$ . The stress  $\sigma$  calculated on this basis by application of Eq. (8) for the transformation of a disordered Cu<sub>3</sub>Pd layer on a substrate to an ordered Cu<sub>3</sub>Pd layer is about 270 MPa. In the specimens investigated, only a minor volume fraction of Cu and Pd transforms to Cu<sub>3</sub>Pd. An analysis of the integrated intensities of the 111 reflections of Cu and Pd indicates that the transformed film volume fraction does not exceed 0.1. Thus, formation of the compound phase does not provide a significant contribution of tensile stress.

### Interdiffusion

Upon substitutional interdiffusion, stresses can be generated due to differences in (i) the partial molar volumes and/or (ii) the diffusion fluxes of the diffusing species. An assessment of the combined effect on stress if both sources of stress operate can be made as follows: The volume change,  $\Delta v_i$  ( $i = \text{Cu, Pd}$ ) resulting from concentration changes in the Cu and Pd layers can be expressed, assuming that the number of lattice sites in each layer is constant, as:

$$\Delta v_{\text{Cu}} = N_{\text{Pd}} (\Omega_{\text{Pd}} - \Omega_{\text{CuV}}) + N_{\text{Cu}} (\Omega_{\text{CuV}} - \Omega_{\text{Cu}}) \quad (9)$$

$$\Delta v_{\text{Pd}} = N_{\text{Pd}} (\Omega_{\text{PdV}} - \Omega_{\text{Pd}}) + N_{\text{Cu}} (\Omega_{\text{Cu}} - \Omega_{\text{PdV}}) \quad (10)$$

where the  $N_i$  are the moles of Cu and Pd crossing the initial interface during a diffusion anneal, the  $\Omega_i$  are the molar volumes of Cu and Pd and the  $\Omega_{iV}$  are the molar volumes of vacancies in Cu and Pd. Note that Eqs. (9) and (10) also hold if the components diffuse via grain boundaries but in the end become dissolved substitutionally in the bulk.

If the volume changes in the sublayers are accommodated elastically, the corresponding diffusion-induced stress parallel to the surface, as compared to the state before interdiffusion had occurred, can be calculated similarly to Eq. (8) according to

$$\sigma_i = \frac{-E_i}{1-\nu_i} \frac{\Delta v_i}{3v_i} \quad (11)$$

with  $E_i$  and  $\nu_i$  taken as the Young's modulus and Poisson's ratio of the pure, elemental layer  $i$ , respectively.

The sign of the diffusion-induced stress in the layers depends on the ratio  $N_{\text{Cu}}/N_{\text{Pd}}$ . The ratio  $-\Delta v_i/N_{\text{Pd}}$ , which is proportional to  $\sigma_i$  (Eq. (11)), has been plotted versus  $N_{\text{Cu}}/N_{\text{Pd}}$  for both sublayers in Fig. 4.11. Literature values for the molar volumes of Cu and Pd have been taken from Ref. [39] and the volume of a vacancy has been taken as half of the atomic volume. A positive value of  $\Delta v_i$  implies that compressive residual stress is built up, whereas tensile stress develops if  $\Delta v_i$  is negative. The larger the diffusional flux of Cu with respect to that of Pd (i.e. the larger  $N_{\text{Cu}}/N_{\text{Pd}}$ ), the more tensile (less compressive) the diffusion-induced stress in the originally pure Cu sublayer and the more compressive (less tensile) the diffusion-induced stress in the originally pure Pd sublayer (cf. Fig. 4.11).

A quantitative assessment of the resulting diffusional stresses in the Cu and Pd sublayers of the investigated specimens is not possible as the (intrinsic) diffusion fluxes of Cu and Pd (and thus  $N_{\text{Cu}}$  and  $N_{\text{Pd}}$ ) cannot be accessed experimentally.

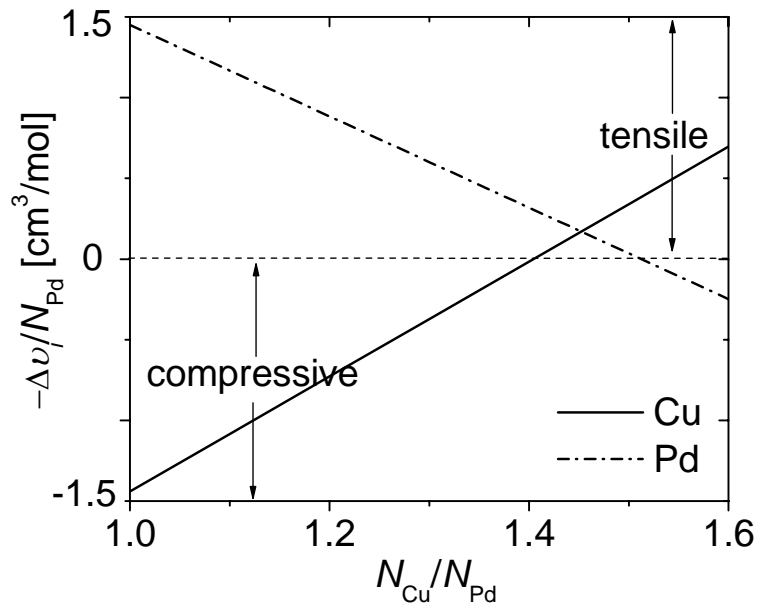


**Fig. 4.11:** The ratio,  $-\Delta v_i/N_{\text{Pd}}$  ( $i = \text{Cu, Pd}$ ), which is proportional to the diffusion-induced stress,  $\sigma_i$  (see Eq. (11)), versus  $N_{\text{Cu}}/N_{\text{Pd}}$ .

#### 4.4.2.2 Stress evolution in Cu-Pd bilayer during heating and isothermal annealing

The differences between the experimentally determined stress and the thermoelastic stress extrapolation to elevated temperatures for the *sublayers* represents the outcome of the possible stress contributions due to thermally activated processes as grain growth and annihilation of crystal defects and due to interdiffusion and/or phase formation, which may lead to a net increase or decrease of the (absolute value of) stress in the (sub)layer.

Interdiffusion and phase formation do not occur in the *single layers*. Hence, the stress contributions due to the processes as grain growth and annihilation of crystal defects can be obtained for the single layers as the difference between the experimentally observed stress at elevated temperature and the expected stress by extrapolation of the thermoelastic stress to elevated temperature (see Fig. 4.12).

The occurrence of plastic deformation can be neglected for both *sublayers* and *single layers* recognizing that the stress levels in Figs. 4.6, 4.7 and 4.8 are incompatible with yield of the 50 nm thick Cu and Pd layers at 185 °C, which has been verified by several heating cycles

performed in this project for single layer and bilayer specimens at a temperature range between 175 °C and 300 °C.

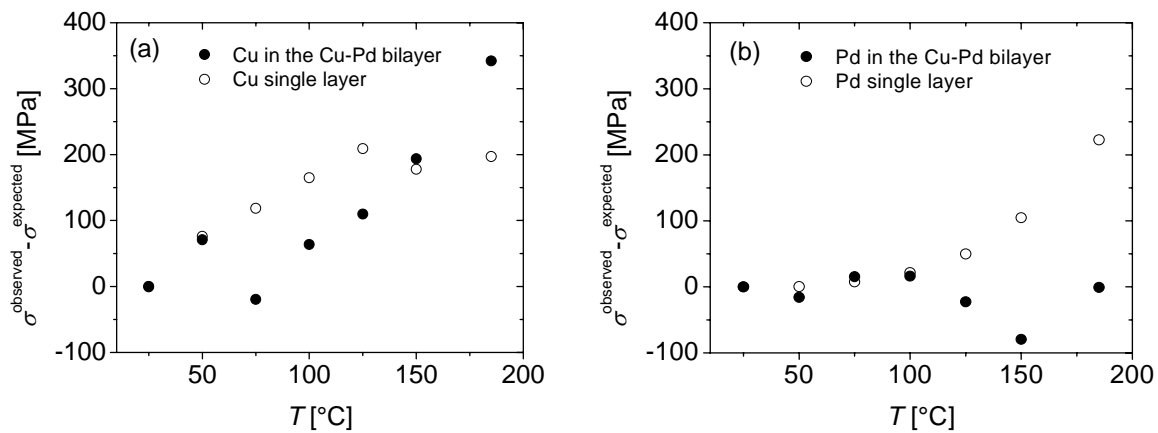


**Fig. 4.12:** Difference between extrapolated (thermoelastic slopes) and as measured stress for (a) Cu single layer and Cu layer of the bilayer (b) Pd single layer and Pd layer of the bilayer as a function of temperature,  $T$ .

### Heating to 185 °C

The annealing-induced stress contributions (after subtraction of the thermoelastic component; cf. above discussion) for the single Cu layer and the Cu sublayer in the diffusion couple are very similar: A considerable tensile stress contribution develops (Fig. 4.12(a)). The magnitude of the tensile stress generated upon heating to 185 °C is more than 100 MPa larger in the Cu sublayer. This difference cannot be ascribed to a different extent of grain growth (see Fig. 4.9(a)). Hence, as compared to the single Cu layer, a different mechanism of tensile stress development operates (additionally) in the Cu sublayer of the diffusion couple.

As for the Cu single layer and the Cu sublayer, it also holds for the Pd single layer and the Pd sublayer that there is no difference in extent of grain growth (see Fig. 4.9(b)). Then it follows from the results shown in Fig. 4.12(b) that a mechanism of compressive stress development operates (additionally) in the Pd sublayer of the diffusion couple (it has been found that a decrease of the crystalline imperfection, as evidenced by a decrease of the microstrain  $\epsilon$  (observed only for the Pd single layer; cf. Fig. 4.9(d)) only marginally affects the (macro) stress; cf. Refs. [18,40]).

With reference to the model calculations shown in Fig. 4.11, the above results could be interpreted as a consequence of a much larger flux of Cu into the Pd sublayer than of Pd into the Cu sublayer. If the flux of Cu atoms (stemming from a combination of bulk and grain boundary diffusion; cf. Section 4.3.1) towards the Pd-rich region of the couple exceeds the

counter flow of Pd atoms, an increase of the vacancy concentration in the Cu layer may occur which contributes to tensile stress development in Cu and compressive stress development in Pd [40,41].

### **Annealing at 185 °C**

(i) The single Cu layer exhibits an approximately constant stress level during isothermal annealing (cf. Fig. 4.7). (ii) Grain growth is negligible for the single Cu layer (cf. Fig. 4.10). From (i) and (ii) it follows that the stress evolution in the Cu sublayer of the diffusion couple is not considerably affected by thermally activated processes as grain growth and defect annihilation. Further (iii) stress generation in the Cu sublayer due to phase formation is insignificant (cf. Section 4.4.2.1). Hence, the tensile stress contribution occurring upon annealing in the Cu sublayer (Fig. 4.8) is likely dominantly due to the diffusional intermixing.

The single Pd layer exhibits an approximately constant stress level during isothermal annealing (cf. Fig. 4.7). A moderate increase of the crystallite size,  $D$ , from about 40 nm to about 50 nm occurs for the Pd sublayer of the diffusion couple (cf. Fig. 4.10). The crystallite size attains a constant, terminal value of about 50 nm already after annealing for about 10 hours. Therefore, in any case in the remaining part of the annealing period, the stress evolution in the Pd sublayer of the diffusion couple is not affected pronouncedly by thermally activated processes as grain growth and defect annihilation. Again, stress generation due to phase formation is insignificant (cf. Section 4.4.2.1). Hence, the tensile stress contribution occurring upon continued annealing in also the Pd sublayer (Fig. 4.8) is likely dominated by diffusional intermixing.

It should be noted that the change of stress in both sublayers of the couple is a linear function of  $t^{1/2}$  (Fig. 4.8) which supports ascribing the origin of stress change to diffusional intermixing.

Due to the moderate increase in the crystallite size of the Pd sublayer during heating up, Cu grain-boundary diffusion is less important during the subsequent isothermal anneal at 185 °C than during heating up (when, by diffusion, tensile stress is generated in the Cu layer and compressive stress is generated in the Pd layer; cf. above discussion under “Heating to 185 °C”). It is thereby possible that the total flux of Cu atoms entering the Pd-rich region of the couple has become relatively less and the regime is entered,  $1.4 < N_{\text{Cu}}/N_{\text{Pd}} < 1.5$ , where tensile stresses are induced in both sublayers (cf. Fig. 4.11).

## 4.5 Summary

- Annealing of Cu-Pd thin film (thickness of each sublayer: 50nm) diffusion couples at a temperatures of 185 °C leads to considerable diffusional intermixing. Whereas grain-boundary and volume diffusion are both significant mechanisms for diffusion of Cu atoms into the Pd sublayer, grain-boundary diffusion dominates for the diffusion of Pd atoms into the Cu-rich part of the coupled.
- Diffusional intermixing is accompanied by the formation of ordered Cu<sub>3</sub>Pd ( $\alpha'$ ).
- For the first time the evolution of stress in the separate sublayers was measured and analyzed in a thin-film bilayer system by X-ray diffraction measurements in-situ. A comparison with stresses measured for single layers allowed identification of stress contributions due to interdiffusion.
- Heating up to 185 °C of single Cu and Pd layers leads to tensile stress contributions in both single layers due to grain growth and/or defect annihilation (determined after correction for thermal misfit stress).
- Heating up to 185 °C of the Cu and Pd sublayers in the bilayer leads to a tensile stress in the Cu sublayer and a compressive stress in the Pd sublayer (determined after correction for thermal misfit stress and (tensile) stress contribution due to grain growth and/or defect annihilation). This result can be ascribed to interdiffusion with a much larger flux of Cu into Pd than vice versa.
- Annealing at 185 °C of the single Cu and Pd layers causes no further significant stress change in both single layers.
- Annealing at 185 °C of the Cu and Pd sublayers in the bilayer leads to tensile stress contributions in both sublayers. Because the grain-boundary density in the Pd sublayer decreases during the heating up to 185 °C, this result can be ascribed to interdiffusion with, as compared to the situation during heating up, a smaller flux of Cu into Pd relative to flux of Pd into Cu.

## Acknowledgement

We thank Mr. F. Thiele and Dr. G. Richter for the single and bilayer specimen production, Mr. B. Siegle for AES measurements, Dr. E. Bischoff for TEM investigations and Mrs. M. Dudek for assistance during the specimen preparation.

## References

- [1] L. B. Freund and S. Suresh, *Thin Film Materials Stress, Defect Formation and Surface Evolution*, (Cambridge Univ. Press, Cambridge, 2003).
- [2] M. Ohring, *Materials Science of Thin Films*, (Academic Press, San Diego, 2002).
- [3] B. Okolo, P. Lamparter, U. Welzel, T. Wagner and E. J. Mittemeijer, *Thin Solid Films* **474**, 50 (2005).
- [4] B. Okolo, P. Lamparter, U. Welzel and E. J. Mittemeijer, *J. Appl. Phys.* **95**, 466 (2004).
- [5] M. F. Doerner and W. D. Nix, *Crit. Rev. Solid State* **14**, 225 (1988).
- [6] J. Chakraborty, U. Welzel and E. J. Mittemeijer, unpublished.
- [7] P. G. Shewmon, *Diffusion in Solids*, (TMS Publication, Warrendale, 1989).
- [8] J. C. M. Li, *Metall. Trans. A* **9A**, 1353 (1978).
- [9] D. W. Stevens and G. W. Powell, *Metall. Trans. A* **8**, 1531 (1977).
- [10] F. C. Larche and J. W. Cahn, *Acta Metall.* **30**, 1835 (1982).
- [11] F. C. Larche and J. W. Cahn, *Acta Metall.* **33**, 331 (1985).
- [12] U. Welzel, P. Lamparter, M. Leoni and E. J. Mittemeijer, *Mater. Sci. Forum* **347**, 405 (2000).
- [13] U. Welzel, P. Lamparter and E. J. Mittemeijer, *Mater. Res. Soc. Symp. Proc.* **562**, 147 (1999).
- [14] N. Balandina, B. Bokstein and A. Ostrovsky, *Defect Diffus. Forum* **156**, 181 (1998).
- [15] A. S. Ostrovsky and B. S. Bokstein, *Appl. Surf. Sci.* **175**, 312 (2001).
- [16] U. Welzel, J. Ligot, P. Lamparter, A. C. Vermeulen and E. J. Mittemeijer, *J. Appl. Cryst.* **38**, 1 (2005).
- [17] M. Wohlschlögel, U. Welzel, G. Maier and E. J. Mittemeijer, *J. Appl. Cryst.* **39**, 194 (2006).
- [18] Y. Kuru, M. Wohlschlögel, U. Welzel and E. J. Mittemeijer, *J. Appl. Cryst.* **41**, 428 (2008).
- [19] A. Strecker, U. Baeder, M. Kelsch, U. Salzberger, M. Sycha, M. Gao, G. Richter and K. V. Benthem, *Z. Metallkd.* **94**, 3 (2003).
- [20] P. S. Ho, J. E. Lewis and L. K. Howard, *J. Vac. Sci. Technol.* **14**, 322 (1977).
- [21] M. Wohlschlögel, T. U. Schüllli, B. Lantz and U. Welzel, *J. Appl. Cryst.* **41**, 124 (2008).



- [22] M. Wohlschlögel, T. U. Schüllli, G. Maier, U. Welzel and E. J. Mittemeijer, *Z. Kristallogr. Suppl.* **26**, 147 (2007).
- [23] *Profit User's Guide*, (Philips Analytical X-ray, Delft, 1996).
- [24] W. F. Gale and T. C. Totemeier, *Smithells Metals Reference Book*, (Elsevier, Amsterdam, 2004).
- [25] U. Welzel and E. J. Mittemeijer, *J. Appl. Phys.* **93**, 9001 (2003).
- [26] U. Welzel and E. J. Mittemeijer, *Mater. Sci. Forum* **443**, 131 (2004).
- [27] R. Delhez, Th. H. de Keijser and E. J. Mittemeijer, *Fresen. Z. Anal. Chem.* **312**, 1 (1982).
- [28] Th. H. de Keijser, J. I. Langford, E. J. Mittemeijer and A. B. P. Vogels, *J. Appl. Cryst.* **15**, 308 (1982).
- [29] J. I. Langford, *J. Appl. Cryst.* **11**, 10 (1978).
- [30] J. I. Langford, R. Delhez, Th. H. de Keijser and E. J. Mittemeijer, *Aust. J. Phys.* **41**, 173 (1988).
- [31] E. J. Mittemeijer and P. Scardi, *Diffraction Analysis of the Microstructure of Materials*, (Springer, Berlin, 2004).
- [32] J. Y. Wang and E. J. Mittemeijer, *J. Mater. Res.* **19**, 3389 (2004).
- [33] S. Hofmann, *Surf. Interface Anal.* **21**, 673 (1994).
- [34] P. R. Subramanian and D. E. Laughlin, *J. Phase Equilib.* **12**, 231 (1991).
- [35] T. B. Massalski, *Binary Alloy Phase Diagrams*, (ASM International, Metals Park, 1990).
- [36] W. D. Nix, *Met. Trans. A* **20**, 2217 (1989).
- [37] Y. Kuru, M. Wohlschlögel, U. Welzel and E. J. Mittemeijer, *Appl. Phys. Lett.* **90**, 243113 (2007).
- [38] Y. S. Touloukian, *Thermal Expansion: Metallic Elements and Alloys*, (IFI/Plenum, New York, 1975).
- [39] [www.webelements.com](http://www.webelements.com)
- [40] Y. Kuru, J. Chakraborty, U. Welzel, M. Wohlschlögel and E. J. Mittemeijer, *Mater. Sci. Forum* **524-5**, 801 (2006).
- [41] U. Welzel and E. J. Mittemeijer, *Diffus. Defect Data* **264**, 71 (2007).



# Chapter 5

## Kurzfassung der Dissertation in deutscher Sprache

### 5.1 Einleitung

Dünne Metallschichten wurden aufgrund ihrer außergewöhnlichen mechanischen, elektrischen und magnetischen Eigenschaften ausführlich untersucht (siehe z.B. [1-4]). Sie können sehr hohe Eigenspannungen aufweisen, welche vom Schichtwachstum, von thermisch aktivierten Vorgängen (wie Kornwachstum, Diffusion etc.) oder von äußeren Einflüssen herrühren können. Abgesehen von direkten mechanischen Konsequenzen (Delaminieren etc.) können eine Reihe von Prozessen wie etwa Kornwachstum und Diffusion von diesen Spannungen und ihren Gradienten beeinflusst werden [5,6]. Demzufolge ist es äußerst wichtig Eigenspannungen in dünnen Schichten zu messen und ein grundlegendes Verständnis für den Auf- und Abbau von Eigenspannungen zu entwickeln.

Röntgendiffraktometrie ist eine der am häufigsten verwendeten Methoden zur Messung von Eigenspannungen [7]. Die Methode arbeitet zerstörungsfrei, ist äußerst empfindlich (Eigenspannungen und deren Änderungen von wenigen MPa können detektiert werden) und ermöglicht es, die Spannungszustände aller kristallinen Phasen in einer Schichtstruktur separat zu bestimmen. Durch eine geeignete Auswertung können unter bestimmten Voraussetzungen auch spannungsfreie Gitterparameter bestimmt werden. Darüber hinaus können zusätzliche Informationen über die Mikrostruktur, wie die kristallographische Textur, die Dichte kristalliner Defekte wie z.B. Versetzungen und die Kristallitgröße aus den gemessenen Diffraktogrammen ermittelt werden und die Analyse von (Eigenspannungs-) Gradienten ist möglich [8-10].

Diese Arbeit ist der Untersuchung von mikrostrukturellen Veränderungen, Eigenspannungen und Interdiffusion in dünnen Schichten mittels in-situ Röntgenbeugungsuntersuchungen gewidmet. Von zentraler Bedeutung sind hierbei methodische Aspekte von in-situ Röntgenbeugungsmessungen, welche in Kapitel 2 detailliert diskutiert werden und in den darauf folgenden Kapiteln 3 und 4 zur Anwendung kommen.

## **5.2 Röntgenographische Eigenspannungsanalyse dünner Schichten durch temperaturabhängige in-situ Messungen unter- und oberhalb der Raumtemperatur: Bestimmung der thermoelastischen Konstanten nanokristalliner Materialien und Identifizierung der Quellen von Eigenspannungen**

In Kapitel 2 der Arbeit wurden methodische Aspekte, die mit temperaturabhängigen in-situ Spannungsanalysen verbunden sind, betrachtet. Dazu zählen insbesondere die Kalibrierung einer Heiz-/Kühlkammer, die Messung von linearen thermischen Ausdehnungskoeffizienten (ThAK) und die Differenzierung von durch thermisch aktivierte Prozesse (z.B. Kornwachstum) hervorgerufenen Spannungen von thermo-elastischen Spannungen.

In den Experimenten wurden dünne Pd und Ni Schichten (nominelle Dicke 50 nm) benutzt, die bei Raumtemperatur auf (100)-orientierte Si Wafer, welche mit dünnen, amorphen, SiO<sub>2</sub> und Si<sub>3</sub>N<sub>4</sub> Diffusionsbarrieren beschichtet waren, mittels DC Magnetronspütern unter UHV-Bedingungen (Basisdruck  $\sim 1 \times 10^{-10}$  mbar) abgeschieden wurden.

Alle Röntgenbeugungsmessungen wurden an einem Bruker D8 Discover Diffraktometer, das mit einer Eulerwiege ausgerüstet war, durchgeführt. In dem Diffraktometer wurde aus Cu K $\alpha$  Strahlung, welche durch eine Drehanode (Bruker TXS) erzeugt wurde, mittels eines kollimierenden Spiegels ein quasi-paralleler Strahl erzeugt. Der gebeugte Strahl passierte einen Parallelplattenkollimator (Akzeptanzwinkel 0,23°) und wurde anschließend von einem Szintillationszähler registriert. Auf dem Probenhalter war eine Heiz-/Kühlkammer (Anton Paar DCS 350) montiert, mit der es möglich ist, im Vakuum (ca. 10<sup>-3</sup> mbar) Temperaturen zwischen -100 °C und 350 °C einzustellen (für weitere Details, siehe [11-13]).

### **5.2.1 Kalibrierung einer Heiz-/Kühlkammer und Messung des thermischen Ausdehnungskoeffizienten**

Mit röntgenografischen in-situ Spannungsmessungen ist es möglich, entweder:

- (i) eine Kalibrierung der verwendeten Heiz-/Kühlkammer in-situ durchzuführen oder
- (ii) eine Bestimmung des ThAK von Substrat und/oder dünner Schicht durchzuführen.

Für die Kalibrierung der Kammer (i) muss der ThAK der Schicht oder des Substrates genau bekannt sein, während eine genaue Kalibrierung der Kammer die Bestimmung der ThAK von Schicht und Substrat ermöglicht (ii).

#### (i) Kalibrierung der Heiz-/Kühlkammer.

Die Temperatur einer Pd-Schicht,  $T$ , welche durch direkte Messung erhalten wurde (Widerstandsthermometrie; siehe Ref. [11]) und die berechnete Temperatur,  $T_{\text{calc}}$ , die aus der mittels röntgenographischer in-situ Eigenspannungsanalyse experimentell ermittelten Temperaturabhängigkeit der spannungsfreien Gitterkonstanten [11] unter Zuhilfenahme von Daten für die thermische Ausdehnung aus der Literatur [14,15] abgeleitet wurde, sind als Abszisse bzw. Ordinate in Abb. 5.1 (a) aufgetragen (für Details zur Bestimmung des spannungsfreien Gitterparameters aus Röntgenbeugungsmessungen, siehe [7]). Die durchgezogene Linie in der Abbildung entspricht dem Fall, dass  $T = T_{\text{calc}}$  gilt. Es folgt, dass die Temperatur  $T_{\text{calc}}$ , die aus der in-situ Temperaturkalibrierung erhalten wurde, gut mit der direkt gemessenen Proben temperatur  $T$  übereinstimmt. Die für eine Ni-Schicht erhaltenen Ergebnisse sind in Abb. 5.1 (b) aufgetragen. Im Gegensatz zur Pd-Schicht (Abb. 5.1. (a)) unterscheiden sich hier  $T$  und  $T_{\text{calc}}$  systematisch voneinander: Die mittels der in-situ Methode bestimmte Temperatur liegt unterhalb der Raumtemperatur unter der mittels Widerstandsthermometrie ermittelten Temperatur; die Abweichung nimmt mit abnehmender Temperatur zu. Es wird im Folgenden gezeigt, dass diese Abweichungen darauf zurückzuführen sind, dass sich die ThAK von fein- bzw. nanokristallinen Schichten erheblich von denen von grobkristallinen Vielkristallen unterscheiden können (siehe auch Kapitel 3 und 5.3).

#### (ii) Bestimmung der thermischen Ausdehnungskoeffizienten von Schicht und/oder Substrat.

Der ThAK kann aus der Steigung einer Ausgleichsgeraden in einer Auftragung der thermischen Dehnung,  $\varepsilon_{\text{th}}$  ( $= \Delta d/d_0$ , wobei  $d_0$  der Abstand der betrachteten Gitterebenen bei Raumtemperatur und  $\Delta d$  die Änderung des Gitterebenenabstands bei einer Temperaturänderung um  $\Delta T$  ist), gegen die Temperatur,  $T$  bestimmt werden. Exemplarische Ergebnisse für die Pd- und Ni-Schichten sind in Tabelle 5.1 zusammengefasst. In Übereinstimmung mit den oben diskutierten Ergebnissen zur Temperaturkalibration wurde für die Pd-Schicht eine relativ gute Übereinstimmung des gemessenen ThAK und des aus der Literatur entnommenen ThAK beobachtet, wohingegen eine wesentlich schlechtere Übereinstimmung im Falle der Ni-Schicht auftrat.

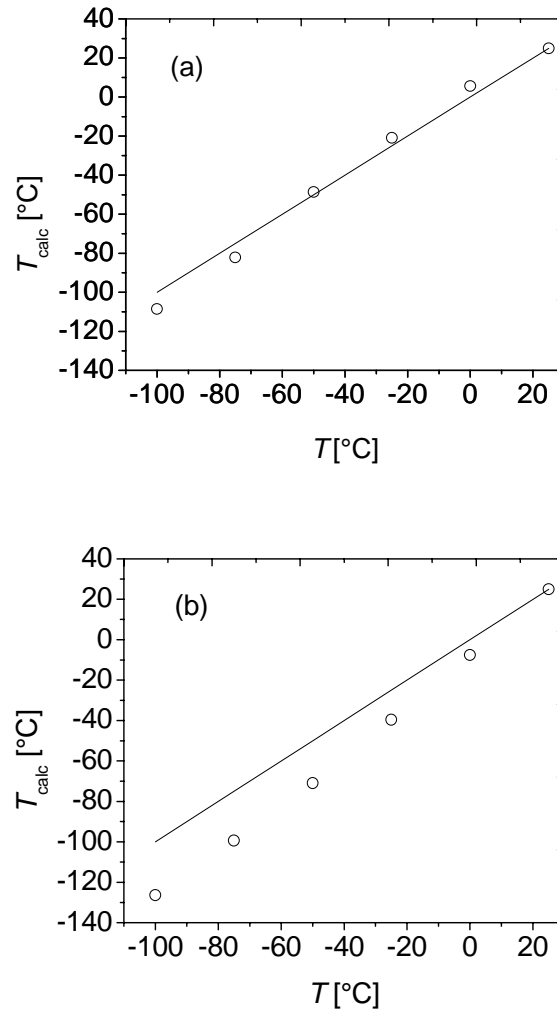


**Abb. 5.1:** Temperatur,  $T_{\text{calc}}$ , berechnet aus mittels Röntgenbeugungsmessungen bestimmten dehnungsfreien Gitterparametern (a) der Pd-Schicht (b) der Ni-Schicht aufgetragen gegen die wahre Probestemperatur,  $T$ , die mittels Widerstandsthermometrie bestimmt wurde.

**Tabelle 5.1:** Thermische Ausdehnungskoeffizienten von Pd- und Ni-Schichten. Experimentell ermittelte Werte und Literaturwerte für den Temperaturbereich zwischen Raumtemperatur und  $-100\text{ }^{\circ}\text{C}$ . Die empfohlene Funktion [14] beziehungsweise die Daten von Altman *et al.* [15] wurden zur Berechnung der Literaturdurchschnittswerte des ThAK der Pd- und der Ni-Schicht verwendet.

<b>Für die Pd- und Ni-Schichten ermittelte thermische Ausdehnungskoeffizienten</b>			
<b>Pd</b>		<b>Ni</b>	
Experimentell ermittelter Wert [ $1/^{\circ}\text{C}$ ]	Literaturwert [ $1/^{\circ}\text{C}$ ]	Experimentell ermittelter Wert [ $1/^{\circ}\text{C}$ ]	Literaturwert [ $1/^{\circ}\text{C}$ ]
$(12.0 \pm 0.6) \times 10^{-6}$	$11.2 \times 10^{-6}$	$(13.7 \pm 0.4) \times 10^{-6}$	$12.4 \times 10^{-6}$

Es wird in Kapitel 3 der Arbeit (siehe auch Kapitel 5.3) gezeigt, dass diese offensichtliche Abweichung, welche im Fall der Ni-Schicht erhalten wird, eine Folge davon

ist, dass der ThAK von Ni-Volumenmaterial, der für die Berechnung der Ordinatenwerte in Abb. 5.1(b) verwendet wurde, hierfür ungeeignet ist.

### 5.2.2 Differenzierung von durch thermisch aktivierte Relaxationsprozesse hervorgerufenen Spannungen von thermo-elastischen Spannungen

Die röntgenographische in-situ Eigenspannungsanalyse bietet die Möglichkeit, thermo-elastische Spannungen (bedingt durch die Differenz der ThAKs von dünner Schicht und Substrat) von Spannungen, die von thermisch aktivierten Relaxationsprozessen bei hohen Temperaturen (wie Kornwachstum und Defektannihilation) hervorgerufen werden, zu unterscheiden. Darüber hinaus können Änderungen in der Kristallitgröße und den Mikrodehnungen (verknüpft mit der Defektdichte) durch Auswertung der Verbreiterung von Beugungslinien in-situ verfolgt werden [8].

Exemplarisch soll eine dünne Ni-Schicht betrachtet werden. Diese wurde zunächst von Raumtemperatur auf  $-100\text{ °C}$  abgekühlt, danach wieder aufgeheizt und anschließend wurde die Schicht zwischen Raumtemperatur und  $250\text{ °C}$  wärmebehandelt (insgesamt vier Zyklen zwischen Raumtemperatur und  $250\text{ °C}$ ). In Temperaturschritten von  $25\text{ °C}$  wurden Spannungsmessungen auf Basis der Kristallitgruppenmethode [7] durchgeführt. Die erhaltenen mechanischen Spannungen  $\sigma$  (ebener, rotationssymmetrischer Spannungszustand) zwischen  $-100\text{ °C}$  und  $100\text{ °C}$  sind für den ersten Zyklus in Abb. 5.2 dargestellt.

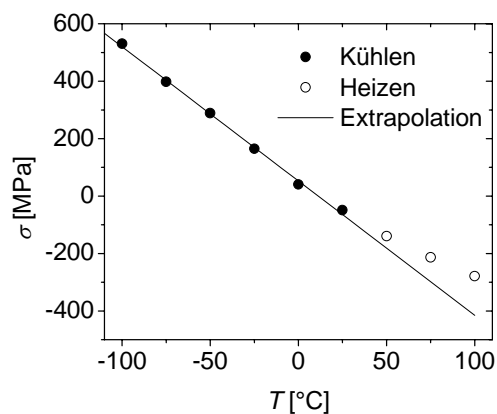


**Abb. 5.2:** Auftragung der Spannung gegen die Temperatur für die Ni-Schicht im Temperaturbereich zwischen  $-100\text{ °C}$  und  $100\text{ °C}$ . Die durchgezogene Linie stellt die lineare Extrapolation der Daten aus dem Temperaturbereich  $-100\text{ °C}$  bis  $25\text{ °C}$  zu erhöhten Temperaturen dar.

Die lineare Extrapolation des thermoelastischen Verhaltens, das während des Kühlens unterhalb von Raumtemperatur ( $25\text{ °C}$ ) beobachtet wird, zu Temperaturen oberhalb von Raumtemperatur ( $25\text{ °C}$ ) zeigt, dass die beobachtete Spannungsänderung bereits beim Heizen

zu leicht erhöhten Temperaturen (Temperaturbereich 25 °C-50 °C) nicht mehr völlig der Differenz der ThAK von Schicht und Substrat zugeschrieben werden kann (siehe Abb. 5.2). Offensichtlich treten unmittelbar oberhalb von Raumtemperatur thermisch aktivierte Prozesse auf, welche zu Spannungen führen die sich mit der Druckeigenspannung (hervorgerufen durch die erhöhte Temperatur und den Unterschied der Ausdehnungskoeffizienten von Schicht und Substrat) überlagern. Diese oberhalb der Raumtemperatur zusätzlich erzeugte Spannung ergibt sich aus der Differenz zwischen der beobachteten Spannung,  $\sigma^{\text{beob}}$ , und der entsprechend der linearen Extrapolation der unterhalb von Raumtemperatur erwarteten Spannung,  $\sigma^{\text{extrapol}}$ . Die Ergebnisse sind in Abb. 5.3 dargestellt. Beim Heizen oberhalb von Raumtemperatur ist die Differenz  $\sigma^{\text{beob}} - \sigma^{\text{extrapol}}$  beträchtlich und erreicht bei ungefähr 225 °C einen Plateauwert (Abb. 5.3).

Die Änderungen der Kristallitgröße  $D$  und der Mikrodehnung  $\varepsilon$  (erhalten aus der Auswertung einer einzelnen Beugungslinie, bei der der Cauchy-Anteil der Verbreiterung der Kristallitgröße und der Gauss-Anteil der Mikrodehnung zugeschrieben wird [16,17]) während des ersten Heizzyklus sind in Abb. 5.4 dargestellt.  $\sigma^{\text{beob}} - \sigma^{\text{extrapol}}$  ist offensichtlich eine Folge von Relaxationsprozessen verbunden mit Kornwachstum und/oder der Annihilation kristalliner Defekte (siehe auch Kapitel 2 und 4).

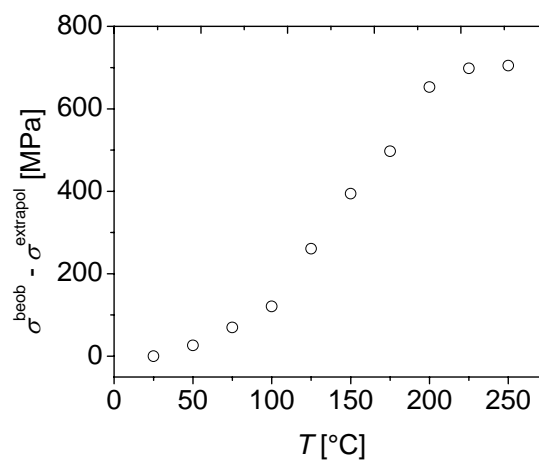


**Abb. 5.3:** Differenz zwischen experimentell beobachteter Spannung und erwarteter Spannung (entsprechend der linearen Extrapolation der Daten aus den Kühllexperimenten zu erhöhten Temperaturen) beim Aufheizen der Ni-Schicht.



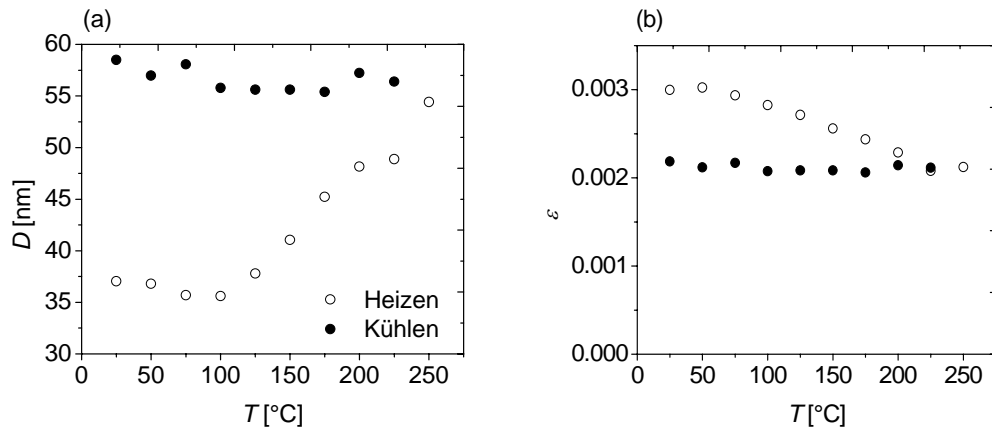


**Fig. 5.4:** Auftragung der Kristallitgröße,  $D$ , (a) und der Mikrodehnung,  $\varepsilon$ , (b) gegen die Temperatur für den ersten thermischen Zyklus der Ni-Schicht.

### 5.3 Kristallitgrößenabhängigkeit des thermischen Ausdehnungskoeffizienten von Metallen

Kapitel 3 ist dem thermischen Ausdehnungskoeffizienten (ThAK) von nanokristallinen Materialien gewidmet. Nanokristalline Materialien stehen wegen ihrer besonderen Eigenschaften im Brennpunkt der Materialforschung. Die thermische Ausdehnung spielt vor allem für Komponenten in der Mikroelektronik, der Mechanik etc., die insbesondere auch aus nanokristallinen Materialien mit unterschiedlichen Ausdehnungskoeffizienten zusammengesetzt sind, eine sehr große Rolle. Der ThAK von nanokristallinen Materialien wurde sowohl theoretisch als auch experimentell in einer Vielzahl von Studien untersucht. In der Literatur findet man mehrere widersprüchliche Beobachtungen bezüglich der Kristallitgrößenabhängigkeit des ThAK [18-20]. Auf Basis der in Kapitel 2 erörterten methodischen Entwicklungen kann die Kristallitgrößenabhängigkeit des ThAK verfolgt werden.

In den Experimenten wurden Cu und Ni Dünnschichten (die nominellen Dicken waren jeweils 50 nm) verwendet, die bei Raumtemperatur auf (100)-orientierte Si-Wafer, welche mit dünnen amorphen SiO<sub>2</sub> und Si<sub>3</sub>N<sub>4</sub> Diffusionsbarrieren (je 50 nm dick) beschichtet waren, mittels DC Magnetronspütern unter UHV-Bedingungen (Basisdruck ungefähr  $1 \times 10^{-10}$  mbar) abgeschieden wurden. Röntgenbeugungsmessungen wurden an einem Bruker D8 Discover Diffraktometer, das mit einer auf einer Eulerwiege montierten Heiz-/Kühlkammer ausgerüstet war, durchgeführt (siehe Kapitel 2.3 und 5.2 für Details der Röntgenbeugungsmessungen).

Zunächst wurden spannungsfreie Gitterebenenabstände der Cu und Ni Schichten mittels röntgenographischer in-situ Eigenspannungsanalyse ermittelt. Die ThAKs werden aus den Steigungen der Ausgleichsgeraden in den Auftragungen von thermischer Dehnung,  $\varepsilon_{th}$  (=  $\Delta d/d_0$ , wobei  $d_0$  der Abstand bestimmter Gitterebenen bei Raumtemperatur und  $\Delta d$  die Änderung des Gitterebenenabstands bei einer Temperaturänderung um  $\Delta T$  ist), gegen Temperatur,  $T$ , bestimmt. Es wurde beobachtet, dass die ThAKs der nanokristallinen Cu- und Ni-Schichten direkt nach der Herstellung signifikant (um ca. 10 %) größer sind als Werte, die für grobkristallines Cu- und Ni- Volumenmaterial erhalten werden (vgl. Abb. 5.5 und Tabelle 5.2).

Es hat sich als sehr wichtig erwiesen, dass die Messungen der ThAK bei Temperaturen unterhalb der Raumtemperatur durchgeführt werden konnten. Es konnte nämlich durch in-situ Röntgenbeugungsmessungen gezeigt werden, dass bei Temperaturen oberhalb der

Raumtemperatur sehr schnell eine Vergrößerung der Kornstruktur einsetzt (Abb. 5.6). Nach dieser Vergrößerung ergeben sich die für grobkristalline Vielkristalle erwarteten Ausdehnungskoeffizienten (vgl. Tabelle 5.2).

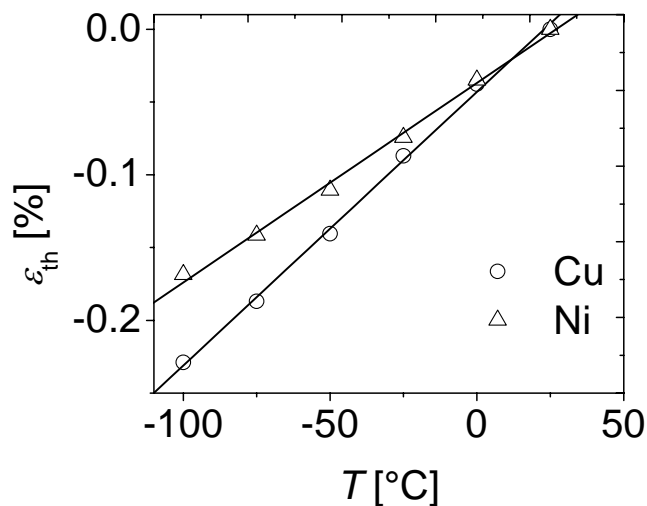


**Abb. 5.5:** Thermische Dehnung,  $\epsilon_{th}$ , der Cu- und Ni-Schichten direkt nach der Herstellung, im nanokristallinen Zustand, als Funktion der Temperatur,  $T$ . Die ThAKs sind die Steigungen der angepassten Ausgleichsgeraden.

**Tabelle 5.2:** Gegenüberstellung der Ausdehnungskoeffizienten und Korngrößen der untersuchten Kupfer- und Nickelschichten vor und nach der Wärmebehandlung. Zum Vergleich wurden auch Literaturwerte für die Ausdehnungskoeffizienten von Kupfer und Nickel angegeben [14,15].

	Ausdehnungskoeffizient $\alpha$ von Kupfer [ $10^{-6} / ^\circ\text{C}$ ]	Ausdehnungskoeffizient $\alpha$ von Nickel [ $10^{-6} / ^\circ\text{C}$ ]
Nach der Herstellung	$18.8 \pm 0.4$	$13.7 \pm 0.4$
Nach der Wärmebehandlung	$17.4 \pm 0.4$	$12.6 \pm 0.2$
Literaturwert für grobkristalline Materialien	15.7	12.4
	Korngröße $D$ von Kupfer [nm]	Korngröße $D$ von Nickel [nm]
Nach der Herstellung	26	37
Nach der Wärmebehandlung	41	59

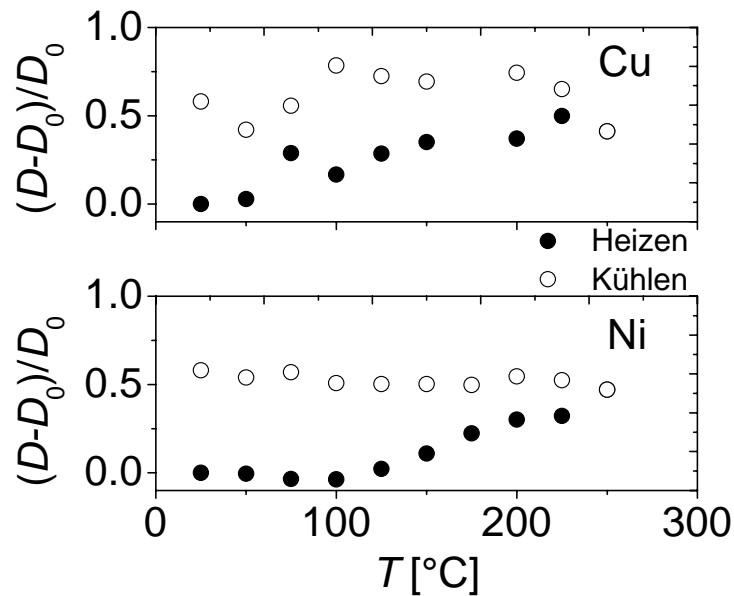


**Abb. 5.6:** Die relative Veränderung der Kristallitgröße der Cu- und Ni-Schichten bezogen auf die Korngröße direkt nach der Herstellung,  $D_0$ , als Funktion der Temperatur,  $T$ . Nach einem thermischen Zyklus zwischen Raumtemperatur und 250 °C stieg die Korngröße um mehr als 50 % an. Die Kristallitgrößen der Schichten wurden durch Auswertung der Linienverbreiterung einer einzelnen Beugungslinie bestimmt [16,17].

Die Abhängigkeit des ThAK von der Kristallitgröße kann verstanden werden, wenn man die Bindungsverhältnisse an Korngrenzen und Oberflächen betrachtet. Atome an der Oberfläche eines Kristalls oder an einer (inkohärenten) Grenzfläche (Korngrenze) sind im Bezug auf ihren Bindungszustand ungesättigt; ihre Koordinationszahl ist geringer als die der Atome im Volumen. In Folge dessen ergeben sich entsprechend unterschiedliche Potentialverläufe (Energie aufgetragen gegen interatomaren Abstand): Siehe Abb. 5.7. Für Atome an Oberflächen zeigt die Potentialkurve ein weniger tiefes Minimum und verläuft asymmetrischer als für Atome im Volumen. Gleiche thermische Energien führen durch die Asymmetrie der Potentialverläufe nun zu unterschiedlichen thermischen Ausdehnungen für Atome an Oberflächen und im Volumen. Je kleiner ein Kristallit ist, desto größer ist das Verhältnis der Anzahl der Oberflächenatome zur Anzahl der Atome im Volumen. Folglich ist die *mittlere* thermische Ausdehnung eines Kristallites umso größer, je kleiner der Kristallit ist.

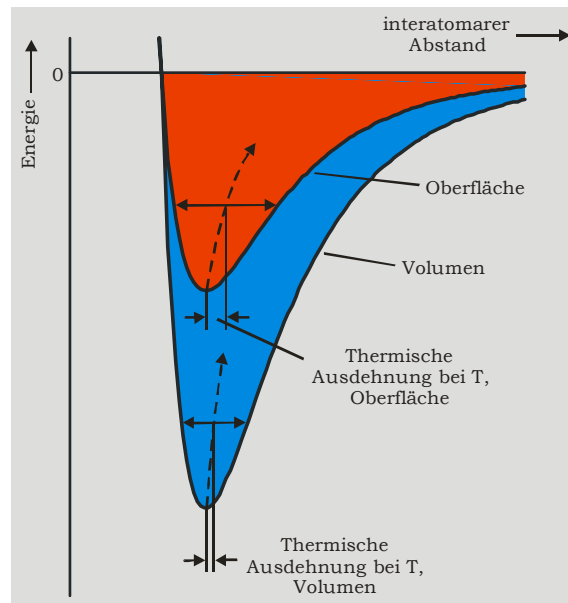


**Abb. 5.7:** Potentielle Energie als Funktion des interatomaren Abstands für Volumen- und Oberflächenatome.

## 5.4 Interdiffusion und Spannungsaufbau in Diffusionspaaren aus Cu-Pd Dünnschichten

Trotz der wissenschaftlichen und technologischen Bedeutung sind systematische Untersuchungen zum Einfluss von Interdiffusion und Phasenumwandlungen auf Eigenspannungen in dünnen Schichten selten. Aus diesem Grund wurden in Kapitel 4 dieser Arbeit Interdiffusion, Phasenbildung und Spannungsentwicklung in Diffusionspaaren aus dünnen Cu/Pd Doppelschichten (Schichtdicke einer Einzelschicht 50 nm) mit Hilfe von in-situ Röntgenbeugungsuntersuchungen, Auger-Elektronenspektroskopie (AES), kombiniert mit Ionensputtern, und Transmissionselektronenmikroskopie (TEM) untersucht. Die Doppelschichten wurden durch DC-Magnetron Sputtern auf Si-Substrate, welche mit amorphen Zwischenschichten ( $\text{Si}_3\text{N}_4$  und  $\text{SiO}_2$ ) beschichtet waren, abgeschieden. Cu- und Pd-Einzelschichten, die unter identischen Bedingungen abgeschieden und wärmebehandelt wurden, wurden als Vergleichsproben verwendet um insbesondere Spannungen, die durch Diffusion hervorgerufen werden, zu identifizieren.

Bei den in-situ Röntgenbeugungsmessungen wurden die Proben (sowohl die Cu- und Pd-Einzelschichten als auch die Cu-Pd Doppelschicht) zunächst von Raumtemperatur auf  $-100\text{ °C}$  gekühlt, danach wieder bis Raumtemperatur erwärmt, anschließend auf  $185\text{ °C}$  geheizt, bei dieser Temperatur für 16 Stunden und 40 Minuten isotherm wärmebehandelt und schließlich wieder auf Raumtemperatur abgekühlt. Außer beim letzten Heizschritt von  $150\text{ °C}$  auf  $185\text{ °C}$  wurde die Temperatur stets in Schritten von  $25\text{ °C}$  während des Heizens und Kühlens geändert (für experimentelle Details, siehe auch Kapiteln 5.2 und 4.2.4). Da ausgeprägte  $\{111\}$ -Fasertexturen auftraten, wurden die Eigenspannungen bei jedem Temperaturschritt mit Hilfe der Kristallitgruppenmethode (KGM) bestimmt (siehe Kapitel 4.2).

### 5.4.1 Interdiffusion

In Abb. 5.8 sind drei exemplarische, mit AES aufgezeichnete, Zusammensetzungs-Tiefenprofile dargestellt. Bereits bei  $185\text{ °C}$  tritt eine beträchtliche Vermischung der beiden Metallschichten durch Diffusion auf. Abgesehen von einer Veränderung der Steigung im Konzentrations-Tiefenprofil an der Stelle der ursprünglichen Grenzfläche zwischen den Schichten kann man in den Sputter-Tiefenprofilen der ausgelagerten Proben ein Konzentrationsplateau mit einer Pd-Konzentration in Cu von wenigen Prozent erkennen, in dem die Cu-Konzentration mit der Auslagerungszeit zunimmt. Dies Plateau entsteht durch

die Diffusion von Pd durch die Cu-Korngrenzen gefolgt von Seitwärtsdiffusion von Pd aus der Korngrenze in die Cu-Körner (Untersuchungen mittels Transmissionselektronenmikroskopie ergaben, dass die Schichten im wesentlichen eine kolumnare Mikrostruktur aufweisen). Es wurde bestätigt, dass die Änderung der Plateaukonzentration von Pd mit zunehmender Auslagerungszeit bei einer bestimmten Auslagerungstemperatur ein  $\sqrt{t}$ -Verhalten zeigt [21]. Andererseits sind Cu-Atome auf der Oberfläche der Pd-Schicht vorhanden - jedoch nur in vernachlässigbarer Konzentration im Plateaubereich. Dies deutet darauf hin, dass in diesem Fall in erheblichem Maße Korngrenzendiffusion auftritt, Volumendiffusion von Cu in Pd jedoch vernachlässigbar ist.

#### 5.4.2 Phasenzusammensetzung

Abb. 5.9 zeigt Ausschnitte aus den Diffraktogrammen einer Probe nach der Herstellung und von Proben, die für verschiedene Zeiten bei 185 °C ausgelagert wurden ( $\psi = 0^\circ$ , d.h. der Beugungsvektor steht senkrecht zur Schichtoberfläche). An der Schulter der Cu 111-Reflektion entwickelte sich bei niedrigerem Beugungswinkel mit zunehmender Auslagerungszeit eine neue Beugungslinie. Solche zusätzlichen Beugungslinien traten auch bei den Cu 200-, 311- und 222-Reflektionen auf. Sämtliche zusätzlich auftretenden Beugungslinien konnten auf die Bildung einer intermetallischen Phase  $\text{Cu}_3\text{Pd}$  ( $\alpha'$ ; Strukturberichtsbezeichnung  $L1_2$ ; Raumgruppe  $Pm\bar{3}m$ ) zurückgeführt werden (für Details, siehe Kapitel 4.3.3).

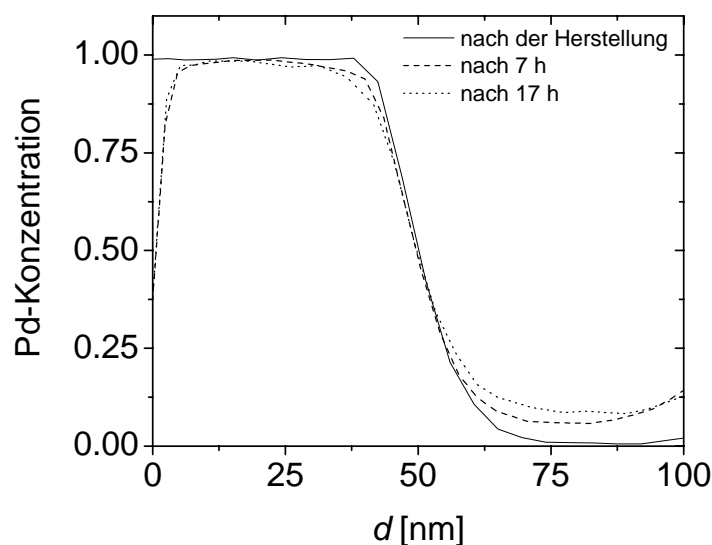


**Abb. 5.8:** AES-Tiefenprofile der Probe nach der Herstellung und nach 7 h und nach 17 h Auslagerungszeit bei 185 °C.

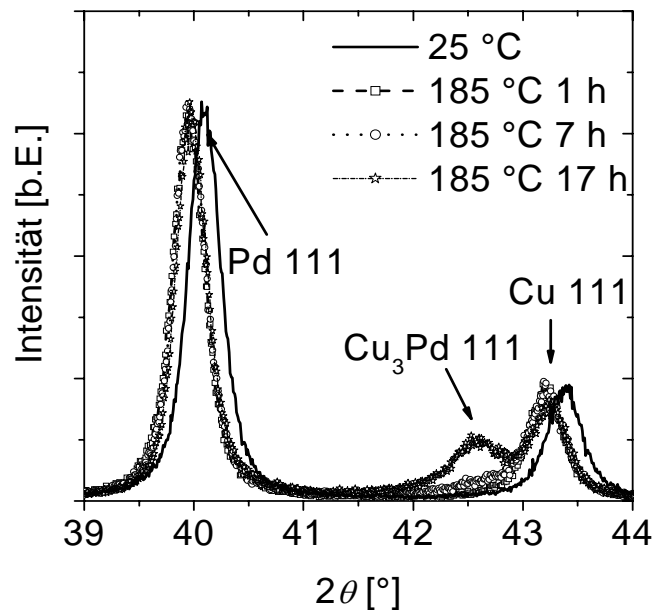


**Abb. 5.9:** Ausschnitt aus dem Diffraktogramm der Cu-Pd Doppelschicht bei 25°C und während des Auslagerns bei 185 °C.

### 5.4.3 Entwicklung der mechanischen Spannungen

#### 5.4.3.1 Diskussion möglicher Einflussfaktoren

Abgesehen von rein thermoelastischem Verhalten können weitere Mechanismen den Spannungszustand eines Schichtsystems auf einem Substrat während einer Wärmebehandlung verändern: (i) Kornwachstum, (ii) Defektannihilation und Verkleinerung von Hohlräumen an Korngrenzen, (iii) plastische Verformung, (iv) Phasenumwandlungen (hier: Bildung der geordneten Phase  $\text{Cu}_3\text{Pd}$ ) und (v) Interdiffusion [2,4].

Die Mechanismen (i) und (ii) (thermisch aktivierte Relaxationsprozesse) treten bei Schichten, die bei Temperaturen um Raumtemperatur mittels Sputtern hergestellt wurden, nach der Abscheidung im Allgemeinen auf, wenn die Temperatur erhöht wird (wenn nicht sogar schon bei Raumtemperatur). Diese Relaxationsprozesse bewirken eine Verdichtung der Schicht durch die Annihilation überschüssigen Volumens in Defekten und Korngrenzen und sorgen dadurch für den Aufbau von Zugeigenspannungen in der Struktur. Während Mechanismus (iii) immer zu einer Spannungsrelaxation (d.h. einer Abnahme des Spannungsbetrages) führt, kann das Auftreten der Mechanismen (iv) und (v) abhängig vom Vorzeichen der Nettovolumenänderung in einer Schicht einen Spannungsbeitrag sowohl in Richtung Druck als auch in Richtung Zug leisten.



Auf der Basis von Literaturdaten für die Gitterparameter von ungeordnetem und geordnetem  $\text{Cu}_3\text{Pd}$  (siehe [14] und [22]) sollten durch die Phasenumwandlung (iv) verursachte Eigenspannungen hier vernachlässigbar sein (siehe auch Kapitel 4.3.3).

Interdiffusion (v) kann zu mechanischen Spannungen führen wenn sich die Molvolumina der am Diffusionsprozess beteiligten Atomsorten unterscheiden und/oder sich die intrinsischen Diffusionskoeffizienten der am Diffusionsprozess beteiligten Atomsorten unterscheiden [23,24]. Unter der Annahme, dass die Anzahl der Gitterplätze konstant ist (also Leerstellenbildung und -vernichtung während der Wärmebehandlung vernachlässigt werden kann; Netzwerk-Festkörper Konzept, zu Details siehe [6]), kann für ein System von zwei dünnen Schichten auf einem dicken Substrat die mittlere Spannung der einzelnen Schichten berechnet werden. In Abb 5.10 ist das zur Spannung  $\sigma$ , welche sich aus Interdiffusion in den Cu- oder Pd-Subschichten ergibt, proportionale Verhältnis  $-\Delta v_i / N_{\text{Pd}}$  ( $i=\text{Cu},\text{Pd}$ ) gegen  $N_{\text{Cu}}/N_{\text{Pd}}$  aufgetragen, wobei  $\Delta v_i$  die Volumenänderung der Cu- oder Pd-Subschicht,  $N_{\text{Cu}}$  die Molzahl der Kupferatome, die während des Auslagerungsexperimentes durch die ursprüngliche Grenzfläche wandern und in das Pd-Gitter eindringen;  $N_{\text{Pd}}$  ist die analoge Größe für die Pd-Atome (zu den Details und einer vollständigen Herleitung siehe Kapitel 4.4.2). Es ist offensichtlich, dass sowohl Zug- als auch Druckeigenspannungen in den Cu- und Pd-Subschichten abhängig vom Verhältnis  $N_{\text{Cu}}/N_{\text{Pd}}$  beobachtet werden können (Für weiterführende Informationen über Spannungsbildende Mechanismen bei dünnen Schichten siehe Referenzen [4,17] und Kapitel 4 dieser Arbeit.).

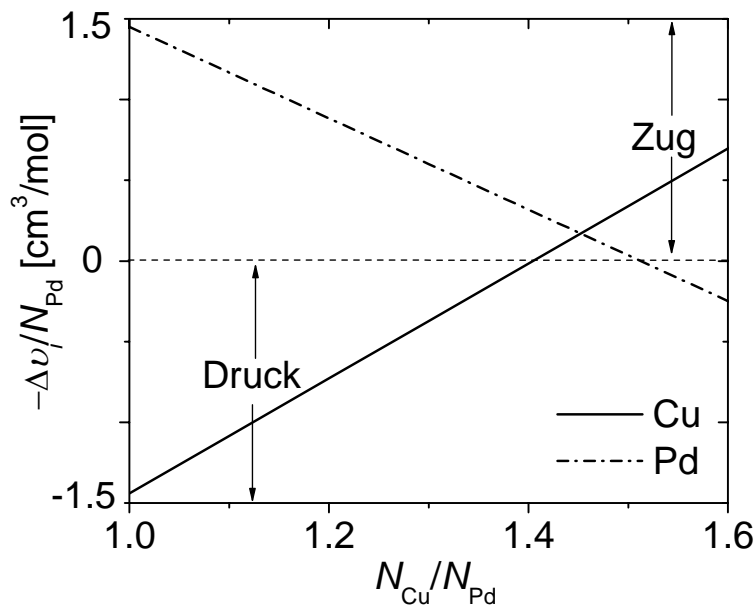


**Abb. 5.10:** Auftragung von  $-\frac{\Delta v_i}{N_{Pd}}$ , proportional zur Spannung  $\sigma_i$ , gegen  $N_{Cu}/N_{Pd}$  für die Cu- und Pd-Schichten.

#### 5.4.3.2 Experimentelle Ergebnisse und Diskussion

Die Extrapolationen der im Experiment beobachteten Spannungsverläufe der Schichten zwischen  $-100\text{ °C}$  und  $25\text{ °C}$  zu Temperaturen oberhalb von Raumtemperatur (zwischen  $25\text{ °C}$  und  $185\text{ °C}$ ) spiegeln thermoelastisches Verhalten in Abwesenheit thermisch aktivierter Prozesse wider (siehe auch Kapitel 2). Für die Cu- und Pd-Einzelschichten können Zugspannungsbeiträge, die durch Stabilisierungsprozesse (z.B. Kornwachstum und Defektannihilation) entstehen, aus den Unterschieden zwischen oberhalb von Raumtemperatur gemessenen und aus den durch die thermoelastischen Extrapolation bestimmten Spannungswerten berechnet werden. Für die Einzelschichten des Diffusionspaares jedoch stellt der Unterschied zwischen linearer Extrapolation und gemessener Spannung eine Summierung über durch thermisch aktivierter Prozesse und durch Interdiffusion hervorgerufene Spannungen dar (vgl. Abb. 5.11). Durch Vergleich der Ergebnisse aus den Messungen der Einzelschichten mit denen der Doppelschicht erhält man daher Informationen über diffusionsbedingte Spannungen.

**Aufheizen.** In Abb. 5.11 (a) wird deutlich, dass der Betrag der in der Cu-Schicht der Doppelschicht erzeugten Zugspannung geringfügig größer ist (der Unterschied beträgt bei  $185\text{ °C}$  etwa  $130\text{ MPa}$ ) als die Zugspannung, die in der Cu-Einzelschicht erzeugt wird. Abb. 5.11 zeigt, dass in der Pd-Einzelschicht eine Zugspannung von ungefähr  $220\text{ MPa}$  während

des Heizens auf 185 °C aufgebaut wird, während die Spannung in der Pd-Subschicht mehr oder weniger der Extrapolation des thermelastischen Verhaltens unterhalb von Raumtemperatur folgt. Die zusätzlich zu den für die Einzelschichten auftretenden Spannungsentwicklungen (zusätzliche Zugspannungen in der Cu-Schicht des Diffusionspaares, zusätzliche Druckspannungen in der Pd-Schicht des Diffusionspaares) können wie folgt verstanden werden: Wenn ein Fluss von Cu-Atomen in Richtung der Pd-reichen Regionen des Diffusionspaares den Gegenfluss von Pd-Atomen übertrifft, tritt ein Nettoleerstellenfluss von der Pd-reichen zur Cu-reichen Seite auf, welcher in Cu Zugspannungen (Leerstellensenke) und in Pd Druckspannungen (Leerstellenquelle) erzeugt. Diese Annahme wird durch die offensichtlich sehr schnell ablaufende Diffusion von Cu Atomen in den Korngrenzen von Pd unterstützt, da beim Aufheizen die Korngrenzendiffusion eine große Rolle spielen wird.

**Isotherme Wärmebehandlung bei 185 °C.** Während der isothermen Auslagerung bei 185 °C verändern sich die Spannungen in den Cu- und Pd-Einzelschichten nicht wesentlich – in den Subschichten der Doppelschicht jedoch entstehen Zugspannungen. Das Quadrat der Änderung der Eigenspannungen ( $(\Delta\sigma)^2$ ) während isothermer Auslagerung ist für beide Schichten des Diffusionspaares gegen die Zeit,  $t$ , in Abb. 5.12 aufgetragen. Die Spannungsdaten können gut durch Geraden beschrieben werden. Dies ist ein Hinweis auf den diffusionsbedingten Ursprung der Spannungsentwicklung.

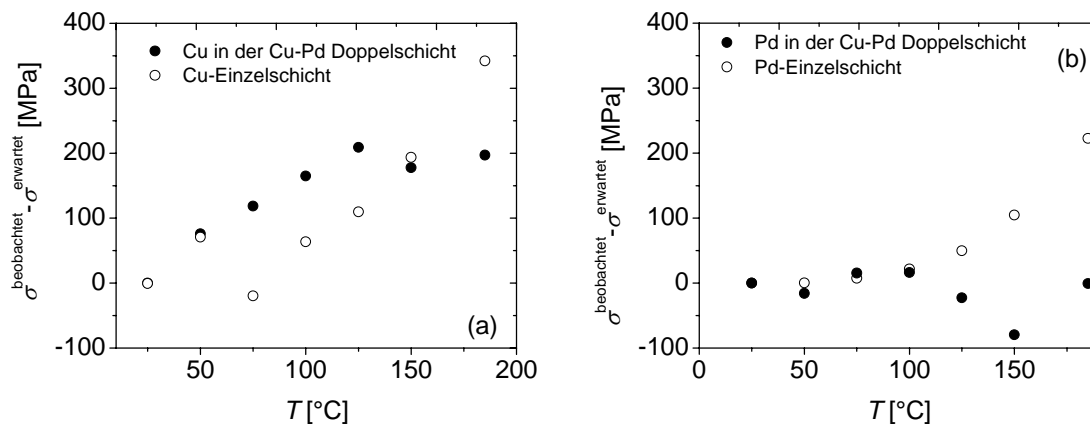


**Fig. 5.11:** Differenz zwischen der bei einer Temperatur  $T$  gemessenen Spannung  $\sigma^{\text{beobachtet}}$  und der Spannung  $\sigma^{\text{erwartet}}$ , die sich durch lineare Extrapolation des durch Messung im Temperaturbereich -100 °C bis 25 °C charakterisierten thermelastischen Verhaltens ergibt für (a) die Cu-Subschicht der Doppelschicht und die Cu-Einzelschicht und (b) Pd-Subschicht der Doppelschicht und die Pd-Einzelschicht.

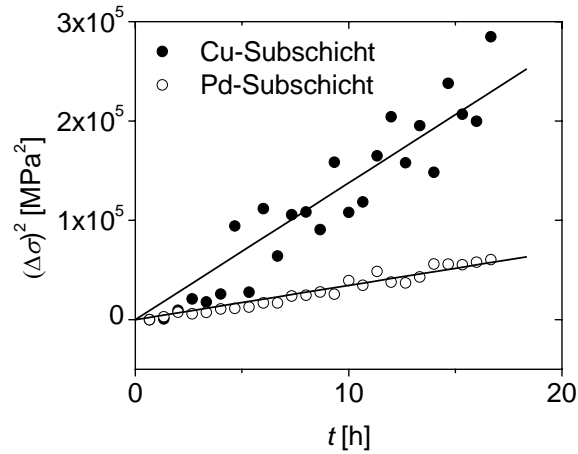


**Fig. 5.12:** Quadrat der Veränderung der Eigenspannung ( $(\Delta\sigma)^2$ ) der Subschichten des Diffusionspaares während isothermer Auslagerung bei 185 °C aufgetragen gegen die Zeit,  $t$ .

Es ist nahe liegend, dass während der isothermen Wärmebehandlung die Bedeutung der Volumendiffusion zunimmt. Die beobachteten Zugspannungen könnten durch eine Verkleinerung des Verhältnisses  $N_{\text{Cu}}/N_{\text{Pd}}$  entstehen, so dass während des Heizens von 25 °C auf 185 °C Zug- bzw. Druckspannungen in der Cu- bzw. der Pd-Subschicht beobachtet wurden (siehe oben), aber während des isothermen Auslagerns die Spannungen in beiden Subschichten in den Zugspannungsbereich gelangen (vgl. Abb. 5.10; zu Details siehe Kapitel 4.4.3):  $1,4 \leq N_{\text{Cu}}/N_{\text{Pd}} \leq 1,5$ .

## Referenzen

- [1] W. D. Nix, Metall. Trans. A **20A**, 2217 (1989).
- [2] M. F. Doerner, and W. D. Nix, Crit. Rev. Solid State **14**, 225 (1988).
- [3] G. C. A. M. Janssen, Thin Solid Films **515**, 6654 (2007).
- [4] L. B. Freund and S. Suresh, *Thin Film Materials Stress, Defect Formation and Surface Evolution*, (Cambridge Univ. Press, Cambridge, 2003).
- [5] F. C. Larche and J. W. Cahn, Acta Metall. **30**, 1835 (1982).
- [6] F. C. Larche and J. W. Cahn, Acta Metall. **33**, 331 (1985).
- [7] U. Welzel, J. Ligot, P. Lamparter, A. C. Vermeulen and E. J. Mittemeijer, J. Appl. Cryst. **38**, 1 (2005).
- [8] E. J. Mittemeijer and P. Scardi (Eds.), *Diffraction Analysis of the Microstructure of Materials*, (Springer, Berlin;Heidelberg, 2004).
- [9] I. C. Noyan and J. B. Cohen, *Residual Stress*, (Springer-Verlag, Berlin, 1987).
- [10] A. Kumar, U. Welzel and E. J. Mittemeijer, J. Appl. Cryst. **39**, 633 (2006).
- [11] M. Wohlschlägel, U. Welzel, G. Maier and E. J. Mittemeijer, J. Appl. Cryst. **39**, 194 (2006).
- [12] M. Wohlschlägel, T. U. Schüllli, G. Maier, U. Welzel and E. J. Mittemeijer, Z. Kristallogr. Suppl. **26**, 147 (2007).
- [13] M. Wohlschlägel, T. U. Schüllli, B. Lantz and U. Welzel, J. Appl. Cryst. **41**, 124 (2008).
- [14] Y. S. Touloukian, *Thermal Expansion: Metallic Elements and Alloys*, (IFI/Plenum, New York, 1975).
- [15] H. W. Altman, T. Rubin and H. L. Johnston, *Cryogenic Laboratory Rept. OSU-TR-264-27*, (Ohio State University, Columbus, 1954).
- [16] R. Delhez, Th. H. de Keijser, and E. J. Mittemeijer, Fresen. Z. Anal. Chem. **312**, 1 (1982).
- [17] Th. H. de Keijser, J. I. Langford, E. J. Mittemeijer, and A. B. P. Vogels, J. Appl. Cryst. **15**, 308 (1982).
- [18] J. Harada, and K. Ohshima, Surf. Sci. **106**, 51 (1981).
- [19] J. G. Lee, and H. Mori, Eur. Phys. J. D **34**, 227 (2005).
- [20] W. Fang, and C. Y. Lo, Sensor Actuat. A-Phys **84**, 310 (2000).

- [21] J. Chakraborty, *Diffusion in stressed thin films*, (Universität Stuttgart, Stuttgart, 2005).
- [22] P. R. Subramanian and D. E. Laughlin, *J. Phase Equilib.* **12**, 231 (1991).
- [23] J. Chakraborty, U. Welzel and E. J. Mittemeijer, eingereicht zur Veröffentlichung.
- [24] J. Philibert, *Atom movements*, (Les Editions de Physique, Les Ulis, 1991).

# Curriculum Vitae

## *Personal*

Name	Yener Kuru
Date and Place of Birth	29.02.1980, Samsun, Turkey
Marital Status	Married
Nationality	Turkish

## *Schooling*

1993 – 1996	Yuce Science High School, Ankara, Turkey.
-------------	--

## *Higher education*

1997 – 2002	B. Sc. (Metallurgical and Materials Engineering) Middle East Technical University, Ankara, Turkey.
2002 – 2004	M. Sc. (Materials Science and Engineering) Sabanci University, Istanbul, Turkey.

## *Dissertation*

2004 – 2008	Ph.D. at the Max-Planck-Institut für Metallforschung and Universität Stuttgart Title: “Interrelationships of microstructure, stress and diffusion”.
-------------	--





# Acknowledgements

The present work was performed at the Institut für Metallkunde at the Universität Stuttgart and at the Max-Planck-Institut für Metallforschung, Stuttgart.

First of all I would like to thank Prof. Dr. Ir. E.J. Mittemeijer for accepting me as a Ph.D. student in his department. Scientific discussions in monthly meetings and his continuous encouragement considerably contributed to the completion of this work. Finally, I would like to thank him for writing the main opinion ('Hauptbericht') for the thesis.

I would like to thank Prof. Dr. F. Aldinger for writing the second opinion ('Mitbericht') for the thesis.

I am grateful to my daily supervisor Dr. U. Welzel for his continuous co-operation. He could always tell me where I should look for the answers of my questions. He has considerably contributed to the successful completion of this work.

My special thanks to Mr. M. Wohlschlägel for assistance during preparing the German summary and collaboration throughout this work.

I would like to thank Dr. H.G. Libuda for his support from my interview to my graduation.

I would also like to thank all colleagues at the Max-Planck-Institut für Metallforschung for their assistance during my research and hearty thanks to my friends who made my stay at Stuttgart pleasant and enjoyable.

Finally, I am grateful to my wife, parents and sister who have always supported and encouraged me.